

ELECTRON PARAMAGNETIC RESONANCE STUDIES
OF ADSORBED SPECIES

by

ALAN IRWIN PELMAN
B.Sc., University of British Columbia, 1966

A THESIS SUBMITTED IN PARTIAL FULFILMENT OF
THE REQUIREMENTS FOR THE DEGREE OF

DOCTOR OF PHILOSOPHY

In the Department
of
Chemistry

We accept this thesis as conforming to the required standard

THE UNIVERSITY OF BRITISH COLUMBIA

April, 1971

In presenting this thesis in partial fulfilment of the requirements for an advanced degree at the University of British Columbia, I agree that the Library shall make it freely available for reference and study.

I further agree that permission for extensive copying of this thesis for scholarly purposes may be granted by the Head of my Department or by his representatives. It is understood that copying or publication of this thesis for financial gain shall not be allowed without my written permission.

Department of Chemistry

The University of British Columbia
Vancouver 8, Canada

Date April 8, 1971

ABSTRACT

Electron paramagnetic resonance techniques have been used to investigate the nature and possible effects of adsorption of gaseous species on several adsorbents, in particular several synthetic zeolites, at temperatures from 77°K upwards. Analysis of the spectra obtained has been aided through computer simulation of the various spectra and comparison of these to the actual observed spectra.

The molecule chlorine dioxide (ClO_2) has been studied in various low temperature matrices but little has been published for ClO_2 in the adsorbed state. An attempt was made to find an adsorbent such that an inert matrix might be approximated, to give a base from which to make comparisons. To this end, adsorbents including silica gel, synthetic zeolites 13X, 10X, 4A, 5A, Na-mordenite and H-mordenite were investigated. The results vary between those from silica gel, where spectra yielding EPR parameters similar to other matrices were obtained, to those from 13X where it was evident that two distinct adsorption sites of the ClO_2 were present. In the 13X as in the other synthetic zeolites, EPR parameters markedly different from other studies were found and were attributed to the intense electrostatic fields present in these zeolites. Results obtained at room temperature for these adsorbents ranged from ClO_2 molecules freely rotating in the cages of the zeolites to other molecules having hindered rotations.

Nitrogen dioxide (NO_2) was also investigated with a view to finding similar interactions. Although changes as marked as for ClO_2 compared to other studies were not observed, the synthetic zeolite H-mordenite yielded spectra closely approximating those obtained in solid N_2O_4 matrices. It is proposed the NO_2 molecules are caged in the numerous side pockets emanating from the main channels in this zeolite and are effectively isolated from other NO_2 molecules. The resulting spectra are strikingly more resolved than those obtained using other adsorbents and enabled accurate computer simulations to be made.

The adsorption of nitric oxide (NO) produced an effect not found with the other molecules. A new species was formed from a reaction of the NO with H-mordenite and could not be removed at room temperature, indicating a strong bond to the surface. The new species does not contain nitrogen as identical spectra were obtained from adsorption of ^{14}NO and ^{15}NO .

Attempts to observe spectra which could be assigned to the difluoroamino radical from adsorption of tetrafluorohydrazine were unsuccessful. The spectra observed were assigned to a species having no hyperfine structure and an anisotropic g tensor.

TABLE OF CONTENTS

	<u>Page</u>
Abstract	i
List of Tables	vi
List of Figures	vii
Acknowledgments	xi
CHAPTER ONE: INTRODUCTION	1
CHAPTER TWO: ADSORPTION	5
2.1 Surfaces	6
2.2 Classification of Isotherms	7
2.3 Volume Filling of Pores	11
2.4 Adsorption Forces	12
2.4.1 Polarization Energy	14
2.4.2 Field-dipole Energy	14
2.4.3 Field Gradient-quadrupole Energy	15
CHAPTER THREE: ZEOLITES	16
3.1 Adsorption in Zeolites	21
3.2 Structures of Zeolites	25
3.2.1 X,Y Type	25
3.2.1.1 Cation Positions	28
3.2.2 A Type	30
3.2.2.1 Cation Positions	32
3.2.3 Mordenite	34
3.2.3.1 Cation Positions	36
CHAPTER FOUR: ELECTRON PARAMAGNETIC RESONANCE	38
4.1 Theory	38
4.1.1 Electronic Zeeman Interaction	45
4.1.2 The Hyperfine Interaction	46
4.1.3 Other Interactions	48
4.1.4 EPR Spectra	49
CHAPTER FIVE: ADSORPTION STUDIES	52
5.1 EPR Studies of Radicals on Surfaces	54

<u>TABLE OF CONTENTS (cont.)</u>		<u>Page</u>
5.1.1	Non-Zeolitic Adsorbents	54
5.1.2	Zeolitic Adsorbents	57
5.2	Special Adsorption Effects	58
CHAPTER SIX:	EXPERIMENTAL	62
6.1	Vacuum System	62
6.2	Sample Tubes	63
6.3	Adsorbents	63
6.4	Sample Preparation	65
6.5	Gases	67
6.5.1	Chlorine Dioxide ClO_2	67
6.5.2	Nitrogen Dioxide NO_2	68
6.5.3	Nitric Oxide NO	68
6.5.4	Tetrafluorohydrazine N_2F_4	68
6.6	Spectrometers	69
CHAPTER SEVEN:	ANALYSIS OF ELECTRON PARAMAGNETIC RESONANCE SPECTRA	72
CHAPTER EIGHT:	CHLORINE DIOXIDE, ClO_2	81
8.1	Silica Gel	82
8.2	Na and H-mordenite	89
8.3	4A and 5A Synthetic Zeolites	92
8.4	13X Synthetic Zeolite	92
8.5	10X Synthetic Zeolite	98
8.6	Lithium Exchanged 13X Synthetic Zeolite	101
8.7	Discussion	101
CHAPTER NINE:	NITROGEN DIOXIDE, NO_2	111
9.1	Silica Gel	112
9.2	13X Synthetic Zeolite	116

TABLE OF CONTENTS (cont.)	<u>Page</u>
9.3 H-mordenite	116
9.4 Discussion	121
CHAPTER TEN: NITRIC OXIDE, NO	130
10.1 Silica Gel	131
10.2 13X Synthetic Zeolite	132
10.3 H-mordenite	132
10.4 Discussion	140
CHAPTER ELEVEN: DIFLUORAMINO RADICAL, NF ₂	144
11.1 H-mordenite	145
11.2 Discussion	147
CHAPTER TWELVE: SUMMARY	151
REFERENCES	156
APPENDIX	166

	<u>LIST OF TABLES</u>	<u>Page</u>
1.	The principal values of the hyperfine and g tensors for ClO_2 in various media.	85
2.	The principal values of the hyperfine and g tensors for NO_2 in various media.	113
3.	The principal values of the hyperfine and g tensors for NO in various media.	133
4.	g-values of the spectrum observed when N_2F_4 was adsorbed on H-mordenite at 77°K.	148

LIST OF FIGURES

	<u>Page</u>
1. Five different types of adsorption isotherms, as classified by Brunauer, Deming, Deming and Teller.	8
2. The fundamental building blocks of zeolites: (a) SiO_4 tetrahedron (b) AlO_4 tetrahedron.	18
3. The truncated octahedron, or sodalite cage.	20
4. Cation positions for zeolites of varying Si/Al ratios: (a) 1/2 (b) 1/1.	22
5. The structural framework of the X type synthetic zeolite.	26
6. The type II 26-hedron cage, or faujasite cage.	27
7. Cation sites in Na 13X synthetic zeolite.	29
8. The structural framework of the A type synthetic zeolite.	31
9. The type I 26-hedron cage.	33
10. The structural framework of synthetic mordenite: (a) characteristic chain structure (b) cross-sectional area of a chain.	35
11. Cation positions in synthetic mordenite. Aluminium and Silicon at the centers of each tetrahedron are not shown.	37
12. Lorentzian and Gaussian first derivative curves.	44
13. a) A schematic diagram of the vacuum system used in these experiments. b) The sample tubes used in these experiments.	64
14. a) Quartz dewar used for variable temperature EPR experiments. b) A Varian V-4546 liquid nitrogen dewar.	66
15. Block diagram of a Varian E-3 X-band Spectrometer system.	70
16. The molecular and magnetic field coordinate system.	75

LIST OF FIGURES (cont.)

	<u>Page</u>
17. Generalized lineshapes of powder EPR spectra for a species with no hyperfine structure: (a) axially symmetric g tensor (b) fully anisotropic g tensor.	79
18. The molecular axis system for chlorine dioxide.	83
19. EPR spectrum of chlorine dioxide adsorbed on silica gel, recorded at 77°K.	86
20. Computer simulated EPR spectrum of chlorine dioxide adsorbed on silica gel, recorded at 77°K.	87
21. EPR spectrum of chlorine dioxide adsorbed on silica gel, recorded at room temperature.	88
22. Computer simulated EPR spectrum of chlorine dioxide adsorbed on silica gel, recorded at room temperature.	90
23. EPR spectrum of chlorine dioxide adsorbed on Na-mordenite, recorded at 77°K.	91
24. Computer simulated EPR spectrum of chlorine dioxide adsorbed on Na-mordenite, recorded at 77°K.	93
25. EPR spectrum of chlorine dioxide adsorbed on Na-mordenite, recorded at room temperature.	94
26. Computer simulated EPR spectrum of chlorine dioxide adsorbed on Na-mordenite, recorded at room temperature.	95
27. EPR spectrum of chlorine dioxide adsorbed on 4A synthetic zeolite, recorded at 77°K.	96
28. Computer simulated EPR spectrum of chlorine dioxide adsorbed on 4A synthetic zeolite, recorded at 77°K.	97
29. EPR spectrum of chlorine dioxide adsorbed on 13X synthetic zeolite, recorded at 77°K.	98

LIST OF FIGURES (cont.)

	<u>Page</u>
30. Computer simulated EPR spectrum of chlorine dioxide adsorbed on 13X synthetic zeolite, recorded at 77°K.	100
31. EPR spectrum of nitrogen dioxide adsorbed on silica gel, recorded at 77°K.	114
32. Computer simulated EPR spectrum of nitrogen dioxide adsorbed on silica gel, recorded at 77°K.	115
33. EPR spectrum of nitrogen dioxide adsorbed on 13X synthetic zeolite, recorded at 77°K.	117
34. Computer simulated EPR spectrum of nitrogen dioxide adsorbed on 13X synthetic zeolite, recorded at 77°K.	118
35. Computer simulated EPR spectrum (assuming axially symmetric g and hyperfine tensors) of nitrogen dioxide adsorbed on 13X synthetic zeolite, recorded at 77°K.	119
36. EPR spectrum of nitrogen dioxide adsorbed on H-mordenite, recorded at 77°K.	120
37. Computer simulated EPR spectrum of nitrogen dioxide adsorbed on H-mordenite, recorded at 77°K.	122
38. EPR spectrum of ¹⁵ N nitrogen dioxide adsorbed on H-mordenite, recorded at 77°K.	123
39. Computer simulated EPR spectrum of ¹⁵ N nitrogen dioxide adsorbed on H-mordenite, recorded at 77°K.	124
40. EPR spectrum of nitric oxide adsorbed on 13X synthetic zeolite, recorded at 77°K.	134
41. Computer simulated EPR spectrum of nitric oxide adsorbed on 13X synthetic zeolite, recorded at 77°K.	135

LIST OF FIGURES (cont.)

	<u>Page</u>
42. EPR spectrum of ^{14}N nitric oxide adsorbed on H-mordenite, recorded at 77°K.	136
43. EPR spectrum of ^{15}N nitric oxide adsorbed on H-mordenite, recorded at 77°K.	137
44. Computer simulated EPR spectrum of ^{14}N nitric oxide adsorbed on H-mordenite, recorded at 77°K.	138
45. Computer simulated EPR spectrum of ^{15}N nitric oxide adsorbed on H-mordenite, recorded at 77°K.	139
46. EPR spectrum observed after adsorption of nitric oxide on H-mordenite, followed by evacuation, recorded at 77°K.	141
47. EPR spectrum observed after adsorption of N_2F_4 on H-mordenite, recorded at 77°K.	146
48. Computer simulated EPR spectra of species formed on adsorption of N_2F_4 on H-mordenite, recorded at 77°K: (a) isotropic g and hyperfine tensor (b) anisotropic g tensor, no hyperfine splitting.	149

ACKNOWLEDGEMENT

I am grateful to Dr. C.A. McDowell for his interest and support throughout the course of my graduate studies.

I would also like to express my appreciation to Drs. P. Raghunathan, C.L. Gardner and J.B. Farmer for their helpful comments on this thesis; to Mr. John Tait for his invaluable assistance during the preparation of the thesis, to the other members of this laboratory for their helpful discussions; to Mr. Tom Markus for the care of the EPR spectrometers; and last, but certainly not least, to my wife Sylvia for her patience and help during the final stages of preparation of the manuscript.

The awards from the National Research Council of Canada received during my graduate studies are also gratefully acknowledged.

CHAPTER ONE

INTRODUCTION

Surface studies have grown in interest over recent years due in part to both increased knowledge of the structure of surfaces and also to the application of different techniques to the study of this area. Adsorption studies, surface structure studies and studies of reactions on surfaces all have contributed greatly to our knowledge of surface phenomena. A great deal of interest and activity in the application of spectroscopic techniques to problems in both catalysis and surface chemistry is evident. The fact that information can be obtained at the molecular level rather than the system level has been a driving force for continuing rapid growth in this area of interest.

No one spectroscopic technique can hope to provide

all the information available from studies of adsorbed species. Perhaps the most successful and widely used application has been that of infrared spectroscopy. Many reviews have been written on infrared spectroscopy as applied to the study of surfaces (for example [1-6]). Gamma-ray resonance spectroscopy, although relatively unexplored at present in this regard, has also been used to some extent [7].

Magnetic Resonance techniques, both electron paramagnetic resonance, hereinafter called EPR, and nuclear magnetic resonance, hereinafter called NMR, hold promise of providing answers to some of the complicated situations that arise on surfaces in systems involving the gas-solid interface. The application of these techniques is still at a relatively early stage. NMR studies have been varied. The detection of relaxation phenomena of molecules adsorbed on surfaces has been a prime area of interest (for example [8-11]). Other NMR studies have included such effects as the study of chemical shifts on various surfaces [12] and studies of adsorbed water [13-15].

The application of EPR to the study of adsorbed molecules has been very productive. The ability of this technique to detect small concentrations of paramagnetic species and to relate the unpaired electron charge distribution to the molecular structure has made this an extremely useful method of investigating systems involving surfaces.

Many reactions which occur at surfaces also involve paramagnetic species. It is possible to stabilize highly reactive

molecules either by adsorption into porous media such as zeolites or molecular sieves (for example [16-18]). Controlled reaction of these 'trapped' molecules would then be possible to produce specific products, whereas corresponding reactions in the gas phase may not be as selective. Under suitable conditions, information about the adsorbed species such as its identity, stability, motional state, chemical structure, and interaction with various surface fields can thus be obtained.

The interactions between paramagnetic molecules and its surroundings can greatly affect the EPR spectrum. When the molecules under study are adsorbed on a surface or in some way trapped, one would naturally expect some differences in the EPR parameters from those observed for 'free' molecules. These interactions will be referred to as matrix interactions. Matrix interactions determine the ability of a paramagnetic molecule to rotate or reorient about various molecular axes. These interactions can also perturb the wave functions of the molecule and thus produce changes in the components of both the g and hyperfine tensors of the molecules.

This study is concerned with the EPR spectra of paramagnetic molecules adsorbed on synthetic zeolites and on silica gel, and the effects of such adsorption on the EPR parameters. Brief introductions on adsorption and the structure of zeolites are given for completeness. In fact, a knowledge of the surface structure of the adsorbents is extremely beneficial to the interpretation of the observed phenomena.

A chapter on EPR is included but the reader is referred to other sources for a more detailed coverage of the theory. Chapter Five gives some insight into the application of various spectroscopic techniques to this research area and presents background on the application of the EPR technique to some surface phenomena.

The remainder of this thesis includes a discussion of the experimental techniques and the results obtained from the various systems investigated.

CHAPTER TWO

ADSORPTION

The components of a solid (ions, atoms, or molecules) are subject to forces which are in equilibrium deep within the lattice but are unbalanced near the surface. This results in an attractive force field only extending a few angstroms, but enough to attract molecules of a liquid or gas in the immediate proximity. These forces cause molecules to become attached to the surface, the phenomenon being known as adsorption. The term was introduced by Kayser [19] in 1881 to denote the condensation of gases on free surfaces. Desorption is the complementary process, the removal of gases from the surface, while the surface is termed the adsorbent. The physical adsorption bond derives from similar cohesive forces as those responsible for condensation whereas chemical adsorption or chemisorption alters the nature of the

adsorbed species. Adsorption is commonly measured in terms of the mass adsorbed as a function of pressure, the measurements undertaken at constant temperature. The resulting plots are termed adsorption isotherms.

2.1 Surfaces.

It is convenient to distinguish between external and internal surfaces when considering the large available surface areas of the adsorbents normally used. The external surface of a solid frequently represents no more than one percent of the total surface accessible to gas molecules, the additional internal surface arising from the walls of the pores, cracks or interstices within the solid. It is obvious also that the smaller the particles, the larger will be the external surface. The demarcation line between these two kinds of surfaces is arbitrary, but the term 'internal surface', then, would comprise the walls of all cracks, pores and cavities which are deeper than they are wide. This internal surface must of course be open to the exterior of the solid and in porous solids is generally several orders of magnitude greater than the external surface. The concern of this study is with porous systems having large internal surfaces.

A convenient classification of pores has been given by Dubinin [20]. Pores of width below $\sim 20\text{\AA}$ are termed micropores, those of width above 200\AA are termed macropores, while those in between are considered transitional or intermediate pores.

2.2 Classification of Isotherms.

Many adsorption isotherms have now been determined and have been found to be of five different types, each type characteristic of a different surface makeup. These have been classified by Brunauer, Deming, Deming and Teller [21] and are shown in figure 1.

Adsorption isotherms are generally analyzed by reference to an equation in which the capacity of a complete monolayer appears as a parameter. Knowing the cross-sectional area of the adsorbate molecules, the specific surface area of the adsorbent can be calculated from the monolayer capacity.

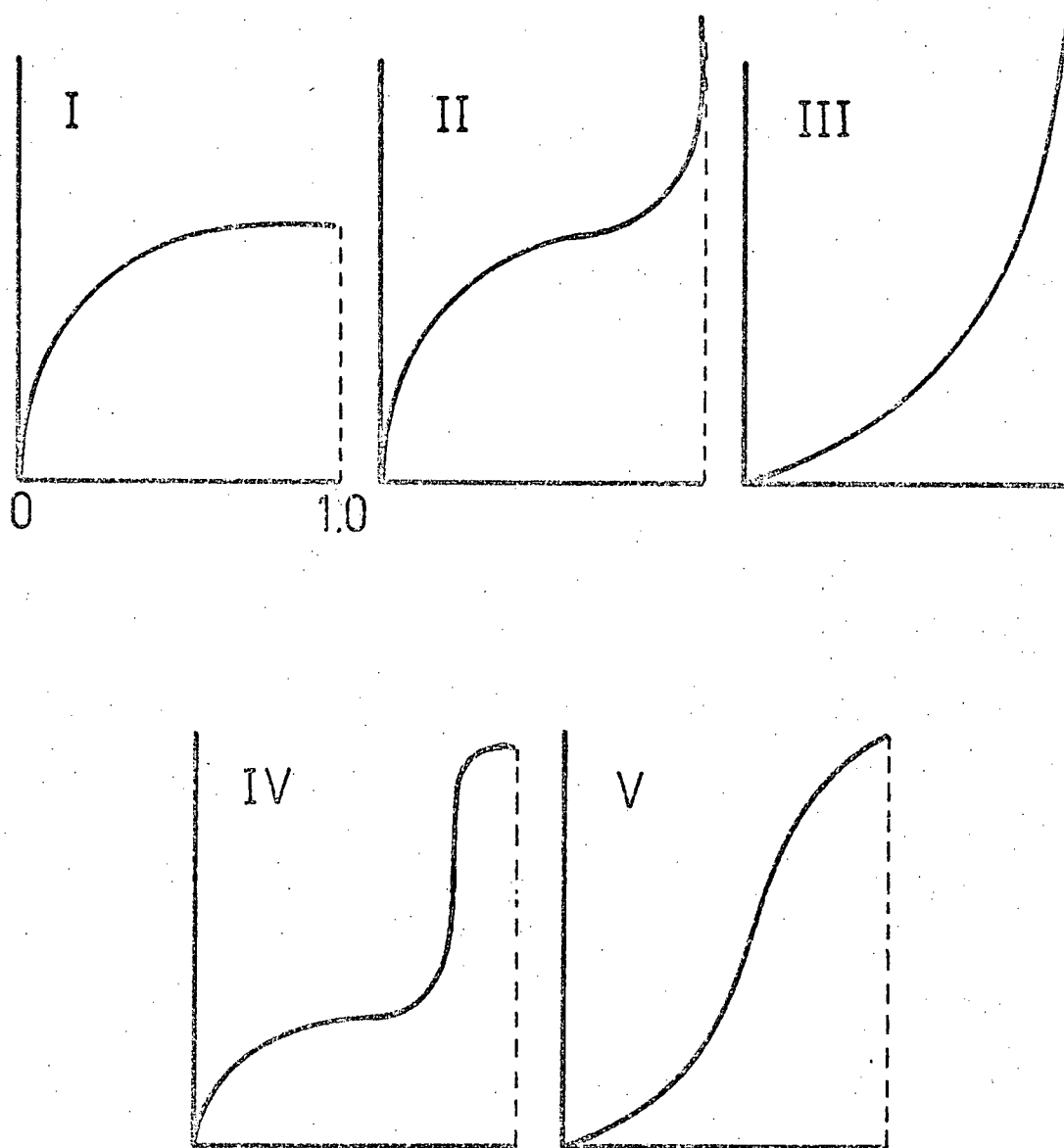
Type I is of main interest in this study and is outlined below. Langmuir [22] was the first to attempt an interpretation of adsorption phenomena and type I isotherms are commonly called Langmuir isotherms.

The isotherm is characterized by the equation

$$V = \frac{V_m \alpha P}{1 + \alpha P} \quad (2-1)$$

where V is the volume of vapour adsorbed at an equilibrium pressure P ; V_m , the volume of vapour adsorbed at full monolayer coverage; and α , a constant. It is obvious from observation of the isotherm that a saturation of the surface appears to occur at higher gas pressures, not always the case as seen for the other types.

Langmuir assumed that initially, all gas molecules striking a surface would condense on it. Once completely covered by adsorbate



ORDINATES: Adsorption, (mg / g)

ABSCISSAE: Relative vapour pressure P/P_0
(scaled 0 to 1.0)

FIGURE 1. Five different types of adsorption isotherms,
as classified by Brunauer, Deming, Deming and Teller.

molecules, further condensation would cease since the surface forces would be neutralized. Saturation in this instance is in the form of a single monolayer over the surface. Before this limit is reached, part of the surface must be vacant and Langmuir assumed a dynamic equilibrium between the condensation of gas molecules hitting the free surface and the evaporation of condensed molecules from the occupied surface. The rate of condensation should be proportional to the specific surface S ; the pressure of the adsorbate P ; and the fraction of the surface not yet covered, $(1 - \theta)$, so that:

$$\text{rate of condensation} = \mu SP(1 - \theta) \quad (2-2)$$

where μ is a constant. The rate of evaporation is also proportional to the specific surface S ; the fraction of surface already covered, θ ; and the rate evaporation would occur if the surface were completely covered, v , such that

$$\text{rate of evaporation} = Sv\theta. \quad (2-3)$$

At sorption equilibrium,

$$S\mu P(1-\theta) = Sv\theta \quad (2-4)$$

By definition, $\theta = V/V_m$ and replacing μ/v by the constant α , equation (2-4) becomes the Langmuir equation given by equation (2-1). The use of the Langmuir equation is limited at the present time almost entirely to chemisorption studies, assuming here that surface coverage does not exceed a monolayer.

Type I isotherms are frequently encountered in adsorption studies of microporous solids, the saturation in this case being a complete filling of the pores with adsorbate molecules. Any slight rise in the isotherm would then come from multilayer adsorption on the relatively small external surface of these microporous solids.

Extensions of the Langmuir theory of adsorption have been made, including the possibility of multilayer adsorption. In 1938, Brunauer, Emmett and Teller [23] proposed a theory which retained the Langmuir concept of dynamic equilibrium but extended the process to include multilayer adsorption. It was assumed that the condensation-evaporation characteristics of the second and subsequent layers are the same as those of the surface of the bulk adsorbate. The assumptions for the initial monolayer are the same as for Langmuir. The equation is characterized by

$$\frac{P}{V(P_o - P)} = \frac{1}{V_m c} + \frac{P}{P_o} \cdot \frac{c-1}{V_m c} \quad (2-5)$$

P_o is the saturated vapour pressure of the adsorbate and c is a constant related to the differential heat of adsorption by the equation

$$c \approx \exp((H_1 - H_L)/RT) \quad (2-6)$$

where H_1 and H_L are the heats of adsorption in the first layer and the heat of liquification, respectively. Equation (2-5) reduces to the Langmuir equation when P/P_0 is very low and c is very large.

The BET theory, as it is called, is still the best known and most widely used today for both porous and non-porous adsorbents. Whichever theory is used, however, to represent a physical adsorption isotherm, agreement is rarely complete between the formula and experimental results. This is due to the the assumptions of energetic homogeneity of the adsorption sites and also of a gradual formation of a polymolecular adsorption layer. These assumptions are not valid for the porous adsorbents in use today.

2.3 Volume Filling of Pores.

Numerous experimental and theoretical studies in recent years (for example [24]) lead to the conclusion that adsorption in micropores differs qualitatively from adsorption on wide pore and non-porous adsorbents. Microporous adsorbents only have been used in this study. The concepts 'surface' and 'adsorption in layers' lose their physical meaning in these systems and it is natural to expect that adsorption in micropores leads to a filling of a limited micropore adsorption space, W_0 . When working with microporous adsorbents, the value of V_m of the BET and Langmuir equations may not be considered as equal to the volume of the monomolecular layer covering the surface of the adsorbent. Its value is near to that of the volume of the micropores, and therefore also to W_0 , the

constant of the Dubinin - Radushkevich equation. This equation is characteristic of adsorption isotherms obtained from experiments on microporous adsorbents, and is given by [25]

$$a = \frac{W_0}{V} \left[-\exp\left(\frac{BT^2}{\beta^2} \left(\log \frac{P_s}{P}\right)^2\right) \right] \quad (2-7)$$

V is the volume of the amount adsorbed, a ; T , the temperature; B , a constant independent of temperature and representing the basic characteristic of the porous structure of the adsorbent; β , the affinity coefficient given by the ratio of the differential molar work of adsorption of a given vapour to that of a vapour chosen as a standard; P_s , the saturated vapour pressure of the sorbate; and P , the pressure of the adsorbate. The constants W_0 and B then characterize the adsorptive properties of the given adsorbent whereas P_s , β , and V describe the adsorptive properties of the adsorbate.

At the present state of the theory of adsorption interactions, sufficiently complete information on the adsorption field in micropores can be obtained only from adsorption experiments. The theory therefore, has a somewhat phenomenological character and is being constantly re-investigated.

2.4 Adsorption Forces.

London [26] in 1930, showed that there was a very general force between atoms such that

$$\phi_D \approx -\frac{A}{x^n} \quad (2-8)$$

where ϕ_D is the potential

energy of the two isolated atoms separated by a distance X ; A , a constant related to the polarizabilities of the atoms and n an integer, usually given as 6. The negative sign denotes attraction. This force is termed a dispersion force and arises as a small perturbation of the motions of orbital electrons on each other leading to attraction of the atoms. Dispersion forces are additive such that an adsorbate molecule near the surface of an adsorbent experiences a total attraction which is the sum of all pairs of interactions.

In addition, short range repulsive forces are also universally associated with physical adsorption, given by

$$\phi_R = \frac{B}{X^m} \quad (2-9)$$

where B is a constant and m an integer, generally much larger than n . Consequently, the repulsion is important only at very short distances of separation.

It is assumed then, that both repulsion and attraction energies of this type have the same form and the total potential is generally given by

$$\phi = \phi_D + \phi_R = -\frac{A}{X^n} + \frac{B}{X^m} \quad (2-10)$$

where $m > n$. This equation has been applied to a variety of physiochemical systems. A relation of this form was first introduced into the theory of gases by Lennard-Jones [27] where $n = 6$ and $m = 12$ and equation (2-10) is generally referred to as the Lennard-Jones (6-12) potential.

Other attraction forces are also present if the adsorbent is ionic in nature and the adsorbate polar. Strong electrostatic fields F are known to be present on ionic surfaces. Barrer [28] has defined various energy terms that contribute to the physical bond in these systems. These are: Polarization energy ϕ_p , Field-dipole energy $\phi_{F\mu}$, Field gradient-quadrupole energy ϕ_{FQ} , Dipole-dipole energy $\phi_{\mu\mu}$, Dipole-quadrupole energy $\phi_{\mu Q}$, and Quadrupole-quadrupole energy ϕ_{QQ} .

2.4.1 Polarization Energy.

Polarization arises when the adsorbent is heteropolar, creating local electrostatic fields which may polarize adsorbate molecules having some polarizability. Then,

$$\phi_p = -\frac{\alpha}{2} F^2 \quad (2-11)$$

The strength of this interaction is obviously directly dependent on both α and F .

2.4.2 Field-dipole Energy.

Molecules possessing permanent dipole moments also interact with F , the energy of interaction given by

$$\phi_{F\mu} = -F\mu \cos\theta \quad (2-12)$$

where μ is the dipole moment of the adsorbed molecule and θ the angle the axis of the dipole makes with the field. It is expected $\phi_{F\mu}$ will assume an appreciable value only if the adsorbate molecule can approach within a short distance of the surface [29].

2.4.3 Field Gradient - quadrupole Energy.

Recently, the importance of the presence of a permanent quadrupole in certain adsorbate molecules has been recognized [30]. A quadrupole is pictured as arising from separation of equal and opposite dipoles, the magnitude of the moment being proportionate to the product of the dipole moment and the separation of the dipoles. The local fields F will normally have associated with them a field gradient \dot{F} which can interact powerfully with molecules possessing permanent quadrupole moments.

The interactions of the poles also contribute to the bond energy though their contributions are normally much smaller than those previously mentioned.

Dispersion forces, then, are always present when considering physical adsorption and, unless the adsorbate molecule has a permanent dipole moment, will represent the major contribution to the total adsorption energy. Electostatic forces are present if the solid is ionic and become significant and perhaps predominant if the adsorbed molecule has a large dipole moment.

It is evident that the exact forces involved depend upon the physical and chemical properties of both the adsorbate and adsorbent. The favoured adsorption sites are also determined by these properties.

CHAPTER THREE

ZEOLITES

Over 200 years ago, a Swedish mineralogist and chemist, Baron Cronstedt, observed that certain minerals appeared to melt and boil at the same time when heated. He named these minerals zeolites from the Greek words "zeo" meaning to boil and "lithos" meaning stone. Little attention was given these zeolites until the 1920's when their selective adsorption property was noticed. McBain [31], in discussing the significance of these results, coined the term "molecular sieves" for these zeolites. In the late 1930's, Barrer [32] began a thorough investigation of the adsorptive properties of these materials which led to considerable interest among the scientific community.

About 40 zeolites occur in nature but much interest has

also been given to synthetic varieties. Barrer synthesized the zeolite mordenite and several other synthetic varieties [33-35]. By the early 1950's many different synthetic zeolites had been prepared in the Linde research laboratory [36, 37]. Some are analogs of zeolite materials; others, new varieties not found in nature. Many present-day commercial operations simply were not possible or practical prior to the advent of these materials. They have permitted the development of selective adsorption as a practical alternative to the long established separation methods of distillation, absorption, extraction and fractional crystallization.

Molecular sieves (zeolites) are crystalline metal aluminosilicates with a three-dimensional interconnecting network structure of SiO_4 and AlO_4 tetrahedra. The fundamental building block of any zeolite crystal is a tetrahedron of four oxygen ions surrounding a silicon or aluminium ion (figure 2). The trivalency of aluminium causes the AlO_4 tetrahedron to be negatively charged requiring an additional cation to electrically neutralize the system. The oxygens are shared between neighbouring tetrahedra and balance the charge of the silicon ion. The charge balancing cations are the exchangeable ions of the zeolite structure.

The remainder of the building blocks of the zeolites, in order of increasing complexity are: (a) rings; (b) primary cages; and (c) secondary cages and channels.

Rings are formed of the silicon and aluminium tetrahedra by oxygen bridges. The cages are composed of various sized rings

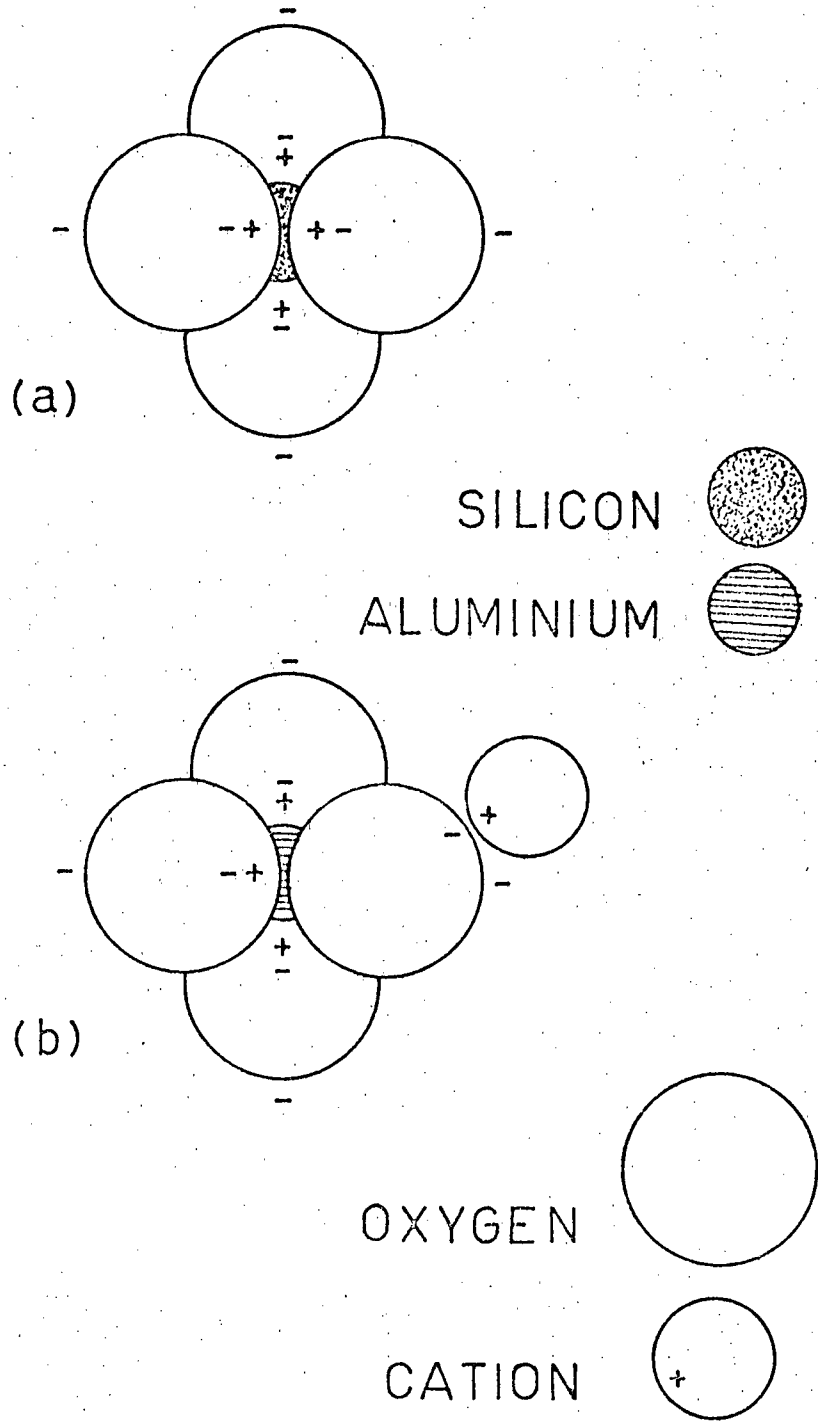


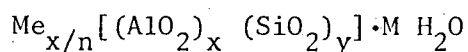
FIGURE 2. The fundamental building blocks of zeolites
a) SiO_4 tetrahedron b) AlO_4 tetrahedron.

so that access to them is governed by the ring dimensions. The pore opening of the 4-membered rings (tetrahedra) is negligible. The 6-membered rings have an opening of 2.2 Å diameter. 8-membered rings have a pore diameter of 4.3 Å while 12-membered rings have a pore diameter of 8.9 Å.

The structures of many zeolites consist of simple arrangements of polyhedra formed from the rings. The truncated octahedron, also known as the sodalite cage, is a well known example of such a primary cage (figure 3). This cage contains 24 silicon (aluminium) tetrahedra and is composed of six 4-membered rings and eight 6-membered rings. The free diameter of the internal cavity is 6.6 Å, and access is through the 6-membered rings.

Secondary cages appear on the packing of the simpler primary cages to form the total zeolite structure. Cages of interest are discussed when the structures of specific zeolites are reviewed.

A structural formula of the type



is often used to illustrate the relation between chemical composition and structure of zeolites. Me stands for the metal ions; x, y and n are integers; and M is the number of H₂O molecules in this unit cell formula. The portion in brackets represents the framework structure.

The ratio y/x varies between 1 and 5. According to an empirical rule of Loewenstein [38], AlO₄ tetrahedra can be joined only to

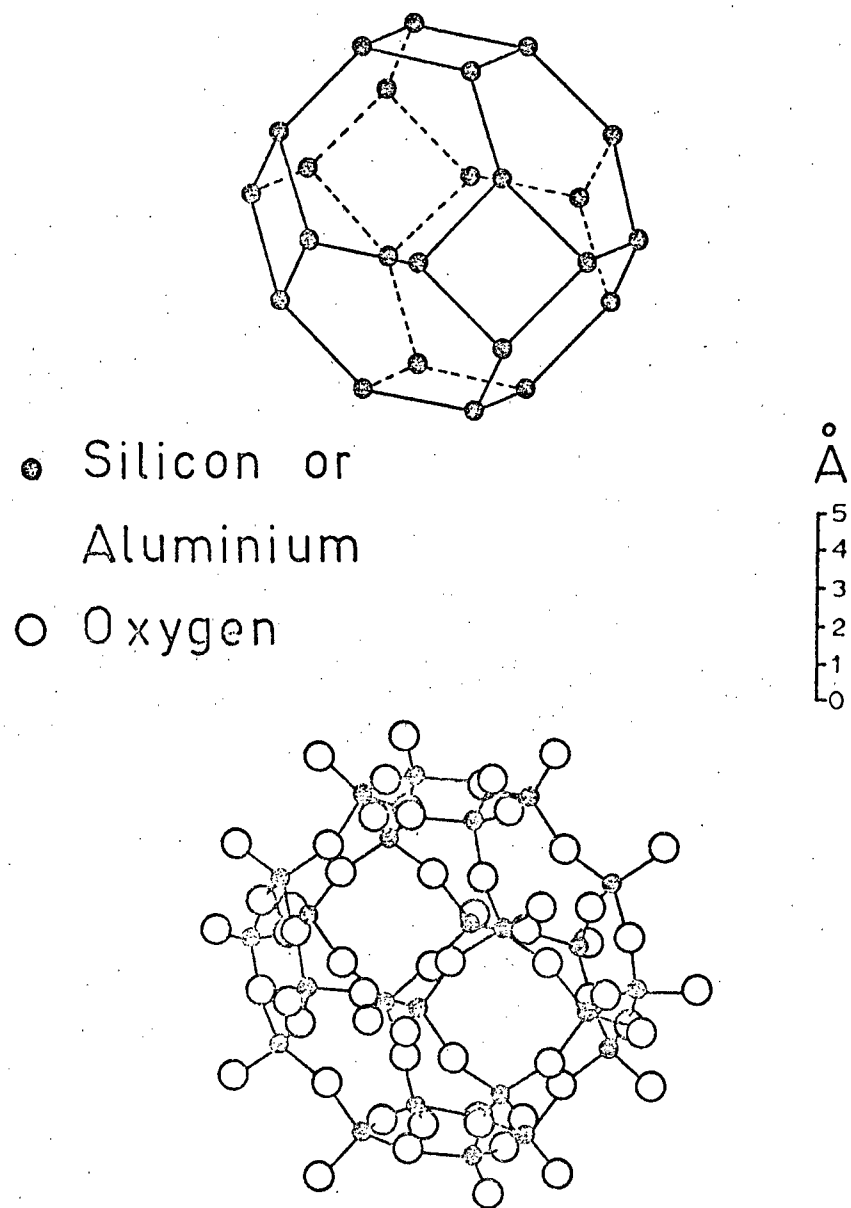


FIGURE 3. The truncated octahedron, or sodalite cage.

SiO_4 tetrahedra and never to another AlO_4 tetrahedron, thus giving the limit to the ratio of 1:1. The fact that only a limited number of silicon/aluminium ratios are observed would indeed indicate that there is an ordering in the rings of the Al and Si. The metal ions needed for charge compensation occupy sites adjacent to the cavities in the zeolites and are generally available for exchange with other ions. Although mono- and di-valent ions are the most common, tri-, tetra- and even penta-valent ions have been found. Synthetic varieties containing Ge^{4+} and Ga^{3+} substituted for Si^{4+} and Al^{3+} have also been prepared [39, 40].

3.1 Adsorption in Zeolites.

As a consequence of their porous structure, zeolites are in many cases able to contain adsorbate molecules in great variety and yet in a highly selective manner. Since their structure is composed of continuous, often interpenetrating channel systems, entry is governed by rings of various dimensions located periodically throughout the structure.

The variety and dimensions of the various adsorbates capable of entering the zeolites is therefore controlled not by the dimensions of the cavities, but by the dimensions of the rings or "windows" permitting access to them. Owing to ring puckering, not all rings containing the same number of tetrahedra are equivalent in size [41]. Structures with, for example, 8-membered rings can therefore exert a wide range of molecular sieving behaviour based on ring distortion alone.

The number, size, valency and location in the lattice of zeolitic cations have important effects on the size and shape of the entry pores to the larger cavities. They also have a profound effect on adsorption energies. The cations are present in the same channels as the adsorbate molecules. They are often recessed into 6-ring windows which do not normally function as the main access to the channel system. Sometimes the cations are also located in polyhedra which are not themselves able to hold adsorbate molecules. These cations, of course, would not hinder the migration of adsorbate molecules. Other cations, however, may remain near windows controlling access to the pore system of the zeolite. This influence may be moderated in three ways [42,43]:

1. Changing the size of the cations through exchange
($K^+ \rightleftharpoons Na^+$, for example)
2. Changing the number of cations through exchange
($2Na^+ \rightleftharpoons Ca^{++}$, for example)
3. Changing the number of cations through synthesis
($NaAl \rightleftharpoons Si$, for example)

The effect of the third consideration using synthesis is two-fold. Besides removing the influencing cation, a given ring size may decrease slightly with higher silicon content [44] since Si-O bonds are slightly shorter than Al-O bonds. The Si/Al ratio may also affect the positions of the cations (figure 4). Anything other than a 1:1 ratio of Si/Al will greatly affect the arrangement of the cation with respect to the tetrahedra charge it is balancing.

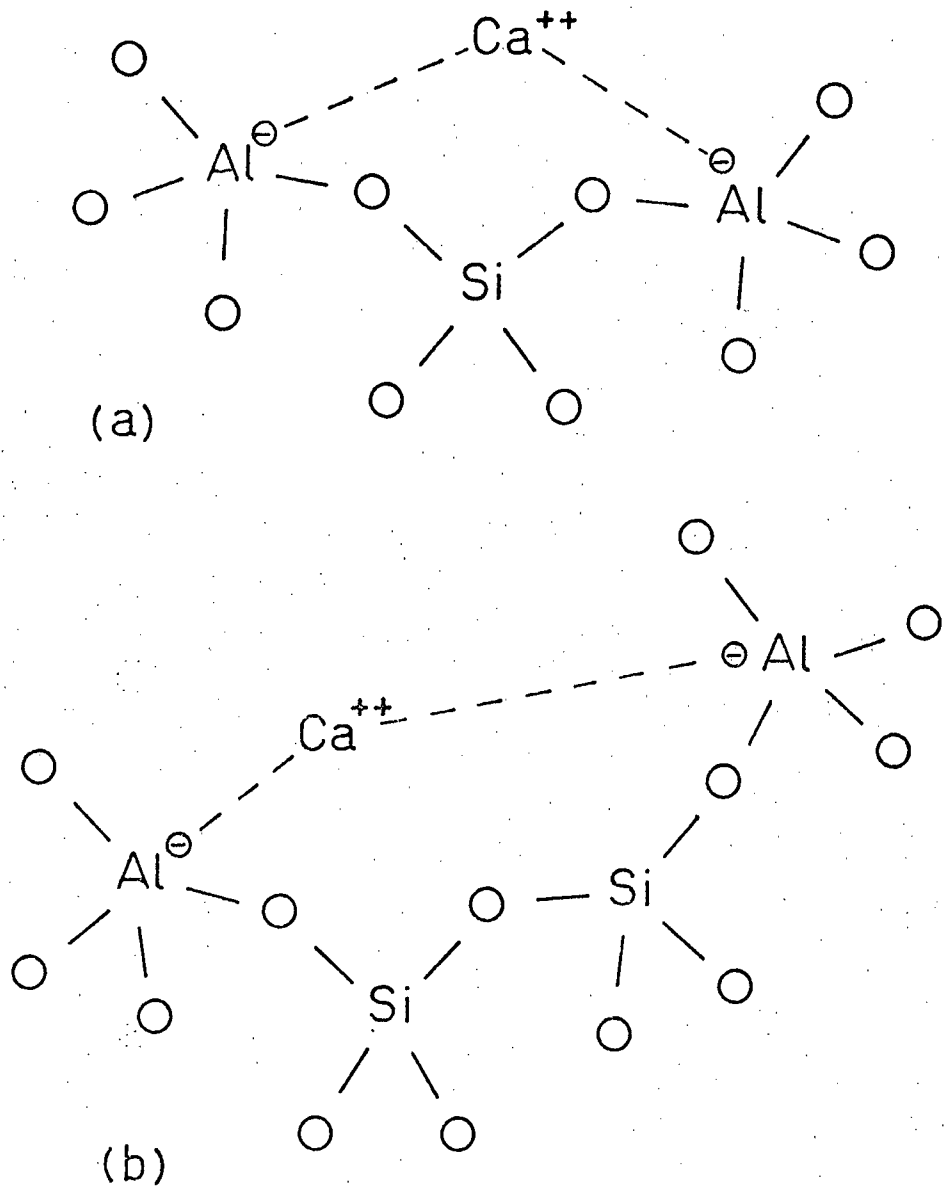


FIGURE 4. Cation position for zeolites of varying Si/Al ratios. (a) 1/2 (b) 1/1

This is especially true when mono-valent cations are replaced by di- or tri-valent ones.

In addition to the pore geometry of the zeolites, the various adsorption forces discussed previously also determine selectivity in adsorption. The polarity of the adsorbate molecules becomes very important since strong interactions may occur between the zeolite and polar adsorbate molecules.

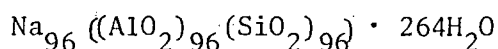
Clusters of molecules are present in the cavities when they are saturated. These clusters may be joined by contact with other clusters through the windows. The number of molecules in any cluster is not necessarily an integer since a molecule may be shared between two cavities or cages if it happens to be located in the window between the two. When the cavities are not saturated and the number of adsorbate molecules is small, they are distributed, not necessarily uniformly, throughout the entire accessible pore volume.

Although the entire pore volume is available for adsorption, certain adsorption sites are more favoured than others and will necessarily be filled first. These are due primarily to the cations which are exposed in the crystal lattice. These cations act as sites of strong positive charge which electrostatically attract the negative ends of polar molecules. Molecules can also have dipoles induced in them under the influence of these localized charges. These induced dipoles are, however, far weaker and less strongly attracted.

3.2 Structures of Zeolites.

3.2.1 X,Y Type.

The crystal structure of the synthetic zeolites types X and Y is similar to that of the naturally occurring faujasite [45]. The framework consists of a tetrahedral arrangement of sodalite cages, in a diamond type lattice, linked by hexagonal faces with six bridge oxygen ions [46,47] (figure 5). The unit cell formula for the type 13X synthetic zeolite is



This is a sodium X sieve and has the same characteristic structure as the sodium Y sieve except for a lower Si/Al ratio and consequently more sodium ions per unit cell. The ratio is usually 1:1 for the X structure and 17:7 for the Y.

The volume enclosed by this array of cages is the supercage, in this case termed a type II 26-hedron cage, or faujasite cage (figure 6). It is composed of 48 atoms of silicon (aluminium) and 96 oxygen atoms. The cage has 18 square faces, four 6-membered rings, and four 12-membered rings. The latter are the most important ports of entry into the supercage. The openings of these rings is approximately 8-9 Å and the internal diameter of the cage is 12.5 Å. The volume of the supercage is about 850 Å³ whereas the volume of the sodalite cages is about 160 Å³.

Thus there are three cage types present in type X zeolites: the faujasite cages, the sodalite cages and the hexagonal prisms

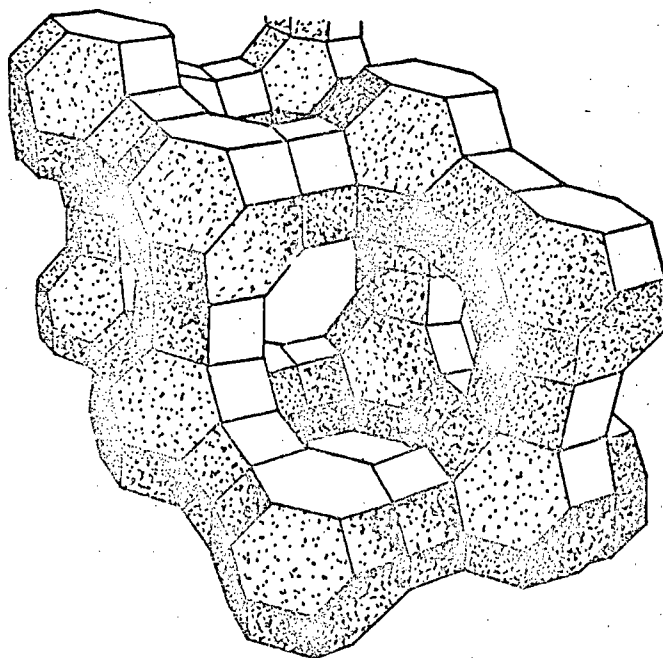


FIGURE 5. The structural framework of the X type synthetic zeolite.

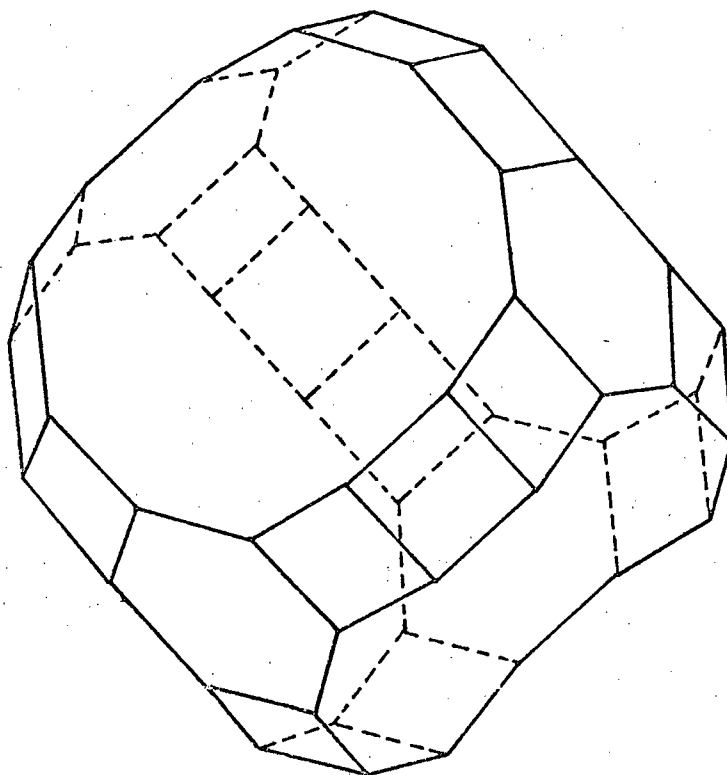


FIGURE 6. The type II 26-hedron cage, or faujasite cage.

formed by the bridging oxygens joining the sodalite cages. The hexagonal prism cavities can usually only be entered from the sodalite cages through the hexagonal faces where the opening is about 2 \AA in diameter. The type X structure therefore contains two independent, three dimensional networks of cavities - one of sodalite cages linked through hexagonal prisms and one of the supercages linked by sharing rings of 12 tetrahedra - the two systems interconnected by rings of 6 tetrahedra.

3.2.1.1 Cation Positions.

From a crystallographic study of synthetic Na 13X, Broussard and Shoemaker [46] were able to locate precisely only 48 out of the 80 Na^+ cations required per unit cell of their sample. X-ray studies of a calcium-exchanged natural faujasite by Pickert, Rabo and associates [48,49] yielded a more explicit picture of the cation distribution. Three cation sites were described (figure 7). S_I sites (16 per unit cell) are located in the interior of the hexagonal prisms, positioned between two puckered 6-membered rings in six-fold coordination to oxygen. S_I is effectively hidden from the zeolite surface as a consequence of its intimate coordination to the framework ions. The S_{II} sites (32 per unit cell) are found in the hexagonal faces (6-membered rings) at the mouths of the sodalite cages. The cations here have three-fold oxygen ion coordination. S_{III} sites are located next to the 4-membered rings on the surface of the supercage. The order of preference of cations seems to be S_I over S_{II} over S_{III} .

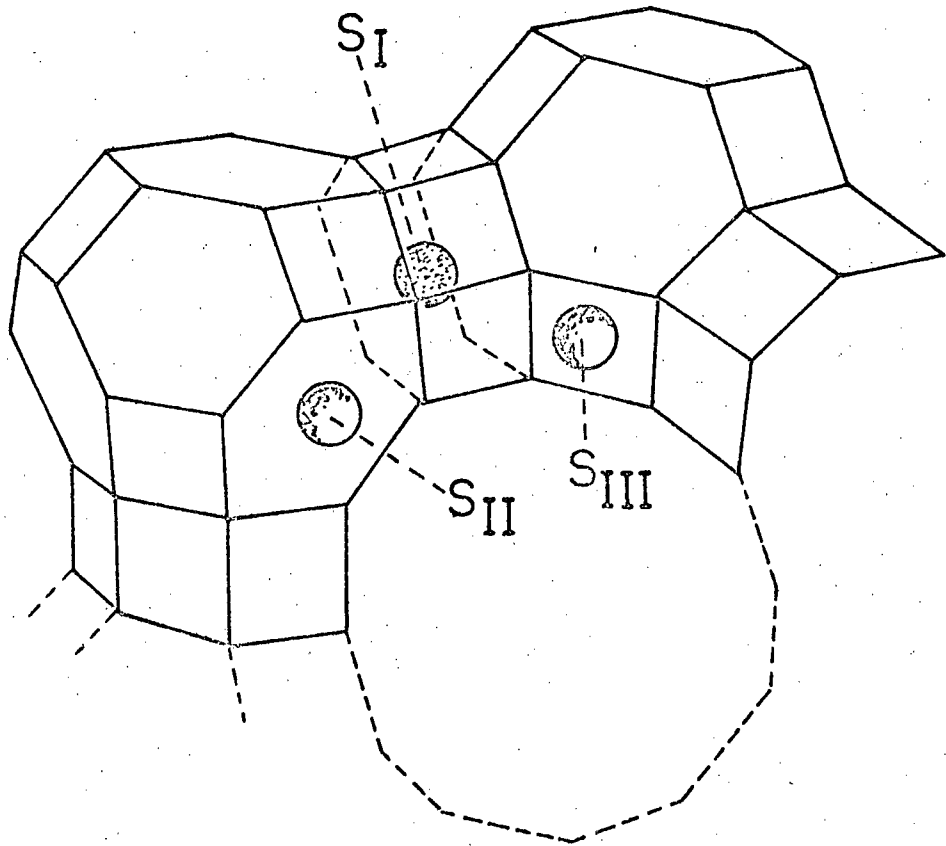


FIGURE 7. Cation sites in Na 13X synthetic zeolite.

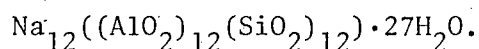
Since S_I and S_{II} sites are more than sufficient to accommodate the bivalent cations, the S_{III} sites are probably only populated in the univalent forms of the zeolites.

The sodium ion can be replaced by a multitude of others, depending on ion size and charge. Among those more commonly exchanged are Li^+ , K^+ , Rb^+ , Cs^+ , Ca^{++} , Sr^{++} , Ba^{++} , and Cu^{++} . The sodium can also be replaced by ammonium ions and these in turn decomposed to yield a decationated zeolite.

Replacement of sodium ions for calcium ions decreases the permeability of the zeolite from approximately 13 Å in 13X to 10 Å in 10X, a calcium exchanged form of the sodium zeolite. Thus, decreasing the number of cations ($2Na^+ \rightleftharpoons Ca^{++}$) actually decreases the adsorptive ability of the X zeolite. This is due to the fact that the cations initially replaced are those in the hexagonal prisms, which have no effect on the pore openings in the zeolite. Replacement of the cations at the open rings of the supercage actually increases the retarding effect of the cationic potential due to the increased size and charge of the cations.

3.2.2 A Type.

In the A type structure, the primary cage also consists of sodalite cages. In this instance they are joined through the square faces (4-membered rings) by four bridging oxygen ions in a cubic array [50] (see figure 8). In the sodium form, commonly called 4A, the structure is represented by the formula



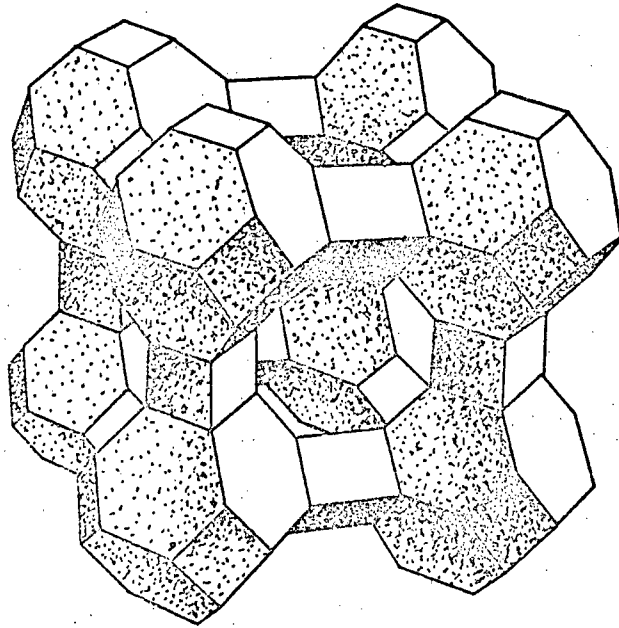


FIGURE 8. The structural framework of the A type synthetic zeolite.

As seen from the formula, the Si/Al ratio in this case should be 1:1. This type of stacking of the sodalite cages gives a roughly spherical supercage, termed a type I 26-hedron cage (figure 9). It consists of the same number of silicon (aluminium) atoms, 48, and oxygen atoms, 96, as the supercage of the X type structure. In terms of ring sizes composing the cage, it has eighteen 4-membered rings (square faces), eight 6-membered rings (hexagons), and six 8-membered rings (octagons). The diameter of this 26-hedron cage is 11.4 \AA and the volume is 775 \AA^3 .

As in the X type structure, there are three cage types: the supercage, the sodalite cage and the square prisms, formed by the oxygen atoms linking the sodalite cages. The supercages, sometimes called truncated cubooctahedra, are found in a cubic arrangement with respect to each other. Access is through the 8-membered rings with a pore diameter of 4.2 \AA , and are the largest 8-membered rings to be found in zeolites since the ring is planar [51]. The A type structure therefore consists of one three-dimensional network of cavities having a maximum diameter of 11.4 \AA and a minimum of 4.2 \AA . Access to the sodalite cages is through the distorted 6-membered rings of diameter 2.2 \AA but access is only through the central cavity system.

3.2.2.1 Cation Positions.

The available positions for cations in the A type structure are at the center of the eight 6-membered rings of the sodalite cages at the corners of the supercage, site A, and in 12 available positions

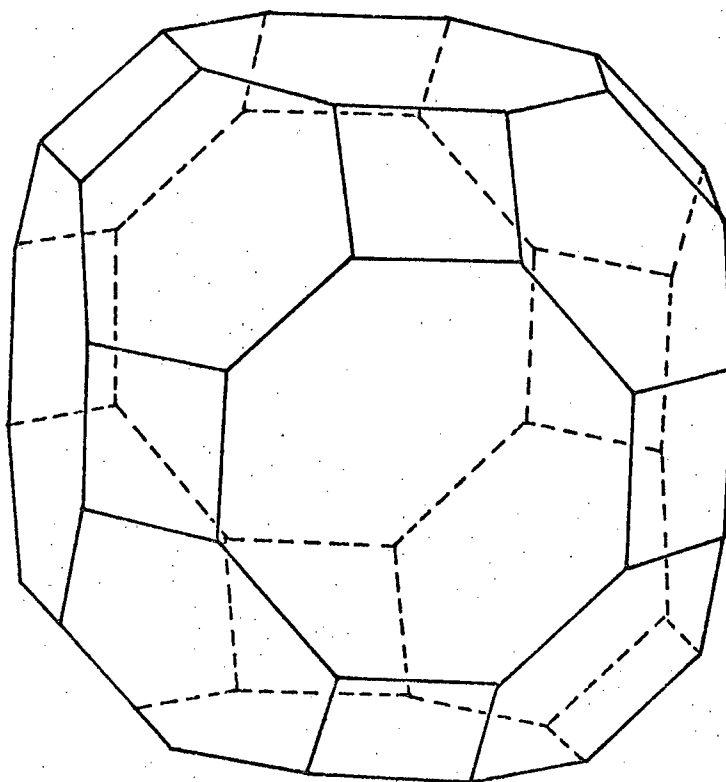
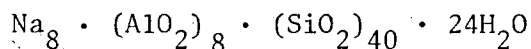


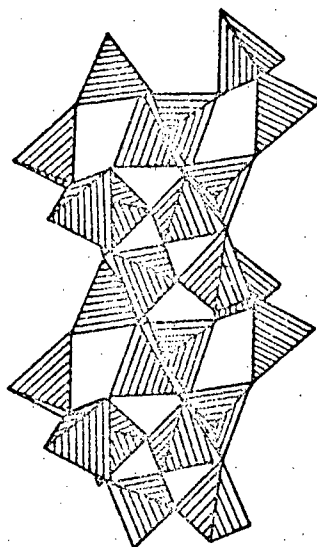
FIGURE 9. The type I 26-hedron cage.

adjacent to the 8-membered rings defining the supercage, site B. For 4A, the sodium form, eight of the twelve cations of a unit cell are found in site A, while the other four are statistically distributed into the twelve site B locations [50,52]. Site A is therefore filled preferentially to site B. Replacement of the sodium ions by calcium ions to form the 5A synthetic zeolite, actually increases the effective opening to the central pore system to approximately 5 Å in diameter. Since the twelve sodium ions are replaced by six calcium ions, these will be located in site A, leaving the 8-membered rings clearer and yielding a larger access to the supercage. The sodium ions may also be replaced by ions such as Li^+ , K^+ , Rb^+ , Cs^+ , Tl^+ , Ag^+ , NH_4^+ , Mg^{2+} , Sr^{2+} , Ba^{2+} , Hg^{2+} , Cd^{2+} , Zn^{2+} , Co^{2+} , and Ni^{2+} .

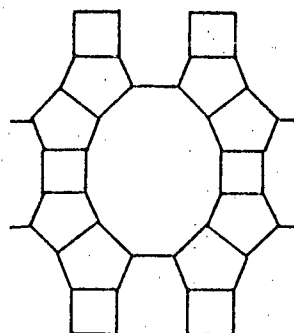
3.2.3 Mordenite.

The zeolite mordenite belongs to that classification characterized by the predominance of 5-membered rings of tetrahedra. The geometrical pattern of the aluminosilicate framework is different from the A and X type structures in that the buildup is of chains rather than of polyhedra (figure 10a). There are six possible simple structures formed by different lateral bondings of the chains to one another and a cross-section of that found in mordenite is shown in figure 10b. The result is a two-dimensional, tubular pore system, unlike the three-dimensional pore systems of A and X structures [53]. The unit cell of an ideal sodium mordenite is given by the formula





(a)



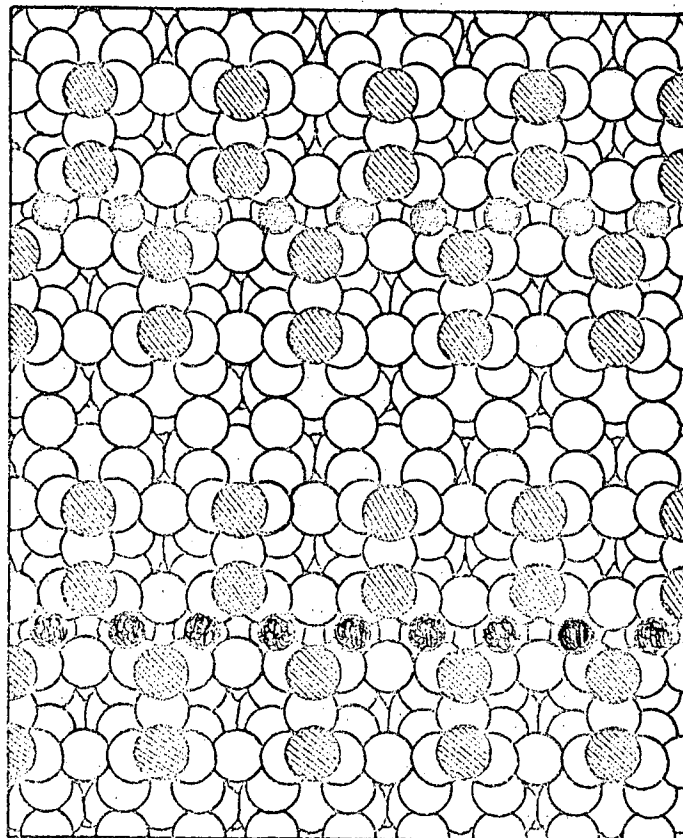
(b)

FIGURE 10. The structural framework of synthetic mordenite
(a) characteristic chain structure
(b) cross-sectional area of a chain

Thus, mordenite contains a higher Si/Al ratio, 5:1. As shown in figure 10b, the channels are circumscribed by 12-membered rings of tetrahedra; large deviations from planarity, however make a planar projection much smaller than a 12-membered ring of the X type structure. The major and minor diameters are thus 7.0 Å and 5.8 Å, respectively. These large channels are intersected perpendicularly by smaller channels circumscribed by 8-membered rings having a minimum free diameter of 3.9 Å and leading to the next main channel. However, halfway to the neighbouring main channel, the side channels branch through two distorted 8-membered rings of 2.8 Å free diameter which open into the main channel.

3.2.3.1 Cation Positions.

In Na-mordenite, a sodium ion rests at the center of each distorted 8-membered ring, effectively isolating the main channels from one another and leaving each main channel lined with two rows of side pockets [54]. These pockets have a low ratio of volume to cross-sectional area of their entrances (figure 11). The other cations are located in the main channels and occupy at random some of the 8- and 12-fold positions available [53].



○ Oxygen

● Oxygen in plane of paper

● Cations

FIGURE 11. Cation positions in synthetic mordenite.
Aluminium and Silicon at the centers of each tetra-
hedron are not shown.

CHAPTER FOUR

ELECTRON PARAMAGNETIC RESONANCE

4.1 Theory.

The basis of electron paramagnetic resonance (EPR)^{*} is concerned with the intrinsic spin of an electron and its associated magnetic moment. An applied magnetic field H allows only certain discrete orientations of the precessing dipoles with respect to the magnetic field, the orientations corresponding to different energy levels. Irradiation of the system with electromagnetic energy of the appropriate frequency induces transitions between these magnetic energy levels.

* The term electron spin resonance, ESR, is less general than EPR, since the former does not take into account orbital magnetism.

The energy for these transitions is given by the equation

$$h\nu = g\beta H \quad (4-1)$$

where h is Planck's constant; ν the frequency of the radiation; g , a numerical factor often close to 2; β , the Bohr magneton; and H , the magnetic field. A magnetic field of 3000 gauss requires a frequency of about 9 Gigahertz to induce the transitions. This corresponds to a wavelength of approximately 3 centimeters, which is in the microwave region of the electromagnetic spectrum.

Relaxation processes must necessarily be present such that the energy absorbed by spins in the higher energy level can be dissipated in such a manner as to permit their return to the ground energy level. Otherwise population between the energy levels would equalize and absorption would cease. This essentially is achieved through the phenomenon of 'spin-lattice relaxation', where the 'spin system' interacts with its surroundings in such a way as to provide paths for this process, and also through spin-spin relaxation. The population of these two levels, when in thermal equilibrium at a given field and temperature, may be represented by the Boltzmann equation. Thus, if the populations of the upper and lower levels are N_2 and N_1 respectively,

$$\frac{N_2}{N_1} = \exp\left(-\frac{g\beta H}{kT_s}\right) \approx 1 - \frac{g\beta H}{kT_s} \quad (4-2)$$

where β , g , and H are defined in equation (4-1); k , Boltzmann's constant; and T_s , the spin temperature defined by equation (4-2) in terms of the instantaneous relative populations of the two spin levels. If the population difference at a given time t is ΔN , equilibrium will be reached at a rate given by

$$d\Delta N/dt = dN_1/dt - dN_2/dt \quad (4-3)$$

Given that W_2 and W_1 are the probabilities of transitions from the upper and lower levels respectively, we can write

$$d\Delta N/dt = 2W_2 \left[N_2 - N_1 \left(1 - \frac{g\beta H}{kT} \right) \right] \quad (4-4)$$

where T now is the lattice temperature. From equation (4-4) it is easily shown that

$$\frac{d\Delta N}{dt} = 2W_2 (\Delta N_0 - \Delta N) \quad (4-5)$$

which has the solution

$$\Delta N = \Delta N_0 [1 - \exp(-t/T_1)] \quad (4-6)$$

where $T_1 = 1/2W$. T_1 , the spin-lattice relaxation time is seen as the inverse of a lattice-induced transition probability. The spin-lattice relaxation is thus characterized by a relaxation time T_1 and the spin system transfers energy to the lattice at the rate $1/T_1$. Similarly, the relaxation time T_2 characterizes a spin-spin relaxation process, a process which depends on the effect of local magnetic fields generated by neighboring spins.

A consequence of the existence of these relaxation processes is that the spectral lines observed for the transitions between the spin levels have a finite width and are often discussed in terms of a 'lineshape'.

Various mechanisms may be responsible for broadening of these spectral lines. Portis [55] has clarified the distinction between the two main classes of broadening, homogeneous broadening and inhomogeneous broadening. Homogeneous broadening is that associated with transitions between spin levels which are not themselves sharply defined but are somewhat broadened. Thermal equilibrium of the spin system is maintained throughout resonance as the energy absorbed from the microwave field is distributed to all the spins. Sources of homogeneous broadening include [55]: (a) spin-lattice relaxation; (b) dipolar interaction between like spins; (c) interaction with the radiation field; and (d) diffusion of excitation through the sample. An inhomogeneously broadened line consists of a spectral distribution of individual resonant lines merged to form an overall lineshape. The distinction between homogeneous and inhomogeneous broadening is that the inhomogeneous broadening comes from interactions external to the spin system and must be slowly varying over the time required for a spin transition. Inhomogeneities in the magnetic field cause energy to be transferred only to those spins whose local fields satisfy the resonance condition. The resonance is thus artificially broadened in an inhomogeneous manner. Other sources of inhomogeneous

broadening are [55]: (a) hyperfine interaction; and (b) anisotropy broadening.

The shape of the absorption spectrum is thus determined by the types of interactions between the environment and the spin system. The widths of these lines, however, depends on the strength of the interactions and the relaxation time. A system where relaxation is controlled by spin-lattice interactions and thermal equilibrium of the spin system is maintained throughout resonance has a lineshape approximated by a Lorentzian function [56], characterized by the equation

$$f(H-H_0) = \frac{2\Delta H_{1/2}}{\pi[(H-H_0)^2 + \Delta H_{1/2}^2]} \quad (4-7)$$

$\Delta H_{1/2}$ here represents the width of the absorption line at half the maximum intensity, and H_0 , the resonance field. It is customary however, in EPR, to display the first derivative of the spectrum.

Although many interactions influence the linewidth, the Heisenberg uncertainty principle sets the ultimate minimum width which may be stated as

$$\Delta H_{1/2} = \frac{\hbar}{g\beta T} \quad (4-8)$$

where T now corresponds to the relaxation time. Either T_1 or T_2 can be the controlling relaxation time, or both may be influential. It is thus possible, in certain cases, to determine relaxation times from the observed spectra.

Another commonly encountered lineshape is a Gaussian function

[56], characterized by

$$f(H-H_0) = \frac{2}{\pi \Delta H_{1/2}} \exp \left[-\frac{(H-H_0)^2}{\pi \Delta H_{1/2}^2} \right] \quad (4-9)$$

This generally occurs in an inhomogeneous spin system described above. Gaussian and Lorentzian lineshapes are compared in figure 12. Although these two lineshape functions are the most common, combinations and variations of these have also been observed and are described in reference [57].

When the nucleus also possesses a magnetic moment, it can interact with the magnetic field and the electronic magnetic moment. This may result, not in line broadening, but in the appearance of resolved hyperfine structure. This hyperfine mechanism accounts for the multiplet character of the spectrum. The theory of EPR is well covered in many articles and reviews (for example [58-61]) and only pertinent theory will be further discussed.

The problem of expressing interactions affecting electronic energy levels is usually approached through the application of the Hamiltonian operator. When applied to the time-dependent Schrödinger equation, this approach yields the eigenvalues and eigenfunctions of the permitted energy levels. Abragam and Pryce [62] have shown that the behaviour of a spin system can be described by a 'spin-Hamiltonian', a particular part of the overall Hamiltonian. Perturbation theory is generally used in the solution of the energy levels. This representation has the same effect as replacing the interaction of the field with the orbital angular momentum by an anisotropic coupling between the electron spin and the external

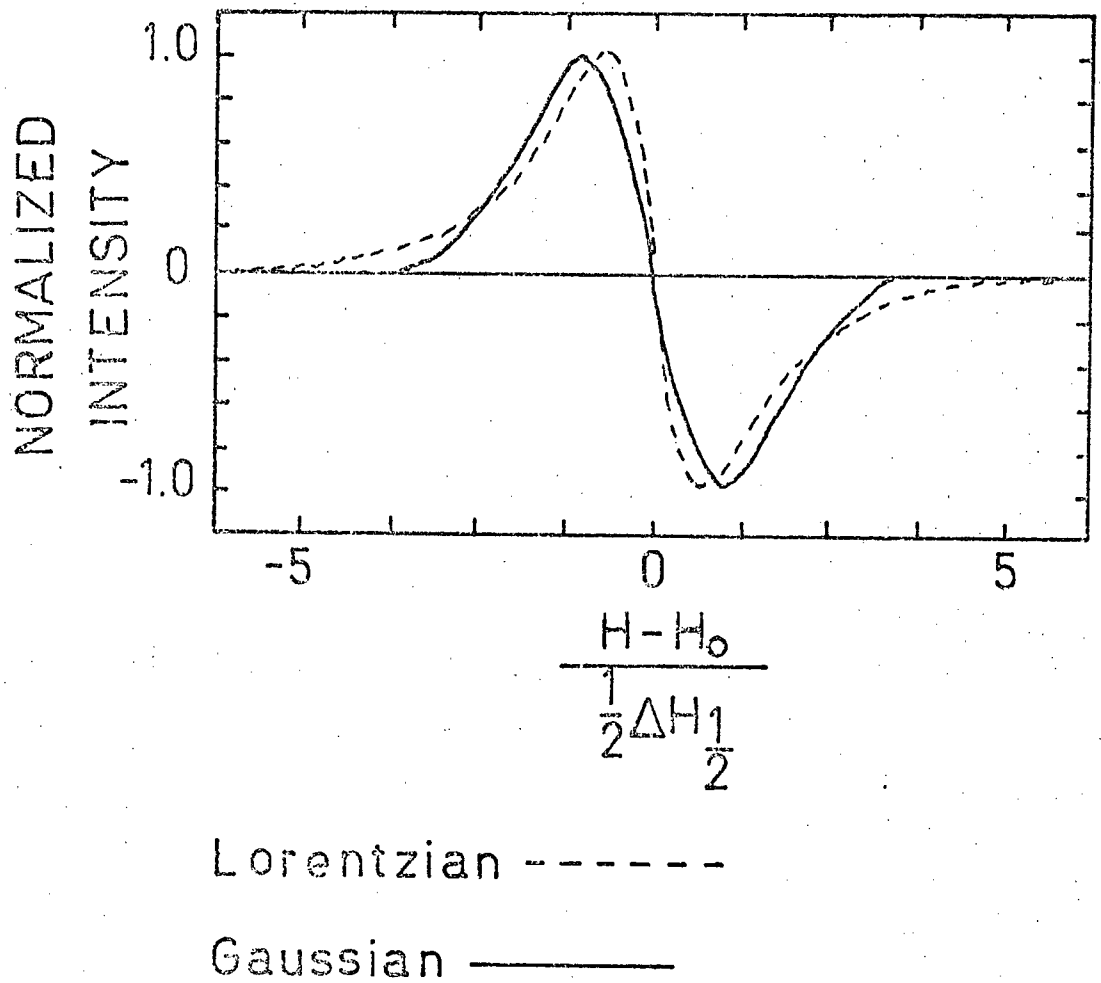


FIGURE 12. Lorentzian and Gaussian first derivative curves.

magnetic field, the spin here now being termed the fictitious spin. Applications of this spin-Hamiltonian approach to EPR are considered in reviews by Bleaney and Stevens [63], Bowers and Owens [64] and Carrington and Longuet-Higgins [65].

The spin-Hamiltonian for a system consisting of one electron with spin $S=\frac{1}{2}$ and a nucleus of spin I may be written as

$$\mathcal{H} = -\beta \underline{H} \cdot \underline{g} \cdot \underline{S} + \hbar \underline{S} \cdot \underline{T} \cdot \underline{I} - \hbar \gamma \underline{I} \cdot \underline{H} + \underline{I} \cdot \underline{Q} \cdot \underline{I} \quad (4-10)$$

where the terms represent electronic Zeeman, hyperfine, nuclear Zeeman and nuclear quadrupole interaction, respectively.

4.1.1 Electronic Zeeman Interaction.

The most general expression representing the Zeeman interaction between a magnetic field \underline{H} and the electron spin \underline{S} is given by

$$\mathcal{H}_z = \beta \underline{H} \cdot \underline{g} \cdot \underline{S} \quad (4-11)$$

\underline{H} and \underline{S} are expressed as vectors, and \underline{g} , the spectroscopic splitting factor, or g value, is usually expressed as a tensor rather than the free electron value $g_e = 2.0023$. The g factor equals the constant g_e when (a) the electron possesses spin angular momentum only, and (b) the g tensor is isotropic. Deviations from g_e are due to orbital magnetic moment contributions, due to spin orbit coupling, which alter the effective magnetic moment and \underline{g} is often found to be anisotropic. The anisotropy may be described by the tensor \underline{g} , which

has the form

$$\underline{\underline{g}} = \begin{pmatrix} g_{xx} & g_{xy} & g_{xz} \\ g_{yx} & g_{yy} & g_{yz} \\ g_{zx} & g_{zy} & g_{zz} \end{pmatrix} \quad (4-12)$$

The \underline{S} , then, does not generally represent the pure spin, and is often termed the effective or fictitious spin.

EPR may be described as the measurement of the Zeeman energy \mathcal{H}_z which is generally of the order of 0 - 1 cm^{-1} . In essence, EPR is concerned with the manner in which the other Hamiltonian terms perturb or are perturbed by this Zeeman energy.

4.1.2 The Hyperfine Interaction.

The hyperfine, or electron spin-nuclear spin interaction results from the interaction of the magnetic moment of the unpaired electron and the magnetic moment of any nuclei within its orbital. This interaction arises in two quite different ways. The first is essentially the classical interaction of the two dipoles separated by a distance r . It would then be expected that this interaction should depend upon their mutual orientation. Consequently, we refer to it as the anisotropic or dipolar hyperfine interaction.

The second form of interaction is non-classical and is known as the Fermi or contact interaction. It is determined by the unpaired electron density at the nucleus, and is isotropic. The overall hyperfine splitting observed, then, would consist of an anisotropic component superimposed upon an isotropic term.

Rapid reorientation of the paramagnetic species, for example in solution, can average the anisotropies to zero.

The expression for the hyperfine interaction in the spin Hamiltonian is given by

$$\mathcal{H}_{\text{hf}} = \hbar \underline{\underline{S}} \cdot \underline{\underline{T}} \cdot \underline{\underline{I}} \quad (4-13)$$

where $\underline{\underline{T}}$ is a tensor representing the coupling between the electron and nuclear spin angular momentum vectors, $\underline{\underline{S}}$ and $\underline{\underline{I}}$, and is a combination of both dipolar and contact terms. The dipolar term may be written as

$$\mathcal{H}_{\text{dip.}} = g_e g_I \beta_e \beta_I \frac{\underline{\underline{I}} \cdot \underline{\underline{S}}}{r^3} - \frac{3(\underline{\underline{I}} \cdot \underline{\underline{r}})(\underline{\underline{S}} \cdot \underline{\underline{r}})}{r^5} \quad (4-14)$$

and the contact or Fermi term written as

$$\mathcal{H}_{\text{cont.}} = A_0 \underline{\underline{S}} \cdot \underline{\underline{I}} \quad (4-15)$$

where

$$A_0 = - \left(\frac{8\pi}{3} \right) g_e g_I \beta_e \beta_I |\psi(0)|^2 \quad (4-16)$$

and $|\psi(0)|^2$ is the spin 'density' of the unpaired electron at the nucleus. Here g_I and β_I are the nuclear g factor and magneton defined correspondingly to those for the electron; $\underline{\underline{r}}$, the radius vector between the electron and nuclear moments; r , is the distance between them; and A_0 , the isotropic hyperfine coupling constant.

The tensor form of $\underline{\underline{T}}$ is identical to that previously described for $\underline{\underline{g}}$, although contributions from both dipolar and

contact interactions may be separated in each term. Thus

$$\underline{\underline{T}} = \begin{pmatrix} T_{xx} & T_{xy} & T_{xz} \\ T_{yx} & T_{yy} & T_{yz} \\ T_{zx} & T_{zy} & T_{zz} \end{pmatrix} \quad (4-17)$$

and

$$T_{ij} = A_o \delta_{ij} + B_{ij} \quad (4-18)$$

In general, the hyperfine interaction (of the order $0 - 10^{-2} \text{ cm}^{-1}$) is found to be smaller than the Zeeman levels, each level being split into $2I+1$ sublevels.

4.1.3 Other Interactions.

Nuclear quadrupole interactions are even smaller in magnitude but on occasion may have to be included to explain EPR results satisfactorily. For nuclei with spin $I > \frac{1}{2}$, the nuclear quadrupole interaction may be expressed by

$$\mathcal{H}_Q = \underline{\underline{I}} \cdot \underline{\underline{Q}} \cdot \underline{\underline{I}} \quad (4-19)$$

where $\underline{\underline{Q}}$ is again represented by a tensor, of the same form as for $\underline{\underline{g}}$ and $\underline{\underline{T}}$. The effect is a small but calculable shift of the hyperfine lines.

The last term to be mentioned is the interaction of the nuclear moments with the magnetic field, the nuclear Zeeman interaction, expressed as

$$\mathcal{H}_{IH} = - g_I \beta_I \underline{\underline{I}} \cdot \underline{\underline{H}} \quad (4-20)$$

All symbols are as defined previously. This term is also generally small and may be ignored in a first order treatment.

4.1.4 EPR Spectra.

The anisotropies present in both the g factor and the hyperfine splittings cause the EPR spectrum to depend on the orientation of the species under consideration with respect to the external magnetic field. Studies of oriented species in single crystals are necessarily lengthy and often require considerable refinement of experimental procedure and mathematical analysis to achieve a high degree of precision in the evaluation of the g and hyperfine tensors.

If the paramagnetic molecules are contained in a polycrystalline or amorphous host, as is usually the case in studies on surfaces, the observed EPR spectrum will be a complex superposition of lines due to all orientations of the randomly oriented molecules. This is not necessarily to say that the molecules are themselves randomly oriented with respect to the surface, but rather the adsorption sites are randomly oriented. Information can be obtained from such observations and is generally achieved by computing spectral line shapes for a number of commonly occurring conditions for known or guessed principal values of the g and hyperfine tensors. The principal values are those obtained on diagonalization of the respective tensors.

Sands [66] obtained a resonance lineshape by assuming a random distribution of spin orientations, and then averaging the

resonant magnetic fields over all orientations. Similar methods of calculating these so-called powder or polycrystalline spectra have been developed by Bloembergen and Rowland [67], Kobin and Poole [68] and Kneubuhl [69].

In deriving theoretical lineshapes for these media, completely random orientation with respect to the external magnetic field on a macroscopic scale is assumed. Thus the microscopic environment may be ordered or disordered without affecting the validity of the calculations.

Following the treatment of Sands [66], an example of a calculation of a powder lineshape for an axially symmetric case is outlined. For the resonance condition given in equation (4-1), we have

$$g = (g_{//}^2 \cos^2 \theta + g_{\perp}^2 \sin^2 \theta)^{1/2} \quad (4-21)$$

where θ relates the position of the g tensor to the applied magnetic field (see figure 16, page 75). Here g_{xx} , g_{yy} , g_{zz} are the principal g values and $g_{xx} = g_{yy} = g_{\perp}$ and $g_{zz} = g_{//}$. Since all orientations are equally probable, one must sum over all the absorptions. With the frequency ν constant and sweeping the magnetic field H , then absorption of energy will occur at fields given by

$$H = \frac{h\nu}{\beta} (g_{//}^2 \cos^2 \theta + g_{\perp}^2 \sin^2 \theta)^{-1/2} \quad (4-22)$$

for each θ . The number of spins N having an orientation with respect to the applied magnetic field between θ and $\theta + d\theta$ is

given by

$$dN = (N_0/2) \sin\theta d\theta \quad (4-23)$$

where N_0 is the total number of spins. This becomes, from equation (4-22)

$$dN = (N_0/2) (4H_0^2/H^3) [(g_{\parallel}^2 - g_{\perp}^2) [2(H_0/H)^2 - g_{\perp}^2]]^{1/2} dH \quad (4-24)$$

where $H_0 = h\nu/2\beta$. A plot of dN/dH vs H yields the expected powder spectrum. Plots of this and also of anisotropic cases are given in Chapter Seven.

CHAPTER FIVE

ADSORPTION STUDIES

As introduced earlier, many spectroscopic techniques have found wide use in adsorption studies. Reviews involving some of the more common techniques have been given in the introduction. This chapter will be concerned with studies using the EPR technique and their application to the surfaces under consideration. The list of studies given is by no means complete, but yields enough insight into the scope of EPR in this area.

Ideally, one may expect to obtain three types of information from spectroscopic experiments:

1. The identity of the active sites on the surfaces
2. The identity of physically adsorbed or chemisorbed species
3. The nature of the interaction between an active site and an adsorbed molecule.

The term 'active site' is broadly defined. It can be a site on a surface capable of adsorbing molecules from the gas phase, or can refer to specific sites which induce chemical reactions. It is often difficult to distinguish between them.

No spectroscopic technique is universally applicable for obtaining all three types of information. Magnetic resonance techniques are most useful in obtaining information of type 1 although it is possible in some cases to obtain types 2 and 3 also. EPR techniques hold considerable promise of elucidating some of the complicated and confusing situations that arise on surfaces in systems involving the gas-solid interface.

Studies of the nature of surfaces themselves, prior to any adsorption, comprised much of the earlier work of the EPR technique in this area. Low temperature studies of various carbon samples gave narrow EPR signals due to various free radicals present on the surface [70,71]. Further studies of the effects of added gaseous oxygen to these samples (for example [72-74]) produced various RC - O - O radicals. Not all radical centers are necessarily on the surface; however, these reactions with oxygen presumably involve radicals at the interface. Most studies of this type have as their main interest internal rather than surface effects and consequently will not be discussed here. More recent studies of this type have involved the use of radiation and the study of the defects formed in various substances [75-78]. EPR techniques here provide very useful information about the type of defect, its environment and crystal field symmetry.

5.1 EPR Studies of Radicals on Surfaces.

5.1.1 Non-Zeolitic Adsorbents.

Many of the earlier studies of paramagnetic species on surfaces were done on glasses, silica gels, aluminas, semiconductors, and various catalytic surfaces. An early study by Faber and Rogers [79] involved adsorption of manganese (II), copper (II), and oxy-vanadium (IV) on various cation and anion exchange resins, activated charcoal, zeolite and silica gel. Their purpose was an attempt to further understand the bonding and environment of transition ions in unknown surroundings on the basis of their EPR spectra.

Russian workers carried out studies of free radicals produced on silica gel surfaces in the early 1960's. Hydrogen atoms were produced by low temperature γ -irradiation of the silica gel surface, the atoms being produced from the adsorbed water molecules or from the surface hydroxyl groups [80-82]. The hydrogen atoms formed were stabilized on the surface and the influence of the surface on the EPR parameters studied. The magnitude of the hyperfine splitting was found to agree closely with values for a free hydrogen atom although the width of the components varied with the nature of the surface under study. This suggests that the 'binding' of the atoms to the surface must occur without significant change in the spin density of the unpaired electron in the atom. A definite interaction, however, between the surface and the atom is indicated by linewidth variations depending on the type of surface. Accurate quantitative analysis of these effects was not thought possible

owing to the lack of reliable data concerning the surface structure of such solids. Wide variations in surface properties exist among various silica gels [83], the differences being caused by concentration of surface hydroxyl groups and differing degrees of surface regularity or crystallinity. Other free radicals have been stabilized on silica gel surfaces, notably ethyl and methyl [84-88], in each case the radical being formed on irradiation of adsorbed molecules on the surface.

The stabilization of free radicals at the surface of solids is of considerable interest in regard to heterogeneous catalysis and surface structure; EPR techniques have provided valuable information to both areas. Benzene adsorbed on silica gel, when irradiated with ultraviolet light, produced phenyl radicals, benzene cation radicals and benzene cation dimer radicals [89]. Radiolysis of monocarboxylic acids adsorbed on silica gel [90] has been studied using the EPR technique to obtain information concerning the radicals produced in the adsorbed state and also the nature of their thermal motion. Monomeric and dimeric cation radicals have also been observed in γ -irradiated benzene-silica gel systems [91]. Other radical ions have also been formed by direct interaction of adsorbates with the solid [92-93]. These are generally produced as a result of electron transfer from the adsorbent to the adsorbate having a high electron affinity.

Porous Vycor glass has also provided a convenient stabilizing medium for free radicals. Turkevitch and Fujita [94] reported the stabilization of the methyl radical at room temperature

and studied its reactivity with various added gases. Further studies [95-97] of the methyl radical on porous glass have been carried out and results have indicated both physically trapped radicals and those which have interacted with surface sites. The aim was to explore the general usefulness of porous glass as a free radical host and/or the relationship between a possible catalyst and free radical host. A novel type of methyl radical trapped in porous Vycor glass at 77°K has recently been reported, having an extremely small hyperfine coupling constant compared to that of the planar methyl radical, probably indicating a non-planar structure for the adsorbed radical [98].

As mentioned previously, workers in the area of heterogeneous catalysis have extensively employed the EPR technique. Knowledge of the mechanisms of heterogeneous catalysis may be obtained from investigations of the elementary acts involved, and of the structures and properties of intermediates taking part in catalytic reactions. The resonance signal can provide evidence as to the nature of the paramagnetic species on or in the surface and also as to the structure and chemical composition of the catalyst. Variations in the signal produced by different methods of preparation and processing may also provide information on the catalyst structure and the nature of the chemical bonds formed on adsorption.

Another possibility of applying EPR to heterogeneous catalysis problems is also available. This would involve the study of chemical reactions and of the adsorption process with a view

to obtaining signals from labile intermediate products on the catalytic surface. Petcherskaya et al [99] have shown the EPR method to be applicable in investigations of crystalline properties, chemical composition and electronic properties of various oxide catalysts. Similar studies and reviews thereon have been published [100,101].

5.1.2 Zeolite Adsorbents.

Various zeolites have found widespread use as adsorbents mainly due to the crystallographically well-defined structure and also to some knowledge of the electronic properties of the surface. As mentioned in an earlier chapter, a very important characteristic of zeolites is that it is possible to vary the electronic structure of the surface by a simple substitution of various cations of different sizes and charge while the lattice remains unchanged. The location of the cations can be assumed to be the same, provided there is not a large size difference. Stamires and Turkevitch [102] studied γ -irradiated synthetic zeolites varying the Si/Al ratio. Most of the defects produced are paramagnetic centers and EPR has proved useful in providing information about the type of defect and its environment. The same authors [103] also studied the adsorption of a number of molecules on these zeolites. Electron charge-transfer complexes were found when molecules with low ionization potentials were adsorbed. The purpose of the study was to examine the zeolites as acceptors in reactions of this type, and because of their crystalline structure, show the existence of well-defined

electron accepting sites in the lattice.

Studies of radical cations formed on the adsorption of aromatic hydrocarbons on zeolites are also present in the literature (for example [104]). Radicals produced by irradiation of adsorbed species have also been investigated. Electron irradiation of mesitylene adsorbed on 13X produced several radicals [105].

Adsorbed O_2^- species on various Y type zeolites have also been studied (for example [106,107]). The highly reactive methyl radical has been trapped in a zeolite matrix and stabilized for long periods at temperatures below 90°K [108]. The radical was generated by γ -irradiation of methane on type A zeolite. The free radical NO_3 was produced by the direct reaction of NO_2 and atomic oxygen and trapped within the sieve cavities of 13X [109].

The catalytic properties of molecular-sieve zeolites have been recognized for many years, but intensive investigation has gotten under way only within the last two decades. Zeolites are suggested as catalysts in such reactions as cracking isomerization and alkylation [110]. EPR can be used for structural determinations of the catalysts, which helps to identify the catalytic centers.

5.2 Special Adsorption Effects.

Physical adsorption is a reversible process and molecules so adsorbed may be easily removed from the surface by pumping. Chemisorption usually involves stronger forces and is often irreversible at moderate temperatures. Weak chemisorption is often indistinguishable from physical adsorption. Perturbation of the

adsorbed molecules, distinct from a chemical reaction between the surface and adsorbate, is generally considered to be a physical adsorption process.

The rotational freedom of physically adsorbed molecules is an important factor to be considered. Depending on the adsorbing temperature, the adsorbed molecule may have no axis of free rotation, possibly free rotation about an axis perpendicular to the surface or, even free rotation, about three mutually perpendicular axes. The possibility of hindered rotation about any or all these axes is also to be considered and in many cases appears to be important. The orientation of the adsorbed molecules is also of importance. This depends on the various adsorption forces present in a given adsorbate-adsorbent system. If the surface or cavities of the adsorbent are considered as the host matrix to the adsorbed molecules then it is clear the matrix can have a pronounced effect on the molecule. This necessarily affects the EPR spectrum and it may possibly affect the spectrum recorded by any other spectroscopic technique. These will be termed matrix interactions and will be discussed in more detail when the experimental results are interpreted.

Other adsorption effects need also to be considered. Electrostatic forces play an important role in physical adsorption. The equations of electrostatics, given by equations (2-11) and (2-12) in Chapter Two, may be applied to the adsorption of gases on zeolitic molecular sieves. The separation of molecules by these sieves is due in large part, not to the size of the molecules, but by electrostatic forces between the adsorbate and the strong electric

fields present in the sieves. It is these electric fields which will be discussed at present.

King and Benson [111], in explaining the low temperature adsorption of the hydrogen isotopes on alumina, have shown that the adsorbent has very strong surface electric fields, distributed over various sites on the surface. They have successfully used equations (2-11) and (2-12) for their results. The fields were found to arise from normal structural vacancies in the crystal lattices, vacancies which were present to maintain electrical neutrality. These same authors also found evidence [112] that electrostatic interactions also play a dominant role in the physical adsorption of gases on zeolites. It was found that o- and p-hydrogen could be separated on synthetic zeolites 5A and 13X. In this case, separation must be related to some type of hindered rotation since these species differ only in rotational energy. Strong electrostatic forces can produce such large barriers to rotation. The origin of these electric fields was then investigated. It was found that the cations, because of their local uncompensated charge, produce very strong electric fields and these cations serve as the adsorption sites. Thus the sieving properties of these 'molecular sieves' are due only in part to the size of the cages and channels present in the lattice.

The cation density of the unit cell of zeolites can be varied systematically by varying the AlO_4 content with respect to the SiO_4 content between well-defined limits. Removal or substitution of the cations can also create changes in the sites available for

adsorption. Rabo et al [113] studied the effect of the cation on the catalytic activity of various synthetic zeolites by comparing the sodium form, the calcium form and the decationized form of the zeolites. They found a positive relationship between the number of cation sites and the catalytic activity. Further reports by these and other workers have substantiated the importance of these large electrostatic fields of the cations as adsorption and catalytic centers [114,115]. The polarization of the adsorbed molecules by the electrostatic fields has also been suggested as being associated with the catalytic activity of the zeolites. Calculations by Hoijsink [116,117] on the polarization of aromatic molecules in a linear electric field give support to this hypothesis. Gibbons and Barrer [118,119] have calculated the electrostatic energy contributions to adsorption energies for molecules with both dipole and quadrupole moments for various cation exchanged zeolites. It was thus possible to see the effect of size and charge of the cations on these energies.

Adsorption according to these electrostatic models of interaction between the adsorbate and the strong electric fields present in the zeolites can also predict the preferred orientation of the molecules on the surface. The electric field normal to the surface will act in the direction of greatest polarizability and cause this to be the preferred orientation. Polar molecules should then be readily oriented by the internal fields of the solid and one should be able to predict this orientation. The molecules would also be assumed to execute small oscillations about an equilibrium position with respect to the surface.

CHAPTER SIX

EXPERIMENTAL

6.1 Vacuum System.

The materials used in this study were handled in a pyrex glass vacuum system constructed in the Chemistry department glassblowing shop at U.B.C. Teflon stopcocks with 'viton' O-rings were used in the gas handling part so as not to introduce impurities via reaction with any stopcock grease. The stopcocks were manufactured by Ace Glass Incorporated, Vineland, New Jersey. Where grease was necessary, a Halofluorocarbon lubricant, KEL-F #90 grease, a product of 3M Company, was used. KEL-F is quite unreactive to most corrosive or reactive chemicals. Pumping was via a 'Veeco' oil diffusion pump backed by a Welsch Duo Seal rotary pump. The ultimate vacuum was of the order of 10^{-6} torr. Both an NRC Thermocouple vacuum gauge and an NRC Ionization gauge were used as

pressure measuring devices. An NRC Model 831 detector was used in conjunction with these gauges. A diagram of the vacuum system is given in figure 13a.

6.2 Sample Tubes.

Figure 13b shows the sample tubes used in the experiments. Quartz tubing of 4 mm. outer diameter was used for the part of the tube to be placed in the EPR spectrometer. The diameter was determined by the size of the liquid nitrogen dewar to be used for low temperature experiments. A teflon stopcock was used here also to prevent any possible reactions of the sample with grease. Glass wool plugs were placed above the sample and in the constriction to prevent possible scattering of the sample during evacuation. A small cylindrical furnace was used which fit around the sample tube. The furnace was capable of temperatures in excess of 673°K .

6.3 Adsorbents.

The Linde Division of the Union Carbide Corporation kindly supplied samples of the synthetic zeolites 4A, 5A, 10X and 13X. The samples were white powders, and did not have any added binders. The usual commercial form of these zeolites is pellets of various size and a clay binder is added to facilitate the molding. As an adsorption material, the binder is relatively inert but may introduce unknown impurities [120]. Generally, the pellets are approximately 15 per cent binder, so these special samples were requested. The lot number for the 4A is 470017; the 5A, M580031; 10X, 1080001; and 13X, 1370014.

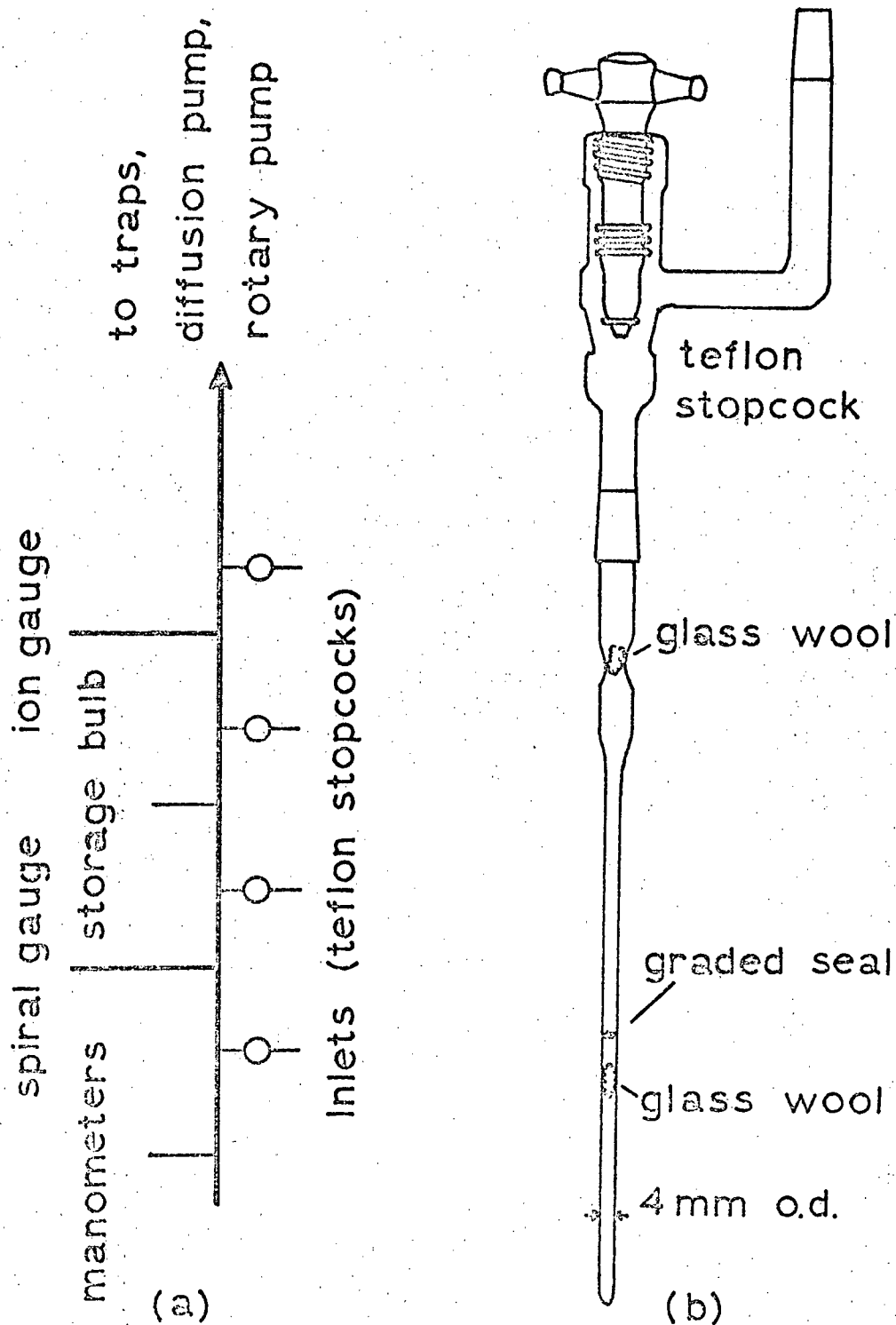


FIGURE 13. a) A schematic diagram of the vacuum system used in these experiments.

b) The sample tubes used in these experiments.

The synthetic mordenites (Zeolons) were supplied by the Norton Company of Worcester, Mass., in the same form as were the Linde products. The lot number of the sodium mordenite is HB 79-80E and that for the hydrogen mordenite, HB 91-92E.

The silica gel samples used were of a thin layer chromatographic sorbent marketed by the Mallinckrodt Chemical Works. The brand name is SilicAR TLC-7GF.

The ions in the Linde synthetic zeolites were exchanged following standard procedures. Sherry [121] gives an account of the exchange properties of various zeolites and also describes the conditions required for a number of specific exchanges.

6.4 Sample Preparation.

Sample tubes containing the adsorbents were degassed for a period of generally 4-6 hours at a temperature of approximately 523°K at a pressure of less than 5×10^{-5} torr. This period was sufficient to remove any water from the adsorbents. The gases to be studied were then adsorbed onto the surfaces at room temperature for several minutes. The pressure of gas adsorbed varied for the different systems and will be given in each appropriate section.

EPR spectra were recorded at 77°K on the spectrometers to be described later in this chapter. A Varian V-4546 liquid nitrogen dewar, shown in figure 14b, was used for the low temperature studies. The dewar was fabricated entirely from selected quartz to pass ultraviolet light with a minimum of background signals.

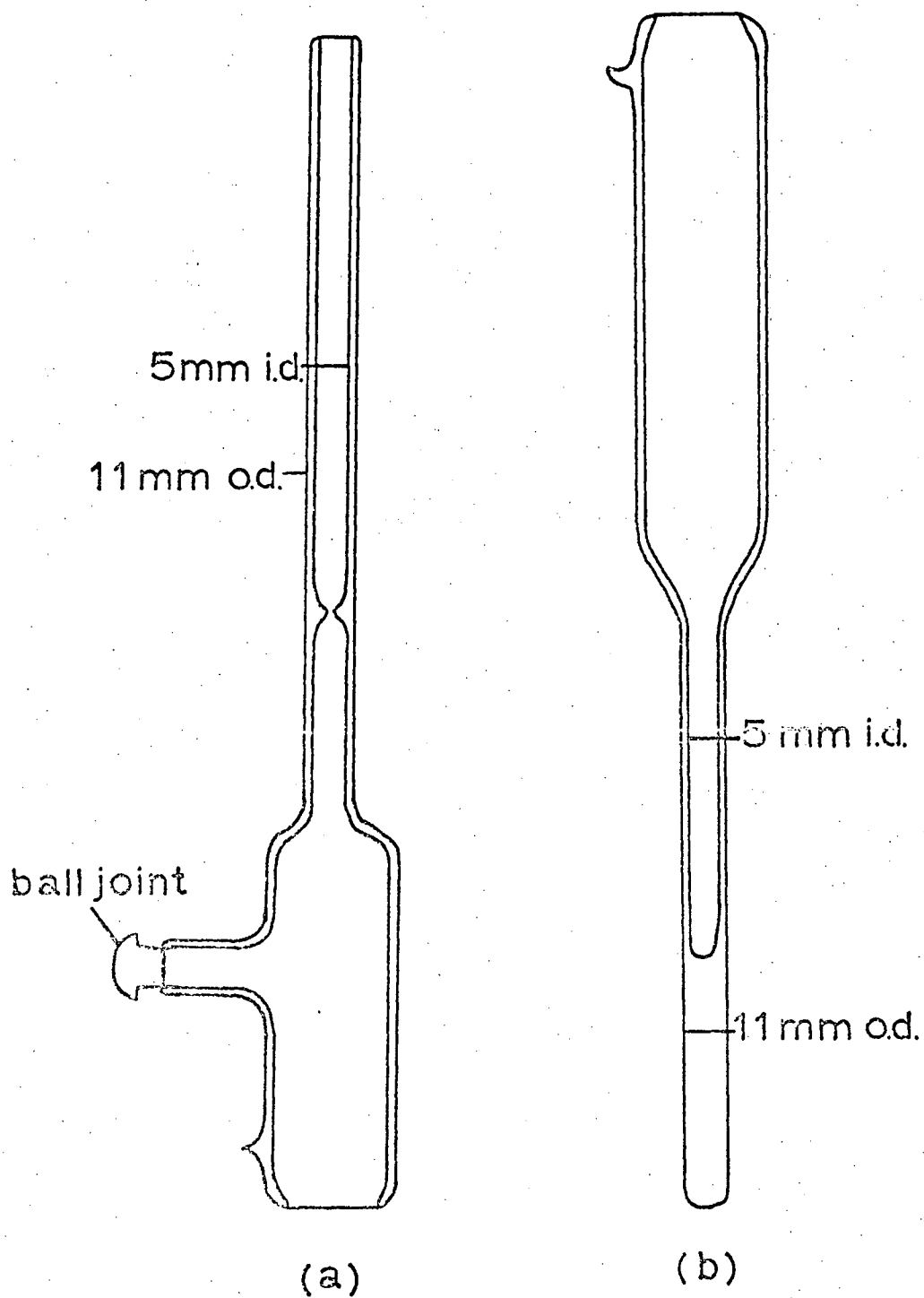


FIGURE 14. a) Quartz dewar used for variable temperature EPR experiments.

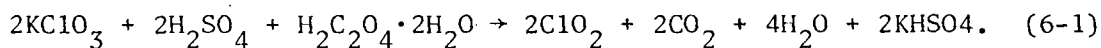
b) A Varian V-4546 liquid nitrogen dewar.

Variable temperature experiments were performed using a specially designed quartz dewar, shown in figure 14a. Dry nitrogen gas was passed through a heat exchanger placed in a large dewar filled with a coolant such as liquid nitrogen or a dry ice-acetone mixture. The gas was cooled to the approximate temperature of the coolant and passed through the quartz dewar, cooling the sample. The temperature at the sample was controlled by the rate of flow of the gas and was measured using a copper-constantan thermocouple. The wave guide near the cavity was kept free from condensed moisture by passing dry nitrogen gas through it.

6.5 Gases.

6.5.1. Chlorine Dioxide ClO_2 .

The chlorine dioxide used in this study was kindly supplied by Professor F. Aubke of this University. In his method of preparation [122], a mixture of 12.2 gm. of potassium chlorate, 10 gm. oxalic acid and a chilled solution of 10.8 gm. of concentrated sulfuric acid in 40 ml. of water was slowly heated on a steam bath (the mole ratio $\text{KClO}_3 : \text{H}_2\text{C}_2\text{O}_4 \cdot 2\text{H}_2\text{O} : \text{H}_2\text{SO}_4$ was 1:0.8:1.1). The reaction is characterized by the following equation:



The ClO_2 and CO_2 produced were passed through a P_2O_5 drying tube and cooled to 195°K . Pumping on the sample at this temperature removed the CO_2 . Further purification was achieved through a trap to trap distillation from 195°K to 77°K . The ClO_2 was stored in a dry ice-

trichloroethylene bath at 195°K.

6.5.2. Nitrogen Dioxide NO₂.

The nitrogen dioxide used in this study was purchased from Matheson of Canada, Limited. The purity of the gases in the containers was > 99.5 percent. Further purification was achieved by pumping on the solidified gas in a container immersed in a dry ice-acetone bath. The purified gas was stored in a glass sample bulb.

6.5.3 Nitric Oxide NO.

The nitric oxide, ¹⁴NO, was purchased from Matheson of Canada, Limited, and the reported purity is > 98.5 percent. The gas was passed through a trap immersed in an isopentane-pentane-dry ice bath at approximately 133°K and stored in a glass sample bulb. Further purification was achieved by pumping on the sample at liquid nitrogen temperature.

The ¹⁵N substituted sample of nitric oxide was purchased from the Isomet Corporation, New Jersey and had a reported purity of > 99.3 percent ¹⁵NO.

6.5.4 Tetrafluorohydrazine N₂F₄.

The tetrafluorohydrazine used in this study was purchased from Air Products and Chemicals Incorporated, Pennsylvania. The research grade gas had a reported purity of > 99 percent and was used directly from the container without any further purification.

6.6 Spectrometers.

The majority of the measurements were carried out on a Varian E-3 X-band EPR spectrometer system. The operating frequency of the klystron is 8.8 to 9.6 GHz transmitted to the cavity through a 4-port circulator. The magnetic field of this system was supplied by a four inch electromagnet having a usable air gap of 1.2 inches, capable of homogeneous magnetic fields in excess of 6 kilogauss. Homogeneity was such as to also resolve 70 mG lines. The magnetic field was modulated through a 100 kHz field modulation unit in this system. A Varian E-4531 cavity of rectangular mode TE₁₀₂ was used for the experiments. This spectrometer system has a calibrated field control and also calibrated frequency and power meters. The magnetic field intensity was measured as a function of the proton resonance in an NMR probe, while being frequency modulated by a magnetometer constructed by the Chemistry Department Electronics Shop. The magnetometer output was displayed on an Hewlett-Packard 5245L frequency counter. This counter was also used to measure the microwave frequency of the klystron by means of a 5255A frequency converter. A block diagram of this EPR system is shown in figure 15.

A portion of the experimental spectra was recorded using a Varian V-4500 100 kHz EPR spectrometer modified by the Chemistry Department Electronics Shop. The operating frequency is about 9 GHz. A standard Varian rectangular cavity, model V-4531 was used with this spectrometer. A maximum field of about 9 kilogauss was attainable from the Varian V-4012A 12 inch magnet having a 2.5 inch gap between

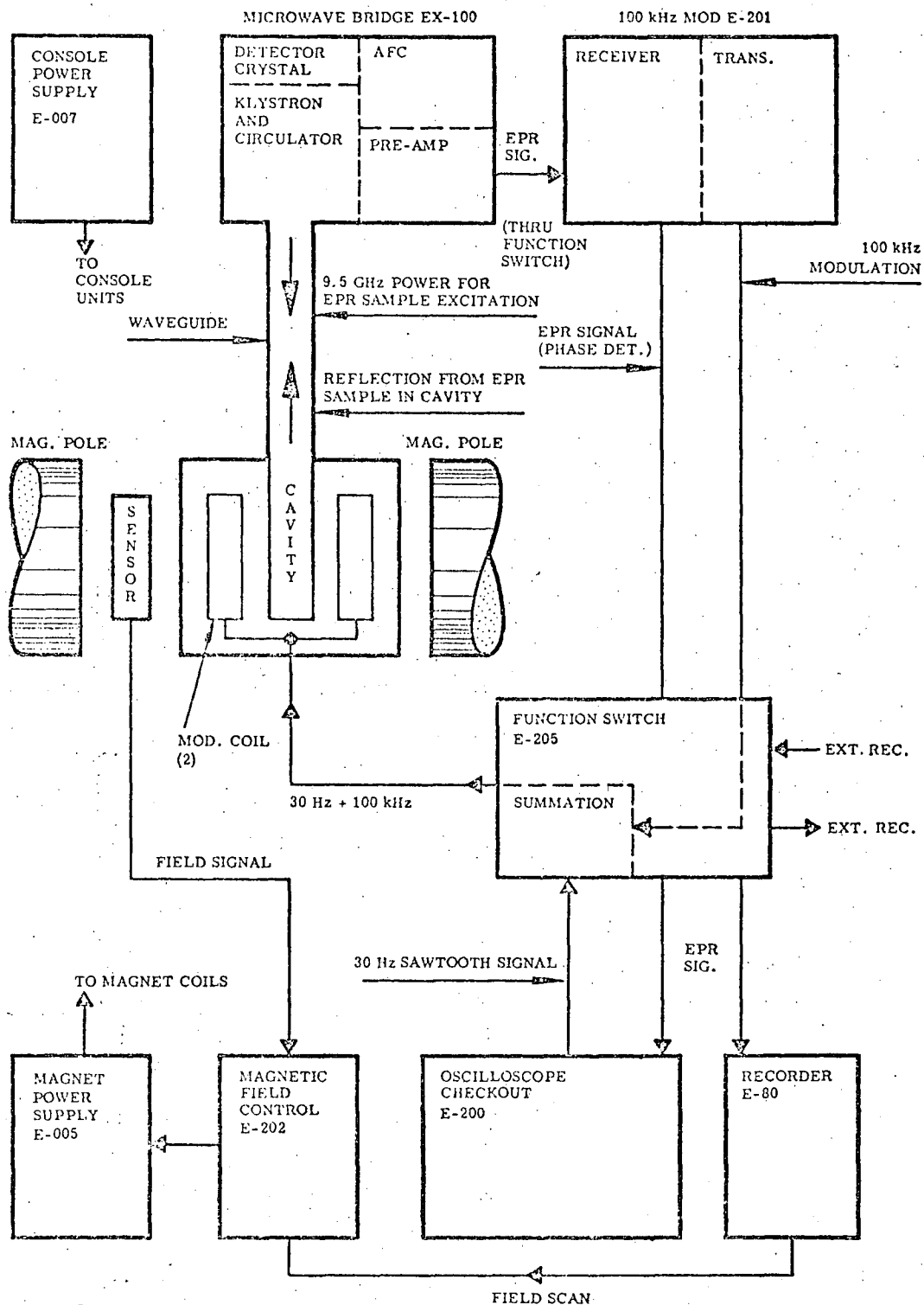


FIGURE 15. Block diagram of a Varian E-3 X-band Spectrometer system.

the poles. Frequency and field intensity measurements were performed as previously described.

Further measurements were carried out on a spectrometer similar to that just described, although a Varian V-3900 magnet capable of 15 kilogauss supplied the magnetic field. A Varian V-2501 Fieldail Mark II Magnetic Field Regulator controlled the magnetic field. The remainder of the spectrometer was essentially the same.

CHAPTER SEVEN

ANALYSIS OF ELECTRON PARAMAGNETIC RESONANCE SPECTRA

The task of assigning numerical values to the parameters in the spin Hamiltonian given by equation (4-10) can, in some cases, be quite formidable. The consistency of the assigned values must be checked through, generally by means of a theoretical calculation. Various methods used for the calculation of resonance fields have been reviewed by Swalen and Gladney [123], and some computer programs available to this end are discussed. Gladney [123,124] has written a program which, though restricted, is generally applicable to many EPR problems. Many papers have since been published on the subject [125-128].

A completely general and extremely versatile method of resonance field calculation has recently been published [129]. A method is proposed for calculating EPR transition fields for a general spin Hamiltonian with no restrictions. The method has also

been supplemented with the calculation of transition probabilities. The inclusion of a lineshape to the calculated resonance field positions enables one to simulate EPR spectra.

The EPR spectrum of a polycrystalline or powder sample involves a spatial average over different orientations of the spins with respect to the direction of the magnetic field, the resonance fields for each orientation being calculated usually by one of the aforementioned methods. A brief summary of a method given for solving the spin problem described by a spin Hamiltonian and the application of these results to the simulation of EPR spectra will be given for completeness. McClung [130] has recently published a simple method to solve a spin Hamiltonian for an orthorhombic paramagnetic center in a rigid lattice. The Hamiltonian is restricted in the sense that nuclear Zeeman and quadrupole terms are neglected and the g and hyperfine tensors are assumed to be simultaneously diagonalized in the same axis system. The solution is given for a paramagnetic species with electron spin $S=1/2$ and one nuclear spin I . Although somewhat less general in application, the technique is instructive.

The spin Hamiltonian is then

$$\mathcal{H} = \beta \underline{\underline{S}} \cdot \underline{\underline{g}} \cdot \underline{\underline{H}} + h \underline{\underline{S}} \cdot \underline{\underline{T}} \cdot \underline{\underline{I}} \quad (7-1)$$

where the symbols have been defined previously. Experimental data are not necessarily collected in a molecular coordinate frame, whereas (7-1) operates in a molecular frame. We must refer to some

experimental or laboratory frame of reference. A 'tensor frame' is defined as the axis system in which that tensor is diagonal. For our spin Hamiltonian, the g tensor frame is taken as the molecular frame. For this example, the T tensor is also diagonal in the molecular frame. Generally, Euler coordinate transformations are used to reduce the frames to the form wanted for study. These transformations correspond to rotation of the vector networks by the appropriate angles. This will often be the case when the molecule is in a host matrix such as a crystal and its molecular coordinates are implicitly defined with respect to the crystal axes. Appropriate transformations are also required when the g and hyperfine tensor frames are not coincident. In this case, generally the g tensor frame is taken as the molecular frame and the hyperfine tensor frame transformed accordingly.

McLung uses the following technique to solve the Hamiltonian. The electron spin operator, \underline{S} , is quantized along the direction of $\underline{g} \cdot \underline{H}$ to allow exact treatment of the Zeeman term. Quantization of the nuclear spin operator \underline{I} , along the direction of $\underline{T} \cdot \underline{S}$, then leads to an expression for the hyperfine interaction which is most suitable for a perturbation treatment. Figure 16 shows the relationships of the frames used. Generally \underline{H} is a large static magnetic field applied along the laboratory Z axis. (X, Y, Z) is the laboratory frame and (x, y, z) , the molecular frame. The angles θ and ϕ relate the position of the applied magnetic field to the g and T tensor frames (the molecular frame).

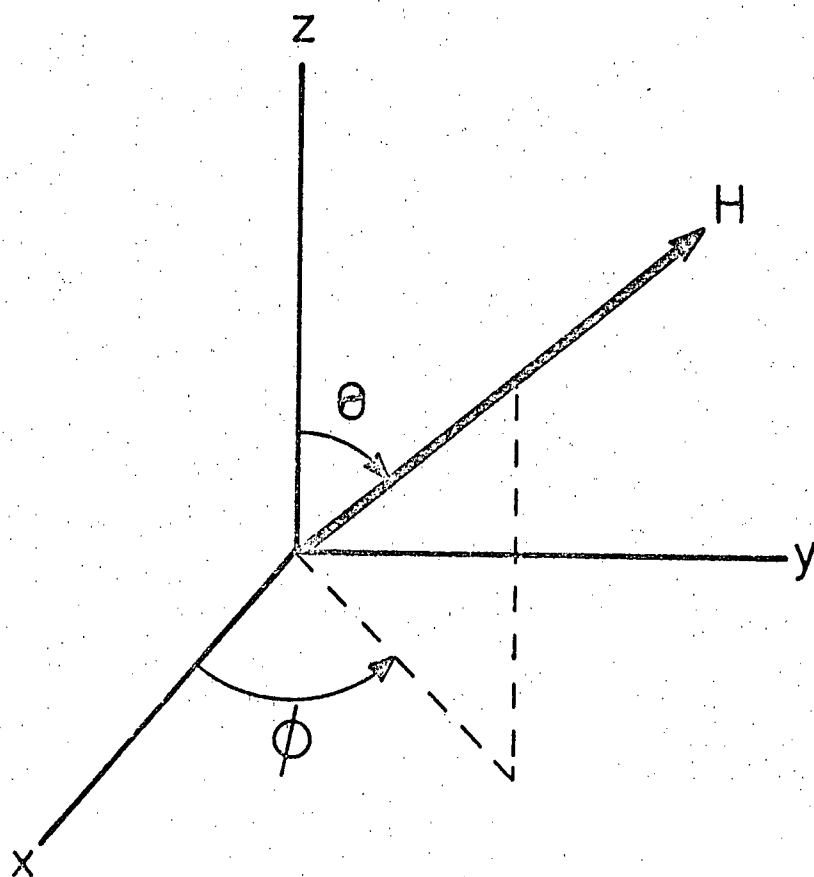


FIGURE 16. The molecular and magnetic field coordinate system.

The hyperfine term may generally be treated as a perturbation which splits the electronic Zeeman levels of the spin system. Using the zero-order basis functions

$$|S, M_S\rangle |I, M_I\rangle ,$$

second-order perturbation theory [131] yields the eigenvalues

$$\begin{aligned} E_{M_S M_I} = & g\beta_0 H_0 M_S + h T M_S M_I - \frac{h^2 T_{xx} T_{yy} T_{zz} [S(S+1) - M_S^2] M_I}{2g\beta_0 H_0 T} \\ & + \left[\frac{g_{zz}^2 (g_{\alpha}^2 T_{\alpha}^2 - g_{\alpha}^2 T_{zz}^2) \sin^2 \theta \cos^2 \theta}{g_{\alpha}^2 g^4 T^2} \right. \\ & + \left. \frac{g_{xx}^2 g_{yy}^2 (T_{xx}^2 - T_{yy}^2)^2 \sin^2 \theta \sin^2 \phi \cos^2 \phi}{g_{\alpha}^2 g^2 T^2} \right] \frac{h^2 M_I^2 M_S}{2g\beta_0 H_0} \\ & + \left[\frac{g_{\alpha}^2 T_{\alpha}^2 T_{zz}^2}{g_{\alpha}^2 T^2} + \frac{g_{\alpha}^2 T_{xx}^2 T_{yy}^2}{g_{\alpha}^2 T_{\alpha}^2} \right. \\ & + \left. \frac{g_{xx}^2 g_{yy}^2 g_{zz}^2 T_{zz}^2 (T_{xx}^2 - T_{yy}^2)^2}{g_{\alpha}^2 g^4 T_{\alpha}^2 T^2} \right] \cos^2 \theta \sin^2 \phi \cos^2 \phi \\ & + \frac{h^2 [I(I+1) - M_I^2] M_S}{4g\beta_0 H_0} \end{aligned} \quad (7-2)$$

$$\text{where } g = (g_{\alpha}^2 \sin^2 \theta + g_{zz}^2 \cos^2 \theta)^{1/2} \quad (7-3)$$

$$g_{\alpha} = (g_{xx}^2 \cos^2 \phi + g_{yy}^2 \sin^2 \phi)^{1/2} \quad (7-4)$$

$$T = (g_{\alpha}^2 T_{\alpha}^2 \sin^2 \theta + g_{zz}^2 T_{zz}^2 \cos^2 \theta)^{1/2} / g \quad (7-5)$$

$$T_{\alpha} = (g_{xx}^2 T_{xx}^2 \cos^2 \phi + g_{yy}^2 T_{yy}^2 \sin^2 \phi)^{1/2} / g \quad (7-6)$$

E_{M_S, M_I} are the eigenvalues of the basis functions named above; β_0 , the Bohr magneton; H_0 , the magnitude of the applied magnetic field; h , Planck's constant, with all other terms being previously defined. In the limit of axial symmetry, this result reduces to that of Bleaney (132).

Once the magnetic field H is computed for various values of θ and ϕ for the appropriate M_S and M_I values, it is possible to simulate the EPR spectrum. An appropriate line shape must be added to each transition, usually in the form of a Gaussian or a Lorentzian line shape. Mr. J.C. Tait of this laboratory has written such a program. Different programs may be used to generate the resonance fields for use in this program, the choice being determined by the complexity of the problem.

Considerable information is available from powder spectra, even though the observed EPR spectrum is a complex superposition of lines due to all orientations of the randomly oriented molecules. The major loss of information is derived from the fact that the orientation of the molecule in the host cannot be determined from the spectrum alone. Line-shapes of powder spectra have been discussed

by a number of authors and reference has been made to some of these in Chapter Four. Assuming that the g and hyperfine tensors are diagonalized in the same frame and considering, for the present, no magnetic nucleus in the molecule, figure 17 shows some generalized line-shapes. Figure 17a depicts the spectrum expected for a species with an axially symmetric g tensor, i.e. $g_{xx} = g_{yy} = g_{\perp}$ and $g_{zz} = g_{\parallel}$. The solid line denotes the idealized absorption and the broken line a possible real absorption. The real absorption, represented by some smoothly varying line-shape, consists of many sources of broadening. Figure 17b depicts the spectrum, both idealized and real, for a species with a fully anisotropic g tensor. It is readily seen that these complex line shapes contain a number of sharp, readily observable peaks. These correspond to molecules which are oriented so that the magnetic field lies along one of the principal axes of the molecule, the result being that the components of the g and T tensors are readily determined from the positions of these lines. The explanation lies in the fact that when the magnetic field lies along one of the molecular axes, the resonance field for the particular transition under study is a maximum or a minimum with respect to variations in θ and ϕ . This results in a piling-up of the number of randomly oriented molecules whose resonance fields are in the vicinity of one of the principal axes, and causes an abrupt and readily observable change in the intensity of the EPR absorption at these points.

When a magnetic nucleus is present in the molecule, the spectra are more complicated, but can generally be analyzed in terms of the absorption curves just discussed. Complications may arise

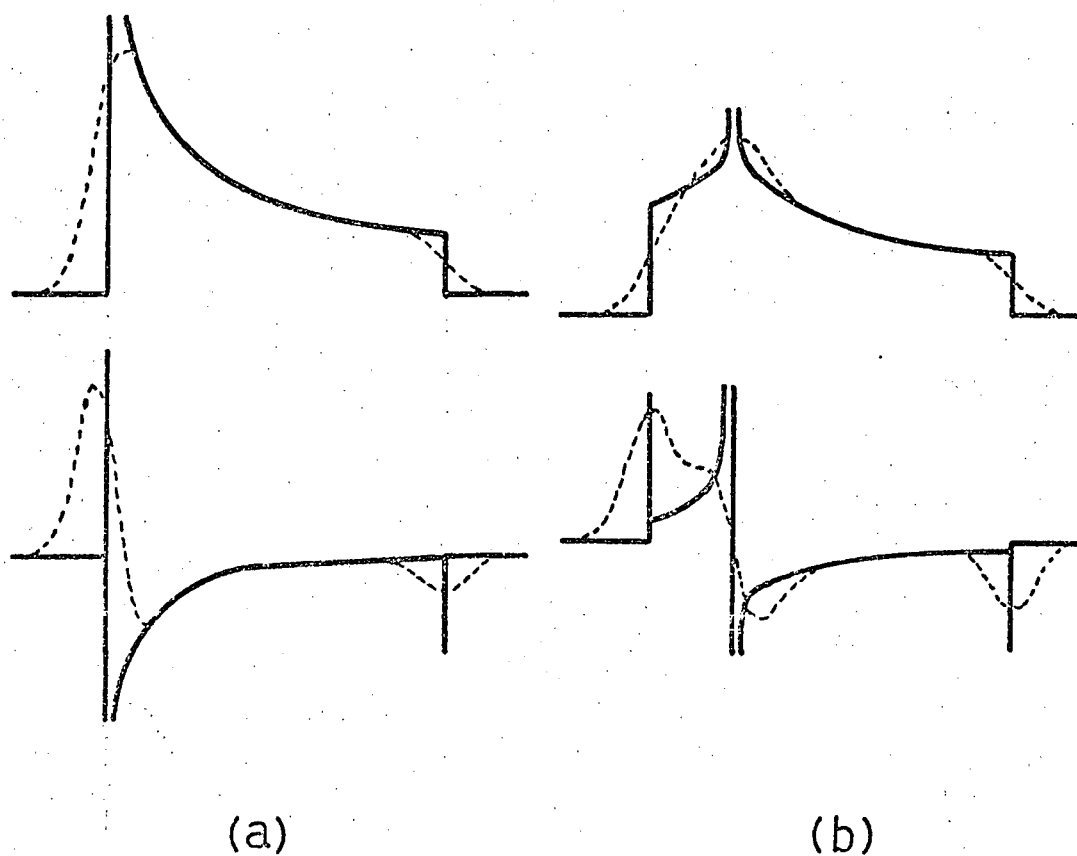


FIGURE 17. Generalized lineshapes of powder EPR spectra for a species with no hyperfine structure.

a) axially symmetric g tensor

b) fully anisotropic g tensor

through the appearance of extra lines owing to the occurrence of usually forbidden transitions, or due to stationarities caused when the g and hyperfine tensors try to shift the lines in opposite directions.

One can then, under favourable conditions, determine the components of the g and hyperfine tensors from a powder EPR spectrum. In complicated instances, approximate starting values for these tensors could probably be obtained from the spectra, and more precise determination done by fitting a computer simulated spectrum to the observed spectrum. Powder EPR spectra cannot provide information about the orientation of the principal axes of the g and hyperfine tensors with respect to the molecular axes, nor can information be obtained about which component is associated with a specific molecular axis. This must be determined by comparison with theoretical estimates of these quantities along the various molecular axes.

CHAPTER EIGHT

CHLORINE DIOXIDE, ClO_2

Chlorine dioxide is one of the few stable gases that is paramagnetic in its normal chemical state. The nuclear spin of the chlorine atom is $I = \frac{3}{2}$. Due in part perhaps to its extremely high reactivity, investigations using EPR techniques have not been extensive. Several years ago, Bennett and Ingram [133] reported the spectrum of ClO_2 in a dilute fluid solution of ethyl alcohol. The spectrum consisted of a broad line at room temperature, separating into four components on cooling. More recent studies of ClO_2 in various solvents at low temperatures have produced better resolved spectra, the resolution in some cases being good enough to distinguish the hyperfine splittings due to the ^{37}Cl isotope [134].

The spectrum reported in rigid sulfuric acid at 77°K is somewhat better resolved, although complex [135]. Here again, features

due to the ^{37}Cl isotope may be distinguished from those due to the predominant ^{35}Cl . Irradiated potassium perchlorate has provided a source of trapped ClO_2 molecules in the crystal environment. Two independent studies [136,137] of the ClO_2 molecule in such crystals have led to similar analysis of the spectra. The principal values of both the g and hyperfine tensors were obtained from these spectra whereas the rigid solution spectra could yield with certainty only one principal value of each of these tensors.

8.1 Silica Gel.

Silica gel was initially chosen as an adsorbent due in part to its high surface area and the fact that the silicon nucleus (except for ^{29}Si of natural abundance less than 5%) does not have a nuclear spin. This would provide a magnetically inert environment eliminating a possible source of line broadening. Adsorption of ClO_2 at room temperature at pressures higher than 8×10^{-3} torr produced a bright yellow colouring of the silica gel when cooled to 77°K . Spectra recorded for these pressures were composed of extremely broad lines indicating far too high a concentration of ClO_2 . To avoid dipolar broadening, less than a monolayer must be adsorbed. Pressures of less than 1×10^{-4} torr of ClO_2 produced much clearer spectra, with readily resolvable features. There was no colouration of the silica gel at these pressures. An equilibration time of up to 20 minutes was needed for maximum signal strength, indicating slow sorption of the ClO_2 molecules throughout the surface of the silica gel. The samples could be

stored at room temperature and re-cooled to 77°K with no loss of signal. Pumping at room temperature removes very little ClO_2 indicated by very little change in the spectrum, but the ClO_2 may be removed from the silica gel by pumping at higher temperatures.

The surface of the silica gel is not uniform, and a large variety of adsorption centers are possible with the possibility of 'densely' populated areas on the surface. This would account for the inability to observe spectra with a small enough linewidth to distinguish all the features clearly.

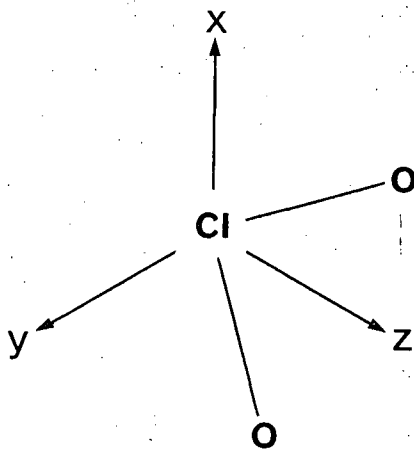


Figure 18

In conformity with earlier works, the axis system for the magnetic parameters of the ClO_2 has been chosen so that the z-axis lies along the two-fold symmetry axis, y is perpendicular to z in the plane of the molecule, and x, the third orthogonal axis (see figure 18).

Figure 19 shows a typical spectrum of ClO_2 adsorbed on silica gel, recorded at 77°K . Chlorine has two naturally occurring isotopes ^{35}Cl and ^{37}Cl in the ratio of approximately 3:1. Both isotopes have a nuclear spin of $I = 3/2$, and the ratio of their magnetic moments is 0.82089:0.68329. The observed spectrum is then essentially a superposition of two spectra, $^{35}\text{ClO}_2$ and $^{37}\text{ClO}_2$, with the ratio of the corresponding hyperfine components given by the ratio of the respective magnetic moments.

The values for the components of the hyperfine and g tensors were obtained by comparison of the recorded spectra to simulated EPR spectra using the various programs previously mentioned. The simulated spectrum is shown in figure 20. Both T and g were found to be anisotropic. The results are tabulated in Table 1.

The main distinguishable features of the spectrum are those associated with the x component of the hyperfine tensor, particularly those associated with $m_I = \pm 3/2$. These are the outer lines of the spectrum. Both the y and z components are concentrated in the central portion of the spectrum.

Figure 21 shows a spectrum of ClO_2 adsorbed on silica gel, recorded at room temperature. Features due to the isotopes are not discernable here. From the spectrum, the ClO_2 appears to be freely

TABLE 1

Reference	Hyperfine components (gauss) For $^{35}\text{ClO}_2$ only							Linewidth used for simulations (gauss)	Medium
	T_{xx}	T_{yy}	T_{zz}	A_o	g_{xx}	g_{yy}	g_{zz}		
137	79.9	-13.4	-12.5	18.0	2.0018	2.0167	2.0111		KClO_3 @ 77°K
137	72.7	- 9.6	-10.0	18.0	2.0025	2.017	2.011		H_2SO_4 @ 77°K
136	74.7	-10.8	-11.5	17.5	2.0016	2.01667	2.01214		KClO_4 @ 106°K
135	70.5				2.0015				H_2SO_4 @ 77°K
	± 0.2 GAUSS				± 0.0005				ADSORBED ON
this work	76.1	-17.0	- 7.9	17.1	2.0023	2.0123	2.0115	3.5	silica gel @ 77°K
this work	74.9	-16.7	- 7.8	16.8	2.0023	2.0123	2.0115		H-mordenite @ 77°K
this work	77.0	-17.2	- 8.0	17.3	2.0023	2.0123	2.0115	8.0	Na-mordenite @ 77°K
this work	82.2	-18.4	- 8.5	18.4	2.0023	2.0123	2.0115	2.5	4A @ 77°K
this work	81.6	-18.3	- 8.5	18.3	2.0023	2.0123	2.0115		5A @ 77°K
this work	84.5	-18.9	- 8.8	18.9	2.0023	2.0123	2.0115	2.0	13X site III @ 77°K
this work	77.5	-17.4	- 8.0	17.3	2.0023	2.0123	2.0115	2.0	13X site II @ 77°K
this work	79.0	-17.7	- 8.2	17.7	2.0023	2.0123	2.0115		10X @ 77°K
this work	77.2	-17.3	- 8.0	17.3	2.0023	2.0123	2.0115		LiX @ 77°K

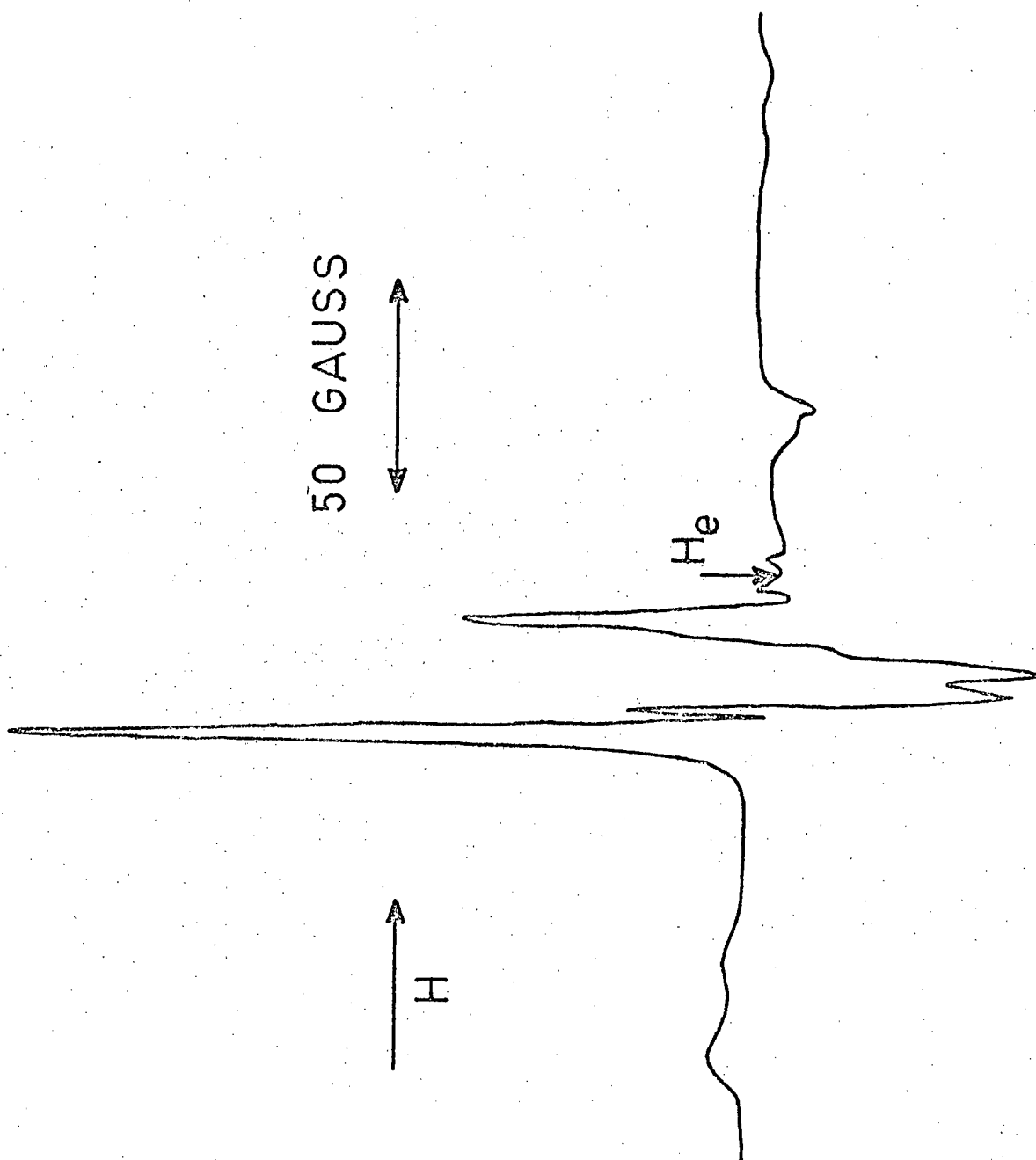


FIGURE 19. EPR spectrum of chlorine dioxide adsorbed on silica gel, recorded at 77° K.

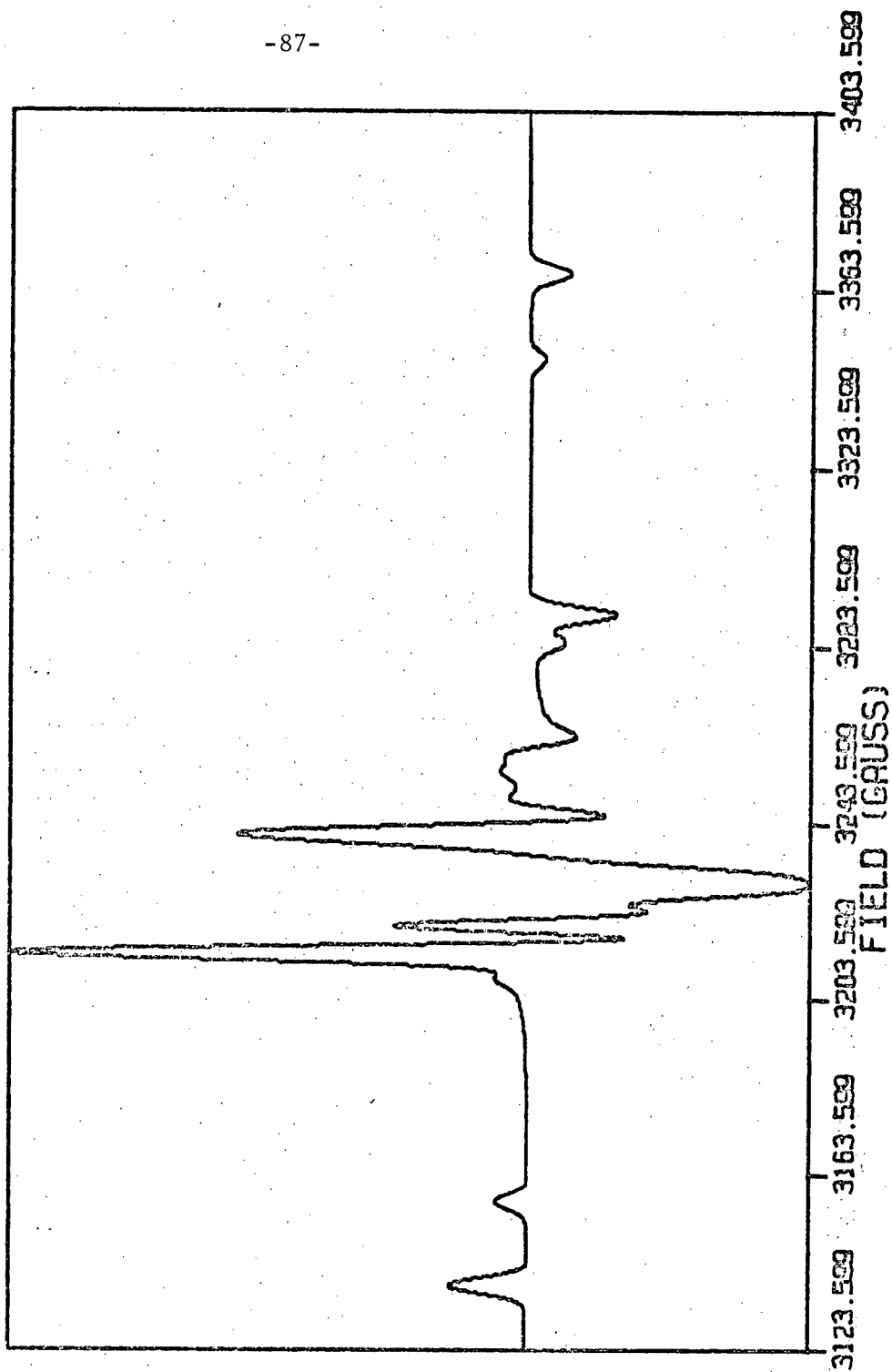


FIGURE 20. Computer simulated EPR spectrum of chlorine dioxide adsorbed on silica gel, recorded at 77° K.

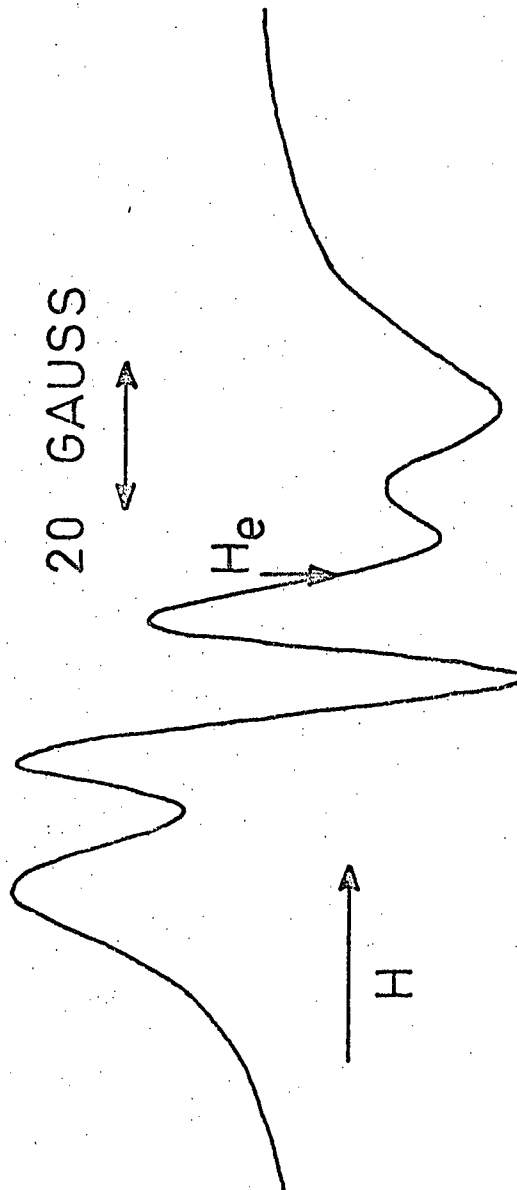


FIGURE 21. EPR spectrum of chlorine dioxide adsorbed on silica gel, recorded at room temperature.

rotating on the silica gel surface or in the pores, and the isotropic parameters are included in Table 1. A simulated spectrum is shown in figure 22.

8.2 Na and H-Mordenite.

ClO_2 adsorbed on H-mordenite and recorded at 77°K yields essentially an identical spectrum to that obtained on silica gel. The components of the hyperfine tensor are slightly different and are listed in Table 1. These, along with those associated with the other adsorbents, will be discussed later.

Na-mordenite produces some interesting results. Under similar conditions of sample preparation, the spectrum at 77°K appears much broader and cannot be improved by pumping. Unlike silica gel, the sample shows no colour. A typical spectrum is shown in figure 23. The x components of the hyperfine tensor are still readily discernable and the values are listed in Table 1. The spectrum recorded at room temperature, unlike that of silica gel, indicates that some features may have been partially averaged due to some motional process of the ClO_2 . The most likely would be a rotation about the z axis, averaging the hyperfine and g tensor components of the x and y axes. A spectrum simulated under these conditions however, does not match the observed spectrum (see figures 25 and 26). This suggests that the rotation is hindered. Spectra recorded at higher temperatures show only a decrease in signal height and it is likely diffusion of the ClO_2 molecules will occur at these elevated temperatures. At 373°K , the ClO_2 is completely removed from the Na-mordenite.

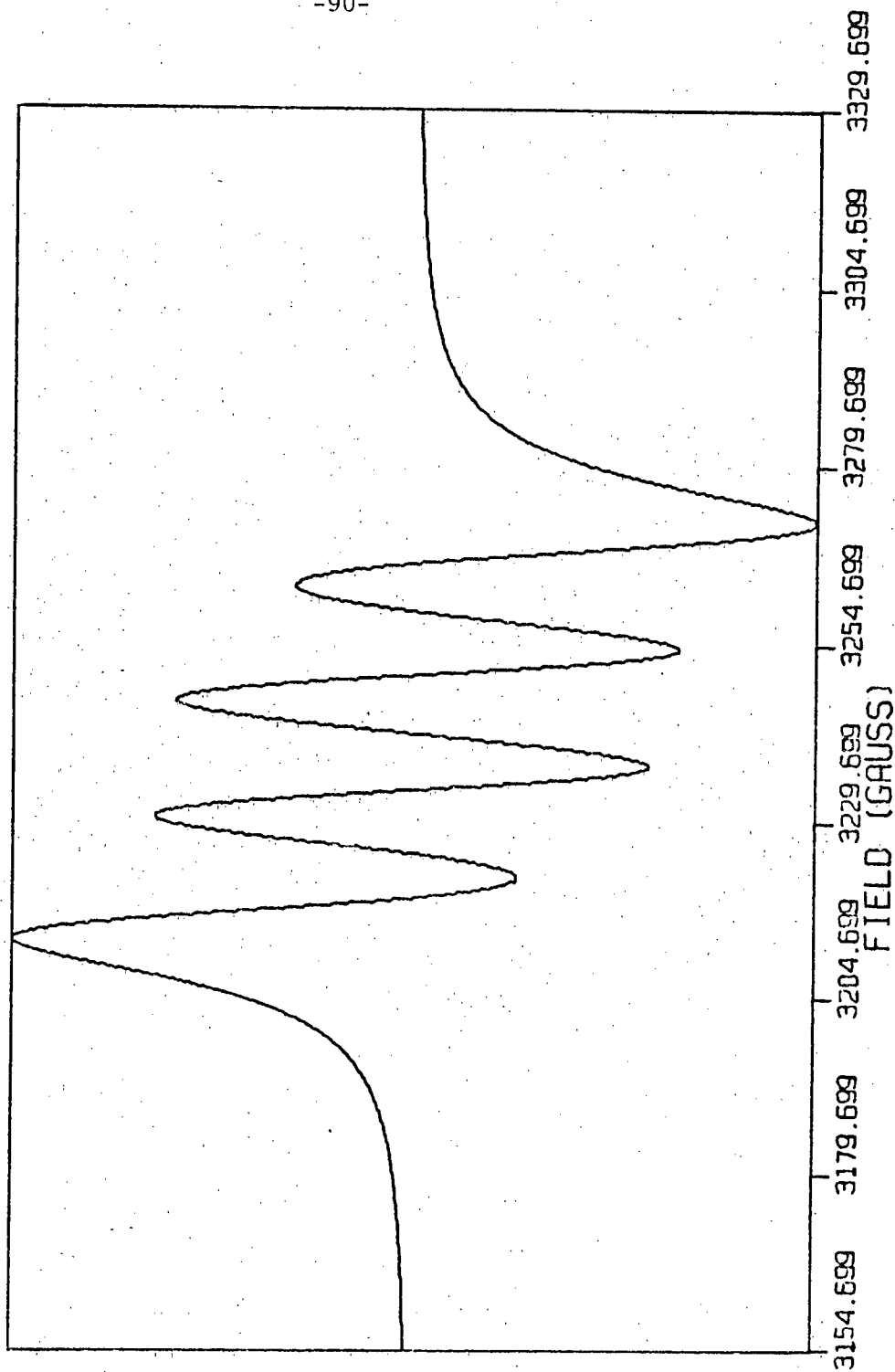


FIGURE 22. Computer simulated EPR spectrum of chlorine dioxide adsorbed on silica gel, recorded at room temperature.

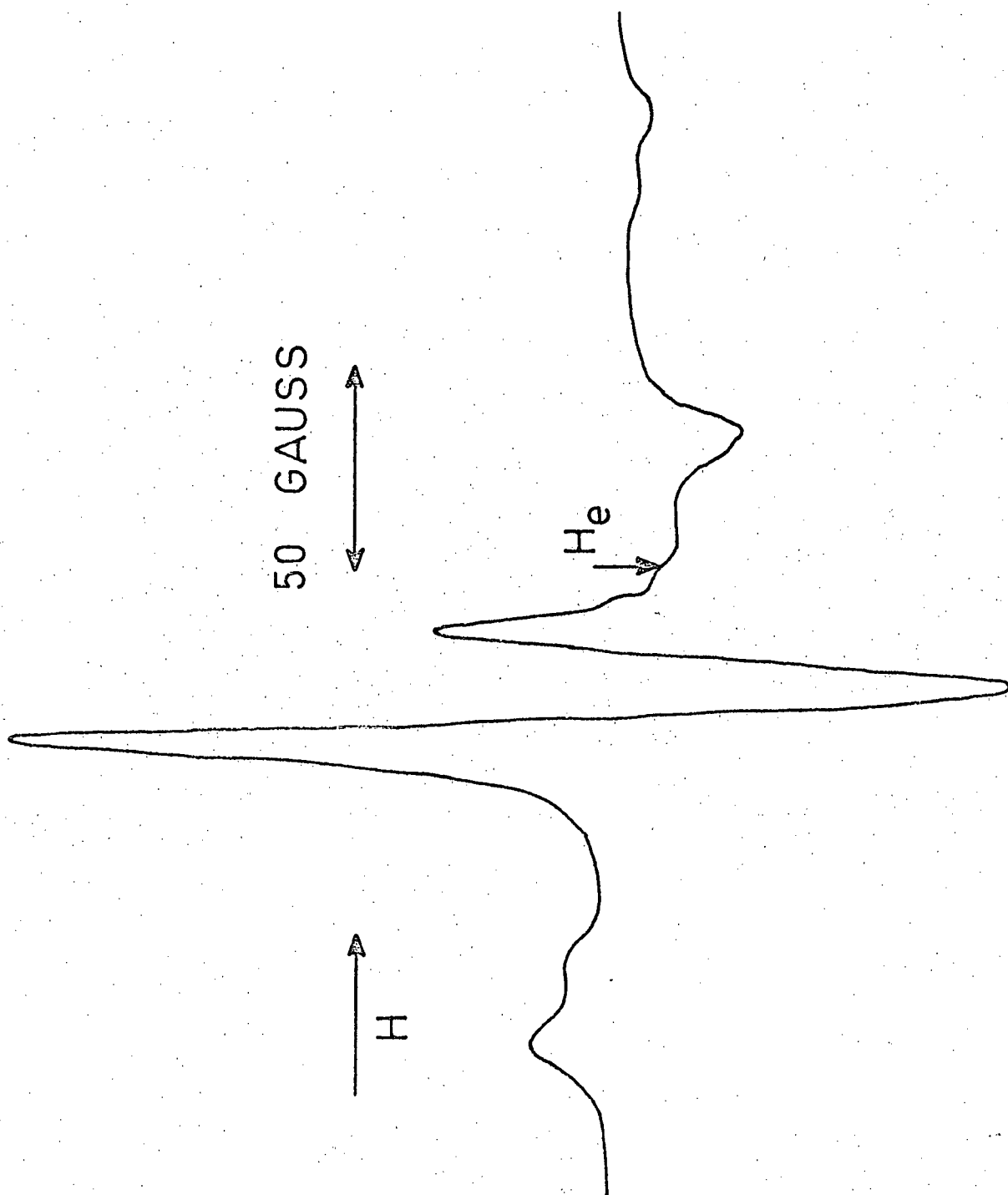


FIGURE 23. EPR spectrum of chlorine dioxide adsorbed on Na-mordenite, recorded at 77° K.

Figure 24 shows a simulated spectrum for ClO_2 adsorbed on Na-mordenite, recorded at 77°K . Figures 25 and 26 show ClO_2 adsorbed on Na-mordenite, recorded at room temperature, observed and simulated, respectively.

8.3 4A and 5A Synthetic Zeolites.

Figure 27 shows a typical spectrum of ClO_2 adsorbed on 4A synthetic zeolite, recorded at 77°K . The linewidth is greatly decreased from that observed on either silica gel or the synthetic mordenites. Consequently, the features in the central portion of the spectrum (corresponding to the y and z components of the hyperfine splitting) are better defined. There is a substantial increase in the magnitude of the components of the hyperfine tensor, and the results are given in Table 1. Figure 28 shows a simulated spectrum corresponding to ClO_2 adsorbed on 4A.

Adsorption on 5A synthetic zeolite again yields a similar spectrum and has not been shown here. The outermost features of the spectrum are somewhat broadened, which possibly suggests the existence of two adsorption sites. This will be discussed later. Spectra recorded at room temperature are markedly changed, although the ClO_2 does not appear to be freely rotating. A partial rotation or some other form of hindered rotation appears evident. The hyperfine and g tensors are given in Table 1.

8.4 13X Synthetic Zeolite.

A typical spectrum of ClO_2 adsorbed on 13X synthetic

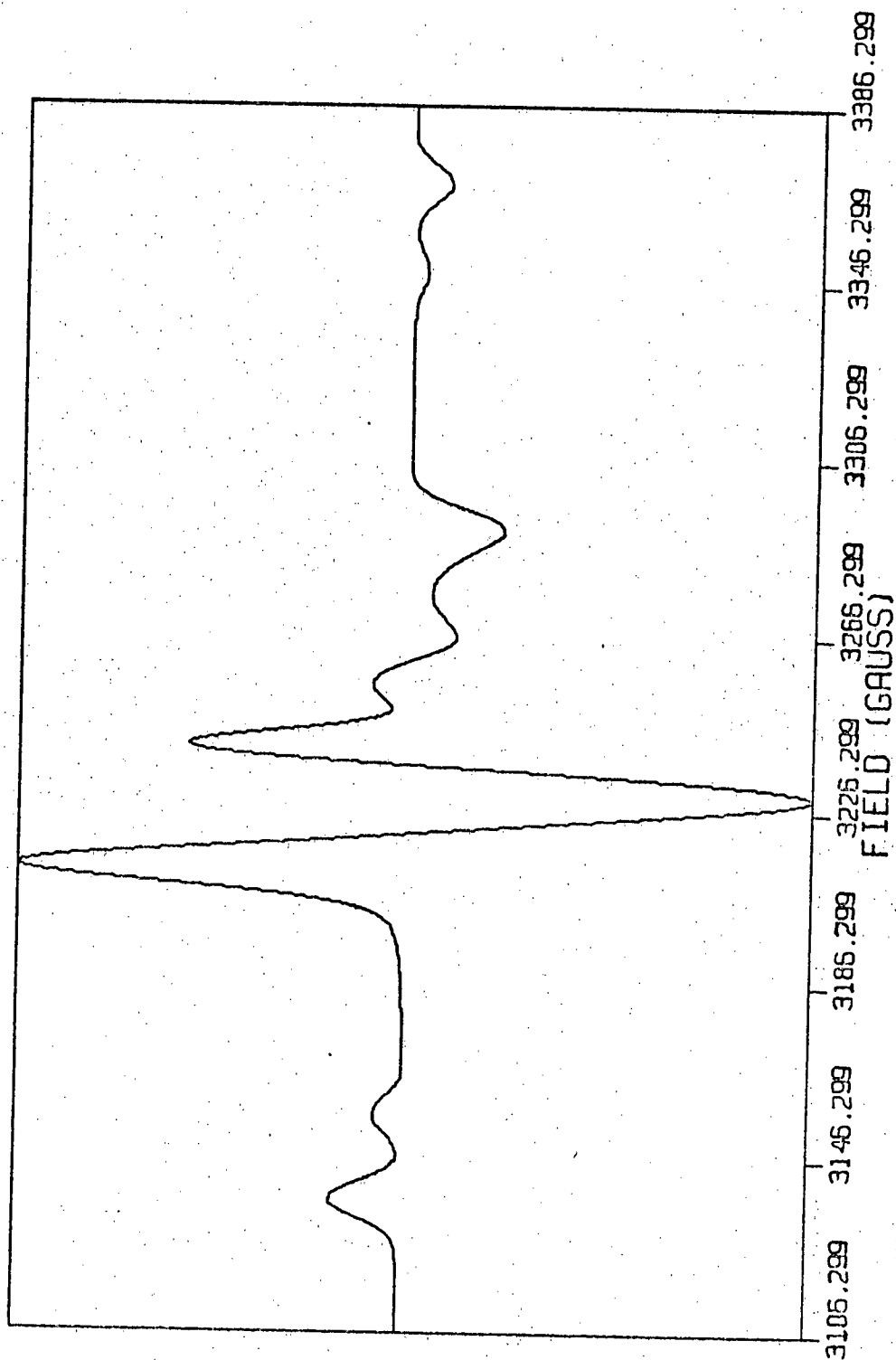


FIGURE 24. Computer simulated EPR spectrum of chlorine dioxide adsorbed on Na-mordenite, recorded at 77° K.

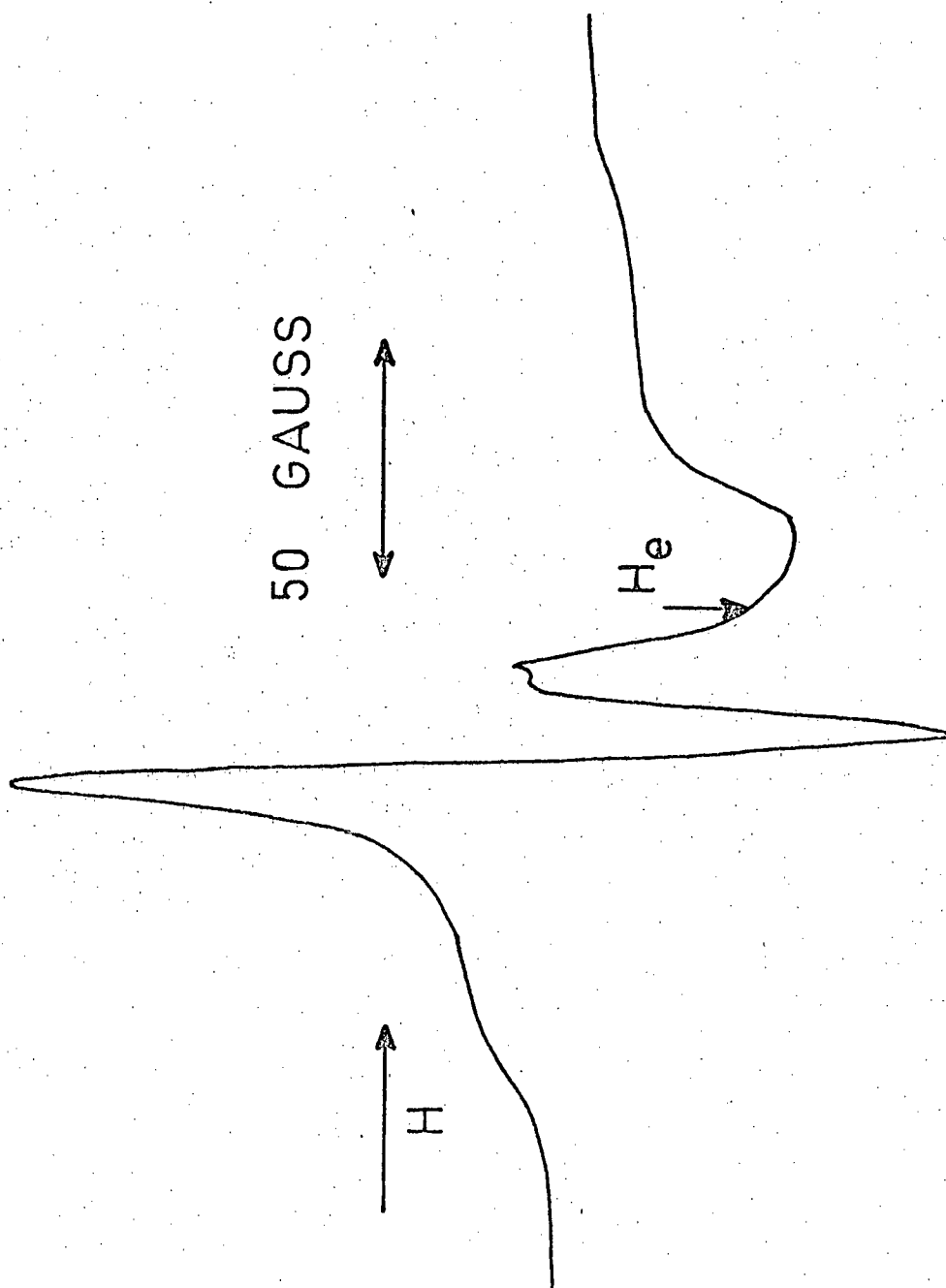


FIGURE 25. EPR spectrum of chlorine dioxide adsorbed on Na-mordenite, recorded at room temperature.

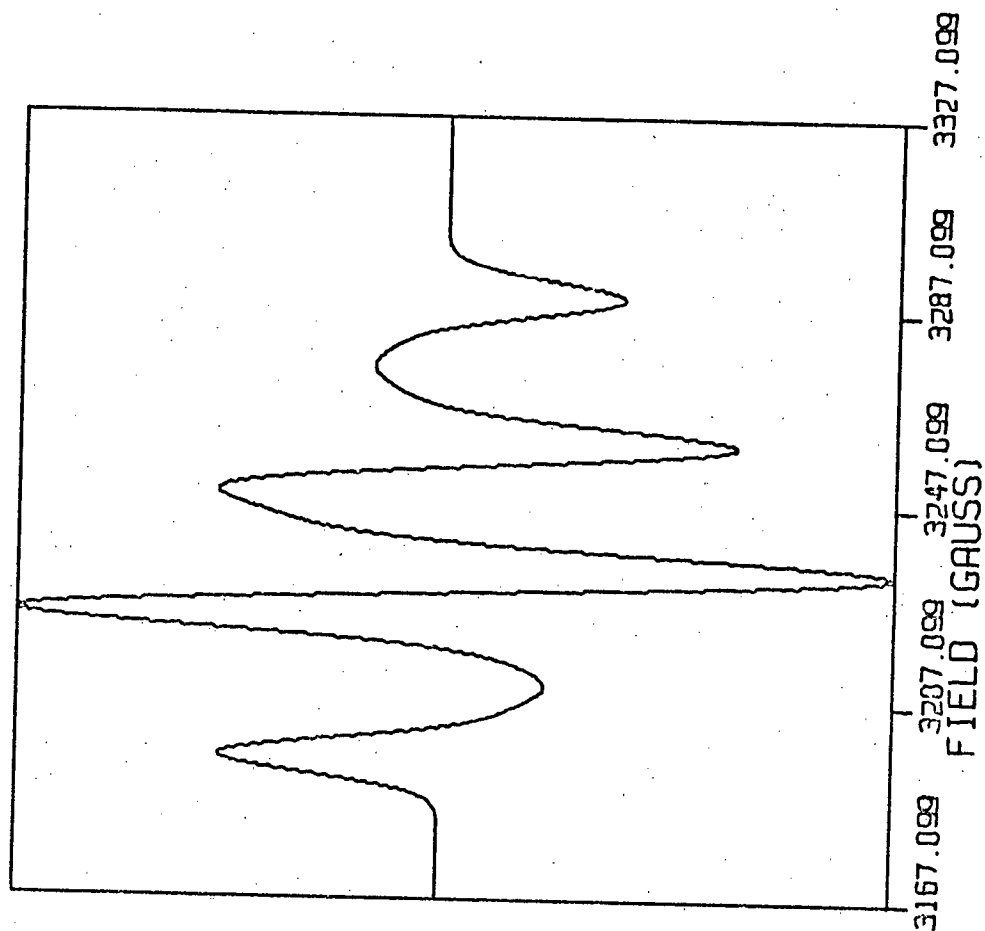


FIGURE 26. Computer simulated EPR spectrum of chlorine dioxide adsorbed on Na-mordenite, recorded at room temperature.

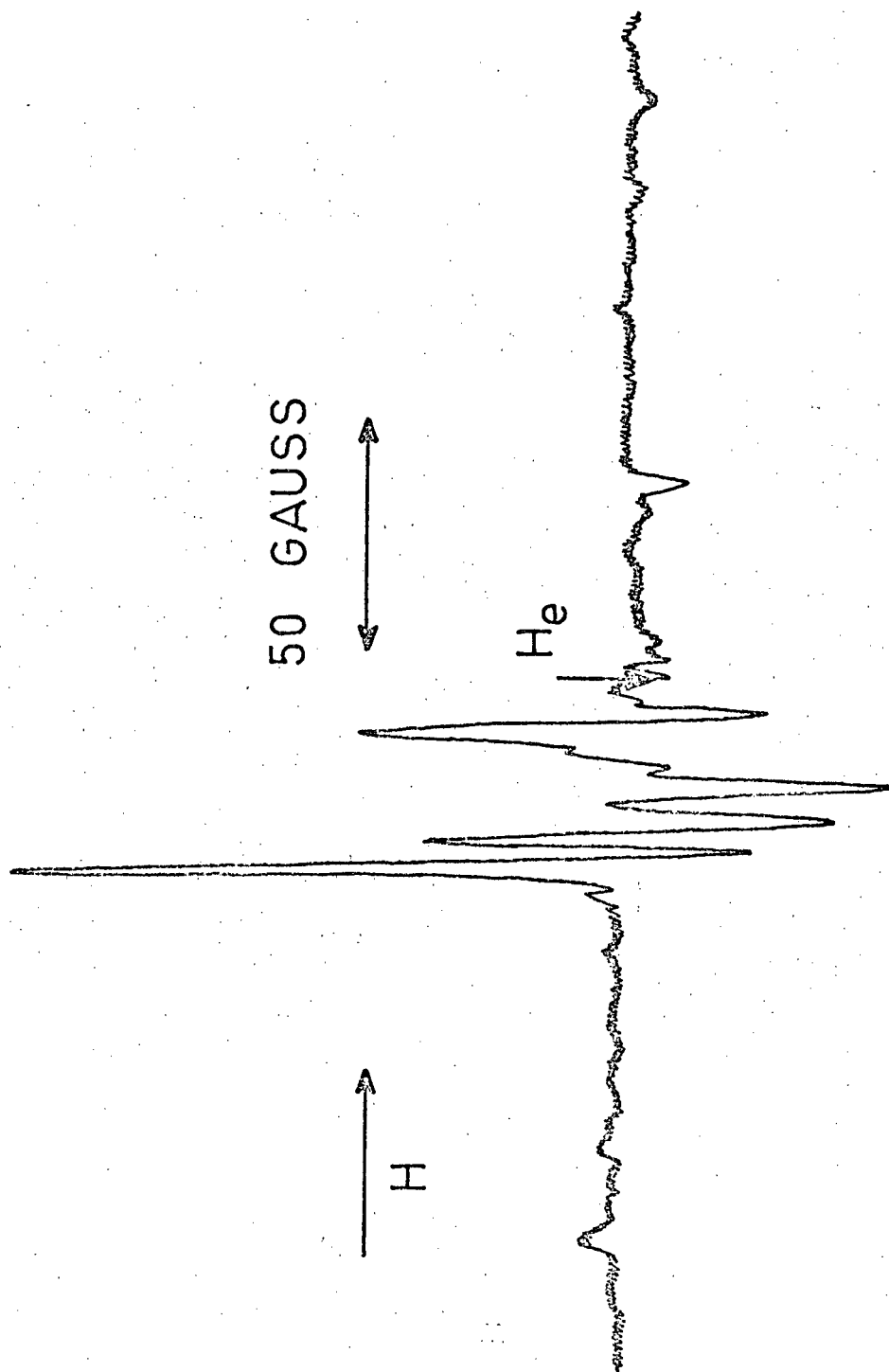


FIGURE 27. EPR spectrum of chlorine dioxide adsorbed on 4A synthetic zeolite, recorded at 77° K.

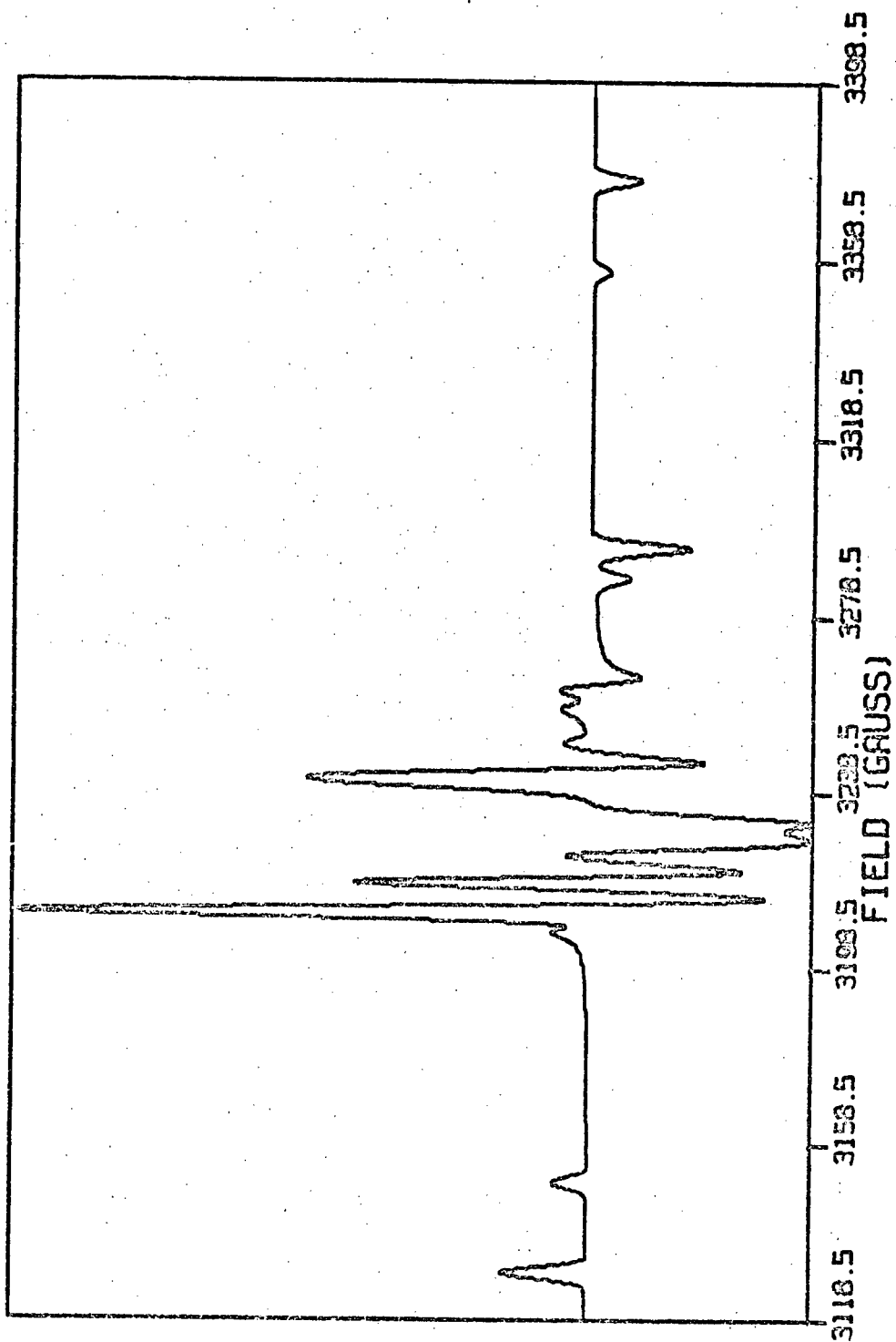


FIGURE 28. Computer simulated EPR spectrum of chlorine dioxide adsorbed on 4A synthetic zeolite, recorded at 77° K.

zeolite is shown in figure 29. The spectrum was recorded at 77°K. A simulated spectrum is shown in figure 30. It is evident from the spectrum that two adsorption sites are present in the zeolite. The outermost components ($m_I = \pm 3/2$, x axis) show this quite clearly. A linewidth difference between the two sites enables them to be more readily distinguished, particularly in the central portion of the spectrum. Table 1 lists the components of the hyperfine and g tensors for the two sites.

Further pumping increases the resolution of the lines although the ClO_2 can be removed from neither site by pumping at room temperature. Variable temperature (annealing type) experiments were performed in the hope that the ClO_2 would be removed preferentially from one of the sites. Unfortunately, line broadening at temperatures higher than 77°K made it impossible for accurate observations to be made. It is apparent that the ClO_2 does not remain rigidly trapped in the zeolite as the temperature is raised, but the exact type of motion could not be determined.

8.5 10X Synthetic Zeolite.

The calcium exchanged form of the 13X zeolite, 10X, was also used as an adsorbent. The spectra recorded at 77°K were similar to those on 13X although the presence of two sites was not as obvious. The reasons for this will be discussed later. The linewidth is broader than that observed on 13X. The spectrum at room temperature was similar to that observed on silica gel, indicating free rotation of ClO_2 in 10X at this temperature. This is unlike the 13X sample,

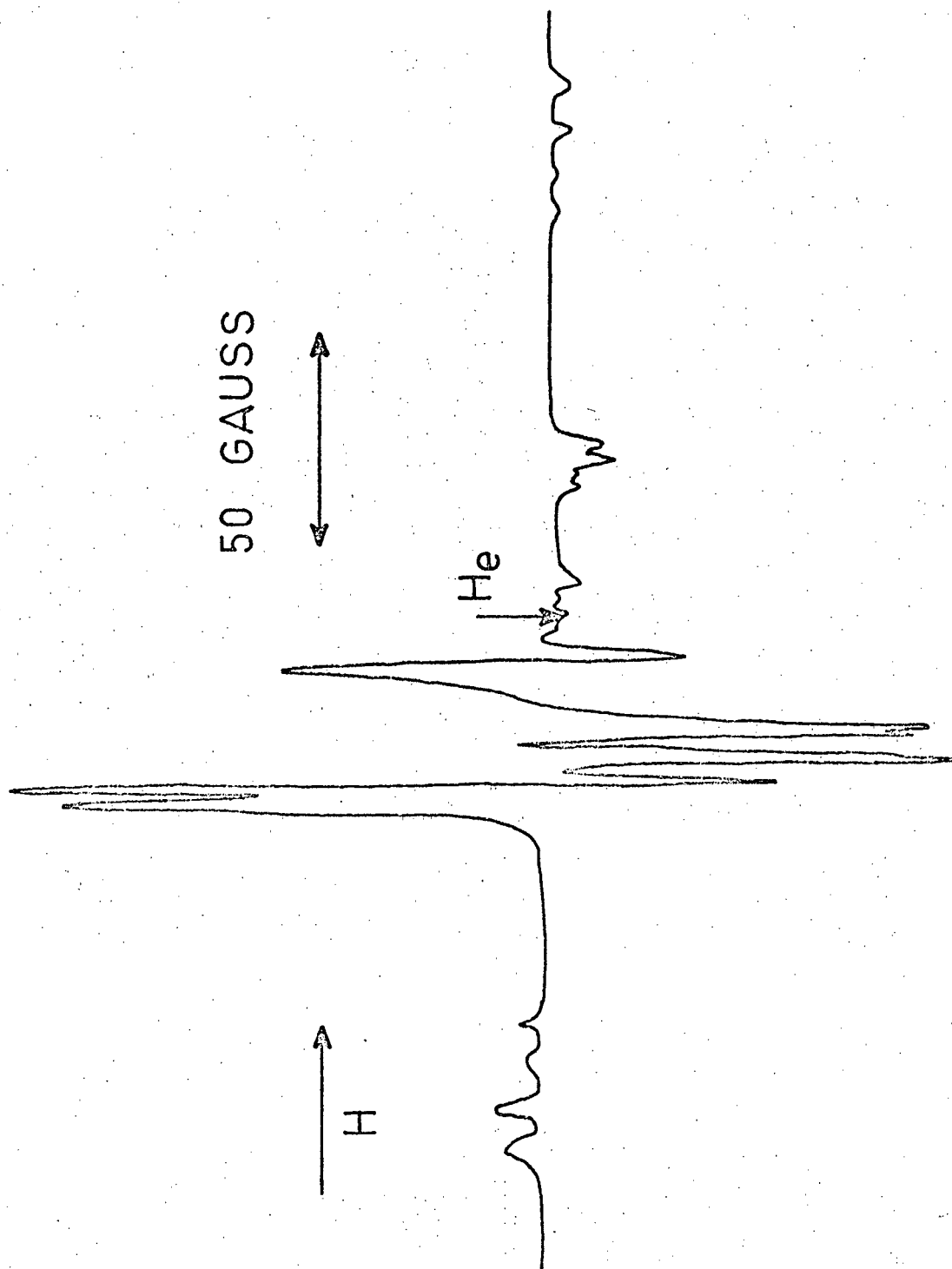


FIGURE 29. EPR spectrum of chlorine dioxide adsorbed on 13X synthetic zeolite, recorded at 77° K.

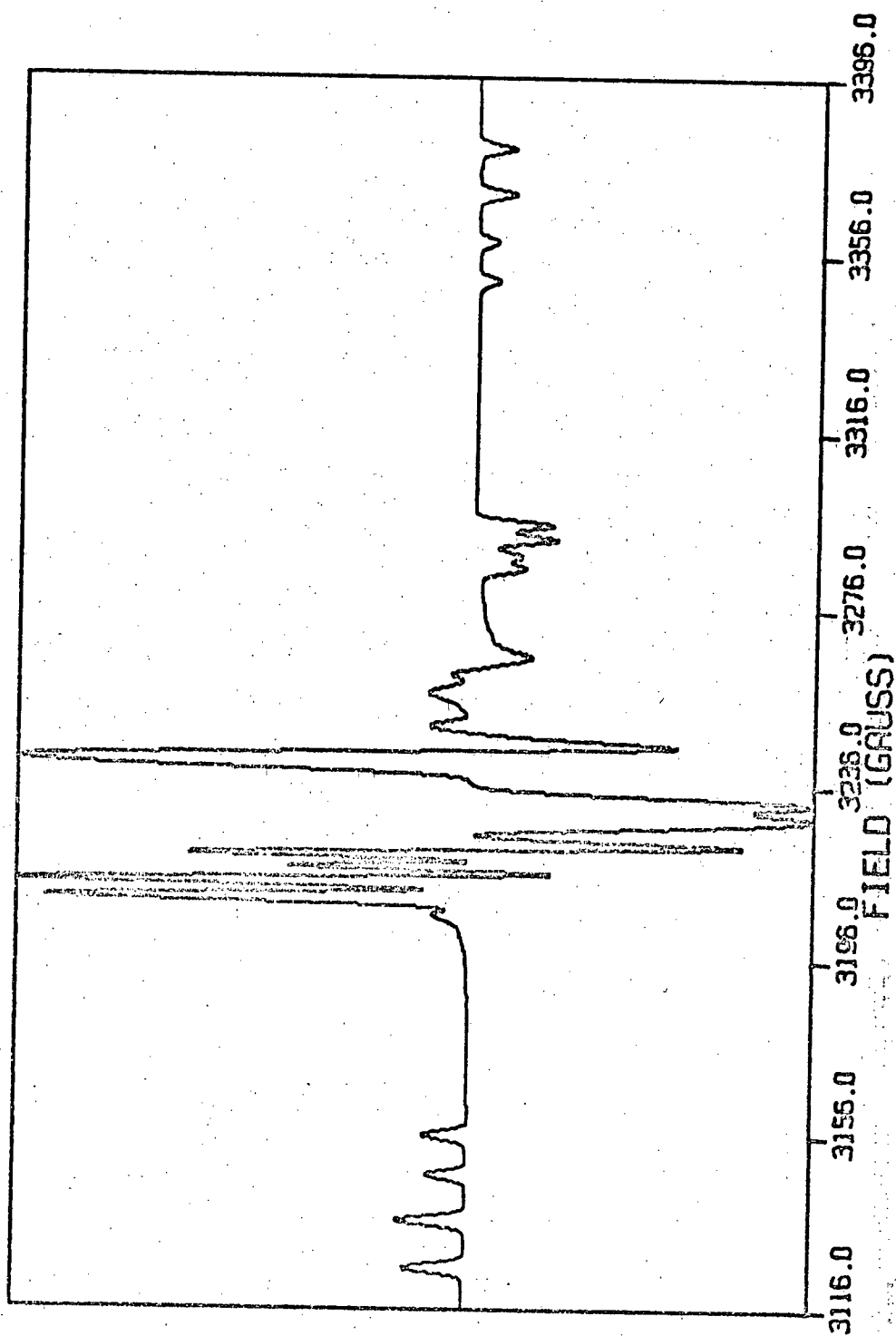


FIGURE 30. Computer simulated EPR spectrum of chlorine dioxide adsorbed on 13X synthetic zeolite, recorded at 77° K.

where the motion of the ClO_2 was still hindered at room temperature.

Table 1 gives the components of the hyperfine and g tensors.

8.6 Lithium Exchanged 13X Synthetic Zeolite.

Lithium was exchanged for the sodium in a sample of 13X and ClO_2 then adsorbed as before. The spectrum recorded at 77°K did not show two distinct sites as did the 13X, and the lines were somewhat broader. Table 1 gives the components of the hyperfine and g tensors.

8.7 Discussion.

ClO_2 is a bent molecule and has the symmetry properties of the C_{2v} point group. Qualitative discussions of the electronic structure of this type of molecule (AB_2) have been given by Mulliken [138] and Walsh [139]. Following the molecular-correlation diagrams given by these authors, the ground state has the configuration

$$\dots (1b_1)^2 (3b_2)^2 (1a_2)^2 (4a_1)^2 (2b_1) , {}^2B_1$$

The b_1 orbital consists of the p_x orbitals of the chlorine and oxygens with possible admixture from the chlorine d_{xz} orbital, and is anti-bonding.

Although an isotropic hyperfine splitting would not be expected from an electron in a b_1 orbital, the odd electron is expected to cause a polarization of the inner s-orbitals on the chlorine and oxygen atoms. This would introduce a small isotropic hyperfine component. An anisotropic hyperfine tensor with the maximum principal value observed when the field is perpendicular to the molecular plane

(along the x-axis) is also expected, of opposite sign to the smaller in-plane principal values, since the unpaired electron is in a b_1 orbital.

The deviations from the free electron value g_e , generally termed g-shifts, may be represented by the general formula (excluding d orbitals)

$$\Delta g_{ii} = \frac{f(c_i c_i', \lambda_{Cl}, \lambda_O)}{E_1 - E_2} \quad (8-1)$$

where $f(c_i c_i', \lambda_{Cl}, \lambda_O)$ is a function of the spin-orbit coupling constants on the atoms chlorine and oxygen (λ_{Cl} and λ_O), and the products of the coefficients of the orbitals on the atoms. The denominator is the energy difference of the two states which are mixing. The various states which are allowed to mix and contribute to the g-tensor may be determined using group theory [182]. For ClO_2 , the dominant g-shift affects g_{yy} and is expected to be large and positive. The shift in the x direction, Δg_{xx} should be close to zero, and negligible if d orbitals are neglected. Δg_{zz} is expected to be positive, and less than Δg_{yy} .

The structural parameters for chlorine dioxide have been obtained by Curl et al [140,141] as a result of a microwave study, and Ward [142] who combined UV spectroscopic data with high resolution IR data. The results are summarized below.

	reference 140, 141	reference 142
r Cl-O (Å)	1.471	1.472
∠ OClO (°)	117.6	117.4

Using the preceding information, the results of chlorine dioxide adsorbed on various surfaces may be analyzed. The results obtained from the present work and those of previous workers are summarized in Table 1.

A general discussion of the adsorption of chlorine dioxide on these surfaces is useful prior to the discussion of the individual cases. Chlorine dioxide has been found to possess a substantial dipole moment, 1.784 D. [143]. This dipole moment, together with the quadrupole moment due to the chlorine nucleus with $I=3/2$, play important roles in the adsorption as detailed previously in Chapter Two. The strong attractive force due to the ionic charges of the adsorbent interacts with these multipole moments and is characterized by the changes observed in the components of the g and hyperfine tensors as compared to these components observed for chlorine dioxide isolated in other media.

It is important in this discussion to analyze these observed parameter changes in terms of adsorption - i.e. the site of adsorption; the position of the chlorine dioxide in relation to the trapping site; any movement of the chlorine dioxide on the surface or at the site.

Buckingham [144] has considered the interaction potential energy u_{12} of two charge distributions 1 and 2 possessing charge q and multipole moments μ, θ, \dots, ϕ . F_z, F_{zz} are the potential and its derivatives at the center of mass of 2 due to the charges of 1.

Hence

$$u_{12} = q_2\phi_2 - \mu_2 F_{2z} - \frac{1}{2} \theta_2 F'_{2zz} - \dots \quad (8-2)$$

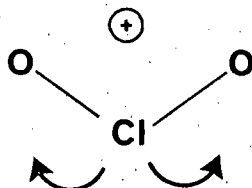
Assuming the adsorption center to be a positive charge as previously discussed for the zeolites, then the favorable relative orientations for a charge-dipole interaction and a charge-quadrupole interaction are as follows:



where + represents a positive charge; → represents a dipole; and ↔ represents a quadrupole. The adsorption in the zeolites expected for ClO_2 according to this model is discussed in the next paragraph.

These same adsorption sites (positive charges) can produce strong electric fields which, in addition to providing additional attractive forces for adsorption, can also determine the relative position of the adsorbed molecule. In the presence of an electric field the dipoles (or induced dipoles if the molecule does not possess a permanent moment) are oriented in the same direction as the field. It has been shown [145] that even for pronouncedly anisotropic dipolar molecules, the mean polarizability in a homogeneous external electric field is practically equal to $(\alpha_1 + \alpha_2 + \alpha_3)/3$ where

α_1, α_2 and α_3 are the molecular polarizabilities in the three axes. We thus expect chlorine dioxide to be adsorbed on the surfaces studied as



The chlorine atom is assumed to be the positive end of the molecule. Assuming substantially strong adsorption, the only probable movement aside from possible slight wagging as indicated by the arrows in the figure, would be a rotation about the z axis of the molecule (bisecting the O-Cl-O bond angle).

Calculations of these electric fields have been performed by Pickert et al [48] and more recently by Dempsey [146] and applied to various zeolites. The calculations were performed by 'growing' the crystal on a computer. The basic quantity of interest is the electrostatic potential at either an ion site j or at a point in free space. Thus

$$\phi_j = \sum_{i,k} q_{i,k} / r_{i,k,j} \quad (8-3)$$

where $q_{i,k}$ is the charge at ion i in the basis at lattice point k, distance $r_{i,k,j}$ from the potential point j. The electrostatic energy of this basis is

$$E = \frac{1}{2} \sum_j q_j \phi_j \quad (8-4)$$

summed over the ions of the basis or some proportion of these, depending on the symmetry. Another quantity of interest is the electrostatic field \vec{F} given by

$$\vec{F} = - \text{grad } \phi \quad (8-5)$$

Evaluation of ϕ at any point in the crystal was done using the transformation method of Ewald [147]. Values of the field \vec{F} and the components of the field gradient tensor were also derived by Dempsey using the Ewald method. Their results will be applied to the EPR spectra of chlorine dioxide adsorbed on the synthetic zeolite 13X and these in turn related to the other adsorbents.

Before discussing the parameters obtained from the spectrum of ClO_2 adsorbed on 13X, it should be pointed out that these parameters were obtained without including the quadrupole interaction term in the spin Hamiltonian. Byberg et al [136] have shown this interaction to be of importance in the ClO_2 molecule trapped in irradiated KClO_4 , in particular giving rise to 'forbidden' transitions of high intensity in certain molecular orientations with respect to the magnetic field. When the off-diagonal tensor elements of \mathcal{H}_Q become comparable to the diagonal parts of \mathcal{H}_{hf} and \mathcal{H}_Q , considerable mixing of nuclear spin states occurs. The selection rule

$$\Delta M_I = 0 \quad (8-6)$$

breaks down and transitions with

$$\Delta M_I = \pm 1, \quad \Delta M_I = \pm 2 \quad (8-7)$$

become observable as well. Several spectra were simulated including the quadrupole interaction but the observed linewidth masked these features. The deviations of the simulated spectra from the experimental spectra, in particular line intensities, are presumed due to this interaction.

Figure 29 clearly shows two distinct adsorption sites on the 13X, the hyperfine splitting constants differing considerably between the two sites. The constants are in fact much larger than those previously observed in other media (see Table 1). The two sites are very likely associated with the surface cations at sites S_{II} and S_{III} , as described in Chapter Three.

The large change in the parameters indicates that the intense electric fields associated with the cations distort the electronic structure of the ClO_2 . Both sites show an increased hyperfine splitting constant indicating an increase in unpaired electron density at the chlorine nucleus. Our model of ClO_2 adsorbed is such that the dipole moment is oriented along the electric field direction, with the oxygen end of the molecule closest to the cation. One would then expect a net shift in electron density towards the oxygen end of the molecule and a decrease in the hyperfine splitting constants. The opposite in fact is the case. The unpaired electron occupies the antibonding b_1 orbital and the unpaired electron density shifts towards the chlorine. This effect arises because it is energetically more favorable for the two electrons in the bonding orbital to be closer to the cation than to have the singly occupied

antibonding orbital close to the cation. Orthogonality conditions ensure that if the bonding orbital shifts towards the cation, the antibonding orbital must shift away from it. The experimental results agree with the proposed model.

The previously mentioned calculations of Dempsey of the electric fields in 13X show the field at S_{III} to be much larger than that at S_{II} . It is reasonable then, to assign the site with the largest shift to S_{III} . The third site, S_I , as outlined in Chapter Three, is inaccessible to adsorbed molecules and therefore is not observed.

Two other zeolites having the same basic X structure as 13X were also used as adsorbents. 10X is a calcium zeolite whereas the 13X is of course sodium. It is expected that only one site should be observed for a 100 percent exchanged form since two sodium cations are replaced by a single doubly-charged calcium, thus leaving site S_{III} unoccupied. In fact, the manufacturers state that the zeolite is only 75 percent exchanged, leaving the possibility of sodium cations in sites S_{II} and S_{III} available for adsorption, as the cations in these sites are exchanged after those in S_I . The spectrum of ClO_2 on 10X is consequently less resolved than the 13X but only one site appears to be present.

A lithium exchanged X structure zeolite is expected to show two distinct sites similar to 13X, with increased shifts in the hyperfine splitting constants due to the smaller size of the lithium cation. Only one distinct site was observed although indications of a second site, much less populated, were evident. It is reasonable to assume that the S_{III} site contains adsorbed water retained from the

exchange process and so is unavailable for adsorption of ClO_2 .

The observed site is then associated with S_{II} , and approximates that of S_{II} in 13X. An increased electric field intensity is postulated for the lithium zeolite due to the increased charge/size ratio. The decreased size of the cation, however, decreases the extent of exposure of the cation to the cavities providing less contact with the ClO_2 molecules even though the specific electric field intensity at the cation surface is stronger.

The spectrum observed on silica gel, although less resolved than on the zeolites, is helpful in analyzing the parameters obtained. The isotropic splitting constant obtained from the room temperature spectrum is 17.1 gauss. This is in good agreement with those obtained from the other studies mentioned and is to be expected, since this should vary little from medium to medium. The isotropic splitting constant obtained from the anisotropic spectrum (i.e. $T_{xx} = A_o + B_{xx}$; the observed splitting, T_{xx} is composed of both isotropic $[A_o]$ and anisotropic $[B_{xx}]$ parts) agrees with that observed. This offers additional support to the assigned values of the parameters.

Some mention should be made of the rather large value assigned to the hyperfine component along the y-axis of the molecule (across the oxygens in the plane of the molecule). It seems reasonable to expect some change in this component from the 'free state' value due to the manner in which the ClO_2 is adsorbed. A decrease in the O-Cl-O bond angle is probable, possibly accounting for this observed change. Agreement of the calculated isotropic value to

that observed lends support to this view.

The parameters obtained from the spectra observed on the zeolites 4A and 5A are in agreement with the arguments proposed for the other zeolites. The electric fields produced by the cations are less intense than those in 13X as indicated by the parameters. The cation sites are less well defined as compared to 13X and only one site appears evident.

Chlorine dioxide adsorbed on the mordenite samples indicate also a much less intense electric field at the adsorption sites. The spectrum recorded at room temperature indicates some motion of the ClO_2 , although somewhat more restricted than that observed on silica gel. Rotation about the z-axis of the ClO_2 molecule seems most probable, but a spectrum simulated for this case does not agree with the observed spectrum and a restricted rotation is assumed. Accurate measurements of the hyperfine and g tensor components was not possible due to the large observed linewidth.

The measured components of the g tensor were in agreement with those predicted for a molecule such as ClO_2 : g_{xx} is close to the free-spin value, as is generally found for an electron in a b_1 orbital composed of p_x -atomic orbitals. Comparing this to the SeO_2^- radical [148] where a negative Δg_{xx} is associated with admixture of the selenium d_{xz} level into the b_1 orbital, it is reasonable to assume little participation of the 3d chlorine orbital in ClO_2 . The values for Δg_{yy} and Δg_{zz} are also in agreement with theory, Δg_{yy} having a large positive value with $\Delta g_{xx} < \Delta g_{zz} < \Delta g_{yy}$.

CHAPTER NINE

NITROGEN DIOXIDE, NO₂

Nitrogen dioxide, like ClO₂, is a stable paramagnetic molecule whose normal chemical state is a gas. The EPR technique has frequently been used to study this molecule in the gaseous and liquid phases [149,150]. One of the purposes of the present study was to compare the spectrum of the adsorbed molecule to the well-established spectra of NO₂ in a variety of environments. Particular attention will be given to comparison of spectra on other adsorbents and in various matrices.

The reported spectra of NO₂ in various polycrystalline media generally show linewidths of the order of 10-20 gauss, limiting the amount of detail which can be resolved [151,152]. More recent studies of NO₂ in N₂O₄ have produced spectra with much smaller

linewidths, revealing greater detail [150, 153]. EPR spectra of NO_2 adsorbed on zinc oxide [154, 155] and on magnesium oxide [156] are also not well resolved. Comparison of these spectra to those of this study will be made in the discussion.

9.1 Silica Gel.

The spectrum recorded at 77°K for NO_2 adsorbed on silica gel is shown in figure 31. The expected pattern of three groups of lines due to the interaction of the odd electron with the ^{14}N nucleus, which has a nuclear spin $I=1$, was observed. The complexity of the spectrum arises from the fact that both the g and hyperfine tensors are anisotropic. The spectrum is complicated further by broadening of those lines associated with transitions involving $m_I = \pm 1$ compared to those with $m_I = 0$, together with an overlapping of some lines. The observed line width also overshadows some features. Table 2 gives the g and hyperfine tensor components derived from the computer simulation of the spectrum. Figure 32 shows the computer fitted spectrum. The spectrum observed on silica gel is comparable in resolution to those obtained on other adsorbents as yet reported in the literature.

When the temperature was raised from 77°K a broadening of the spectrum occurred. Specific changes in the spectrum occur if the adsorbed NO_2 begins to rotate about a given axis on warming. The linewidth of the spectrum even at 77°K makes it difficult to distinguish axially symmetric tensors from completely anisotropic ones.

TABLE 2

Reference	Hyperfine components (gauss)				g-value			
	T _{xx}	T _{yy}	T _{zz}	A _O	g _{xx}	g _{yy}	g _{zz}	medium
154	52	47	65	54.6	2.007	1.994	2.003	adsorbed on ZnO @ 77°K
156	53.0	49.0	66.4	56.5	2.005	1.9915	2.002	adsorbed on MgO @ 77°K
156	50.0	47.9	66.4	54.8	2.0058	1.9920	2.0018	solid N ₂ O ₄ @ 77°K
153	50.3	48.2	67.3	55.25	2.0061	1.9922	2.0022	solid N ₂ O ₄ @ 77°K
150	50.2	49.6	68.3	56.0	2.0065	1.9960	2.0029	solid N ₂ O ₄ @ 77°K
(±0.2) gauss					(±0.0005)			
this work	52.3	48.7	67.8	56.3	2.0051	1.9926	2.0019	adsorbed on silica gel @ 77°K
this work	53.1	51.0	65.5	56.5	2.0066	1.9956	2.0029	adsorbed on 13X @ 77°K
this work	50.1	48.1	66.7	55.1	2.0062	1.9926	2.0025	adsorbed on H-mordenite @ 77°K
¹⁵ NO ₂								
this work	71.1	67.7	93.8	77.5	2.0062	1.9926	2.0025	adsorbed on H-mordenite @ 77°K

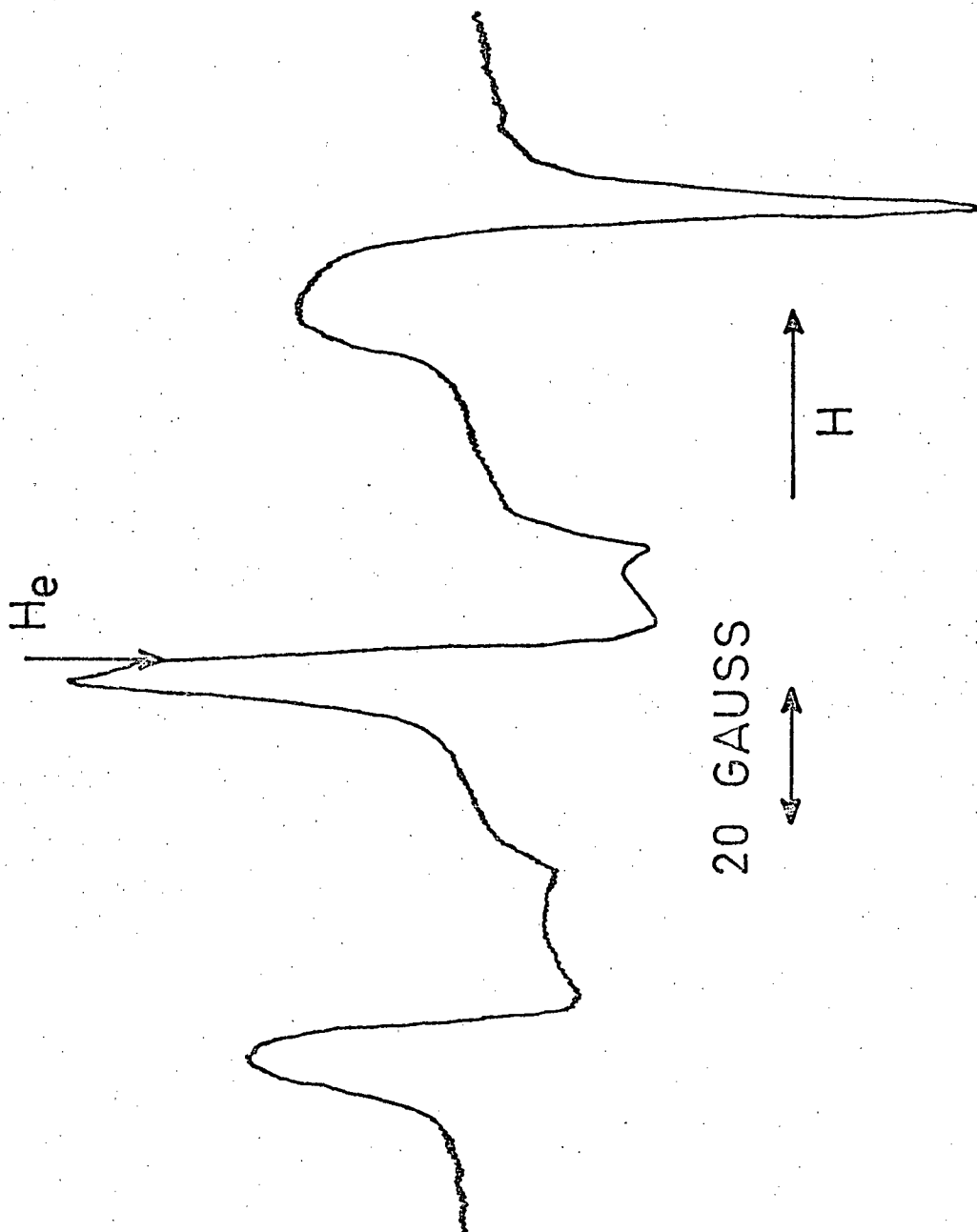


FIGURE 31. EPR spectrum of nitrogen dioxide adsorbed on silica gel, recorded at 77° K.

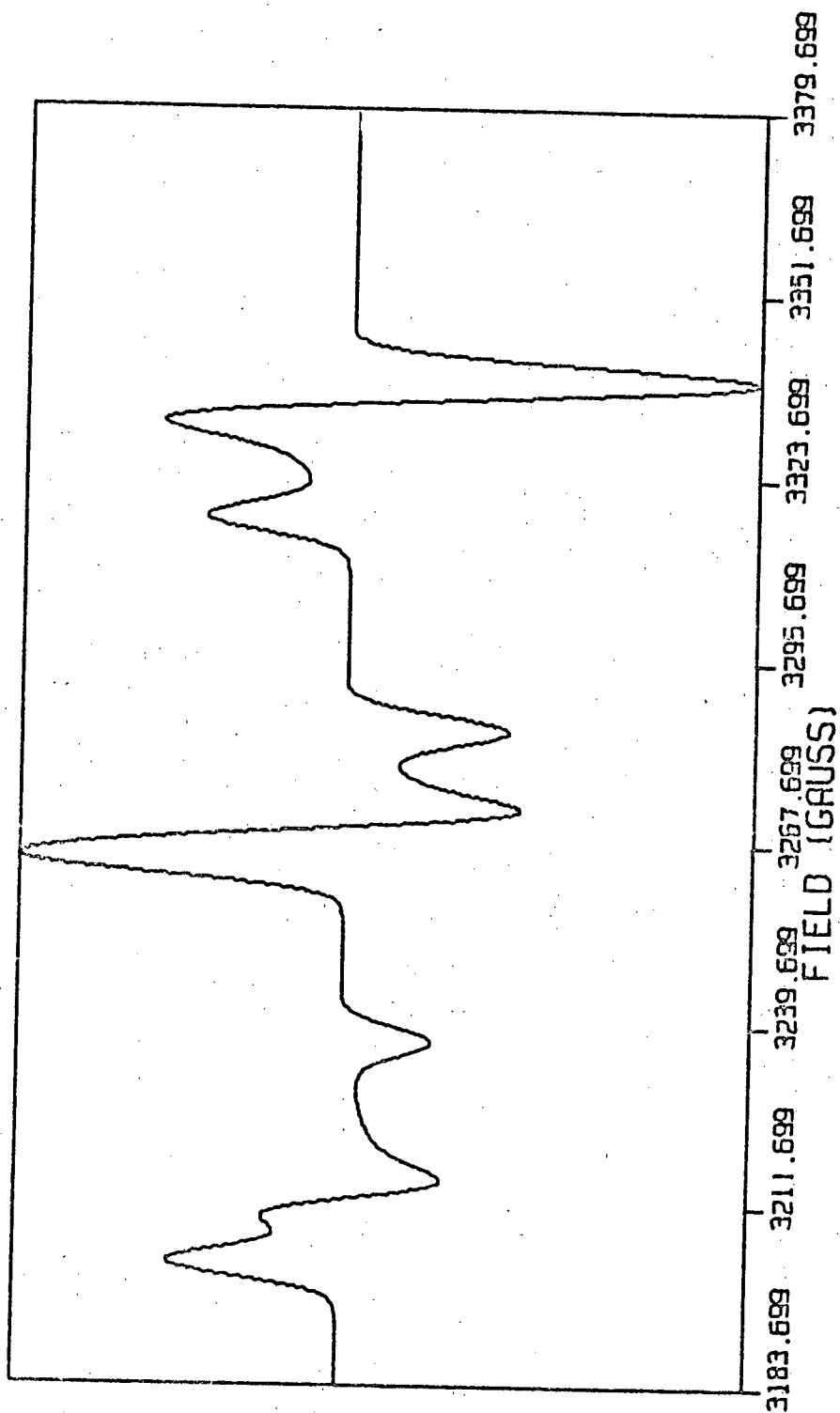


FIGURE 32. Computer simulated EPR spectrum of nitrogen dioxide adsorbed on silica gel, recorded at 77° K.

The increased broadening due to the increase in temperature makes it impossible in this case. At approximately 200°K, the NO₂ appears to be freely rotating on the silica gel, since the structure on the three groups of lines is completely broadened. Above this temperature, the spectrum could not be discerned from the background. When the sample was re-cooled, the signal was recovered unchanged.

9.2 13X Synthetic Zeolite.

The spectrum at 77°K of NO₂ adsorbed on 13X synthetic zeolite is similar to that observed on silica gel. The parameters derived from the spectrum are given in Table 2. Line broadening is somewhat more evident in this case. Differentiation between axially symmetric and fully anisotropic tensors is very difficult. Figure 33 shows a typical spectrum while figures 34 and 35 show computer simulated spectra for fully anisotropic and axially symmetric tensors respectively.

A comparison of figures 34 and 35 shows the similarity of the two spectra and the difficulty that might be encountered in analyzing spectra with the linewidths generally found. The spectrum corresponding to axially symmetric tensors could be caused by rotation of the NO₂ about the z-axis. No spectrum was observed at room temperature.

9.3 H-Mordenite.

Figure 36 shows a typical spectrum of NO₂ adsorbed

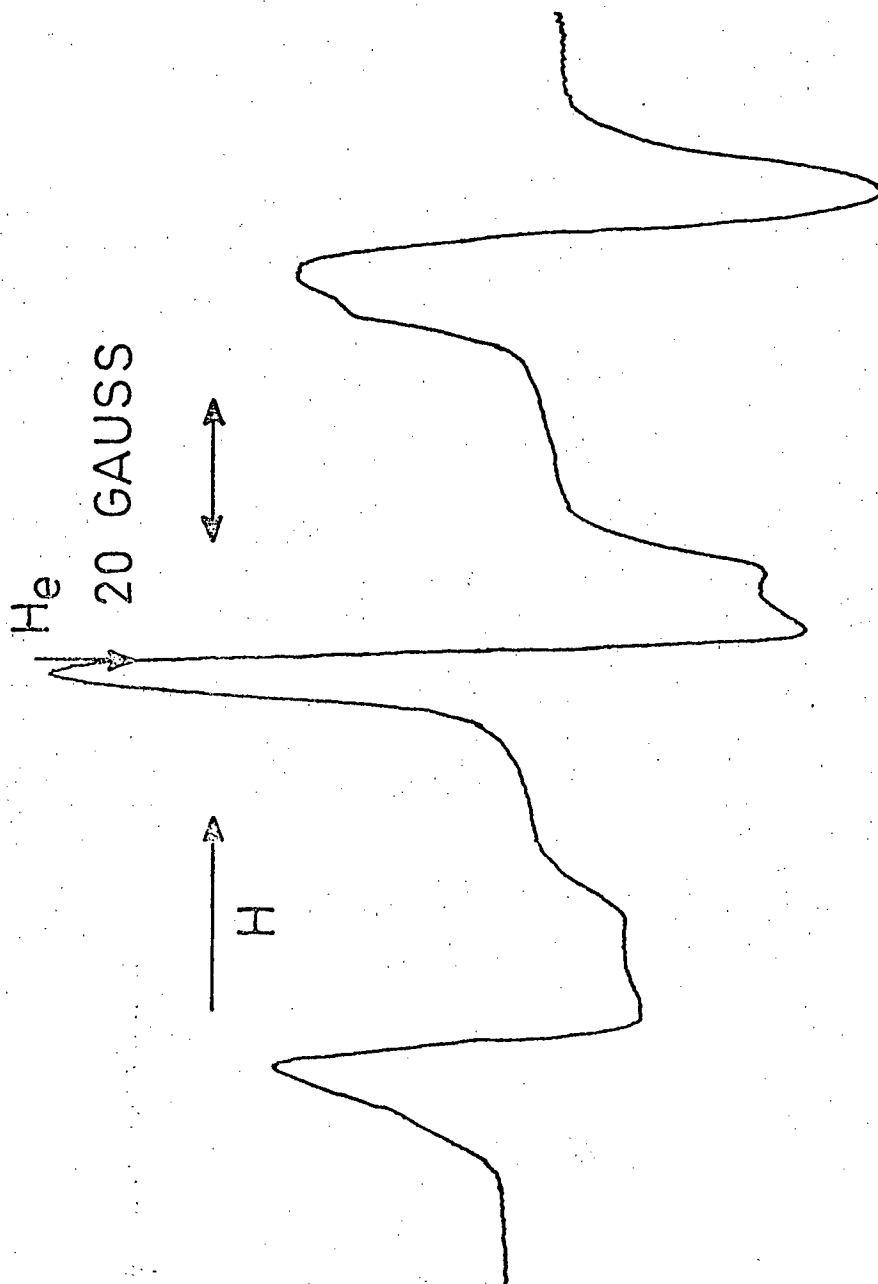


FIGURE 33. EPR spectrum of nitrogen dioxide adsorbed on 13X synthetic zeolite, recorded at 77° K.

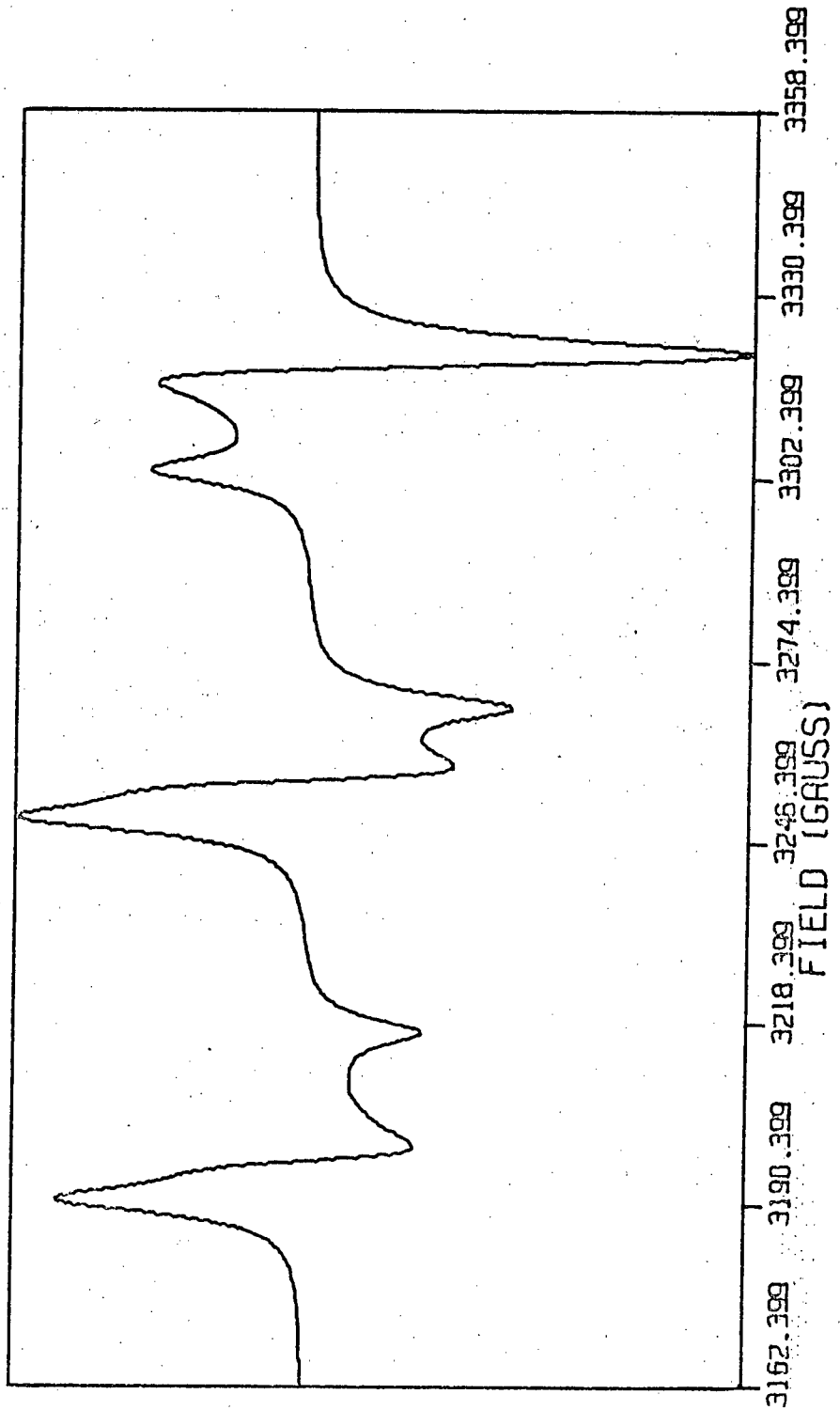


FIGURE 34. Computer simulated EPR spectrum of nitrogen dioxide adsorbed on 13X synthetic zeolite, recorded at 77° K.

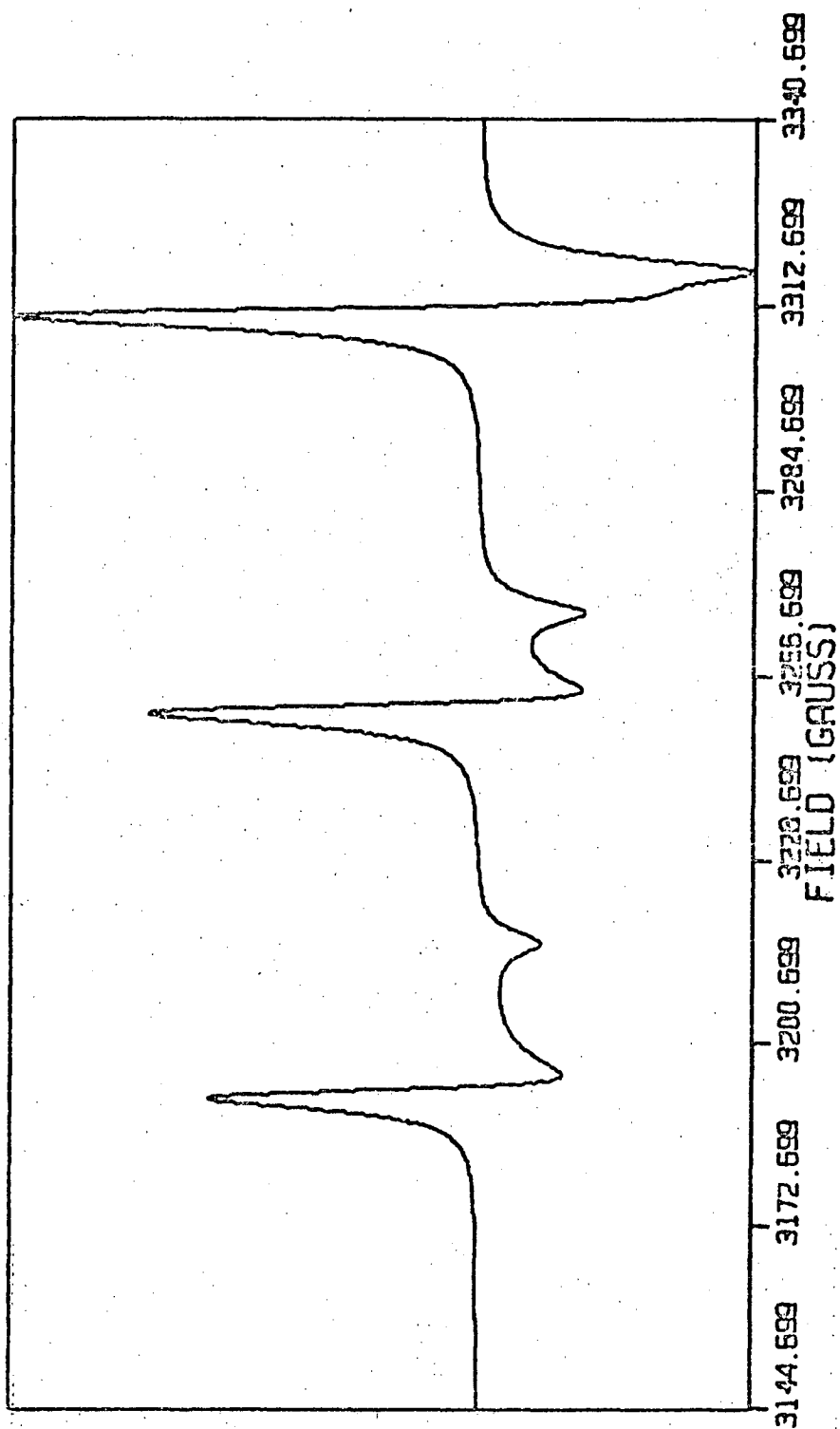


FIGURE 35. Computer simulated EPR spectrum (assuming axially symmetric g and hyperfine tensors) of nitrogen dioxide adsorbed on 13X synthetic zeolite, recorded at 77° K.

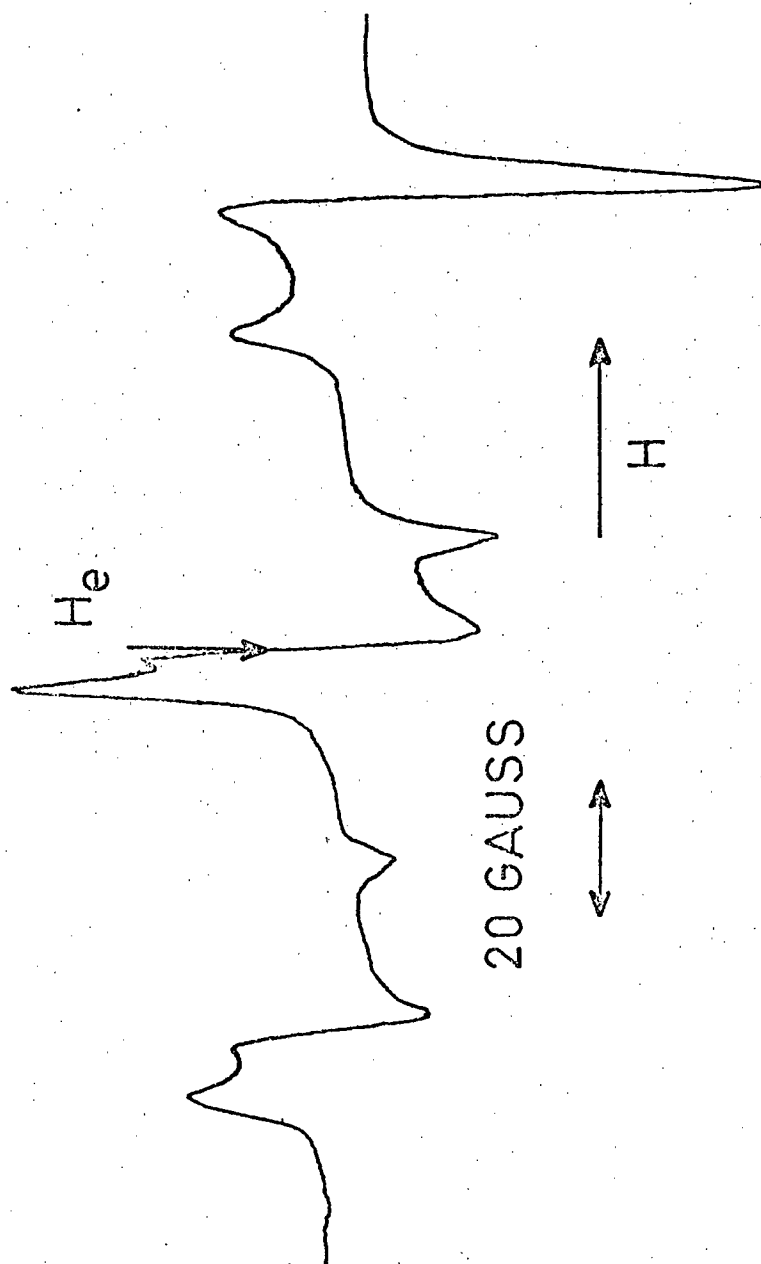


FIGURE 36. EPR spectrum of nitrogen dioxide adsorbed on H-mordenite, recorded at 77° K.

on H-mordenite, recorded at 77°K. It should be noted that much higher pressures of NO₂ were needed to observe spectra than those required for ClO₂. Probable reasons for this phenomenon will be given in the discussion. An obvious feature of the spectrum is the reduced linewidth as compared to NO₂ adsorbed on other surfaces yielding a well resolved anisotropic set of triplets. The resolution compares to that observed for NO₂ trapped in a N₂O₄ matrix at 77°K as reported by Schaafsma et al [153] and James et al [150]. A computer simulated spectrum is shown in figure 37 and the results are given in Table 2. The consequences of the narrow linewidth will also be discussed later.

The spectrum for ¹⁵NO₂ adsorbed on H-mordenite is shown in figure 38, and a simulated spectrum in figure 39. The parameters obtained are given in Table 2 and agree with those expected for ¹⁵N with I = ½.

An attempt was made to record spectra at higher temperatures with a view to obtain information on possible motional processes of the NO₂ since the narrow linewidth at 77°K should enable any new features to be easily seen. Unfortunately, this was not the case and line broadening at higher temperatures obscured all details.

9.4 Discussion.

NO₂, like ClO₂ is also a bent molecule with the symmetry properties of the C_{2v} point group. Following the approach of

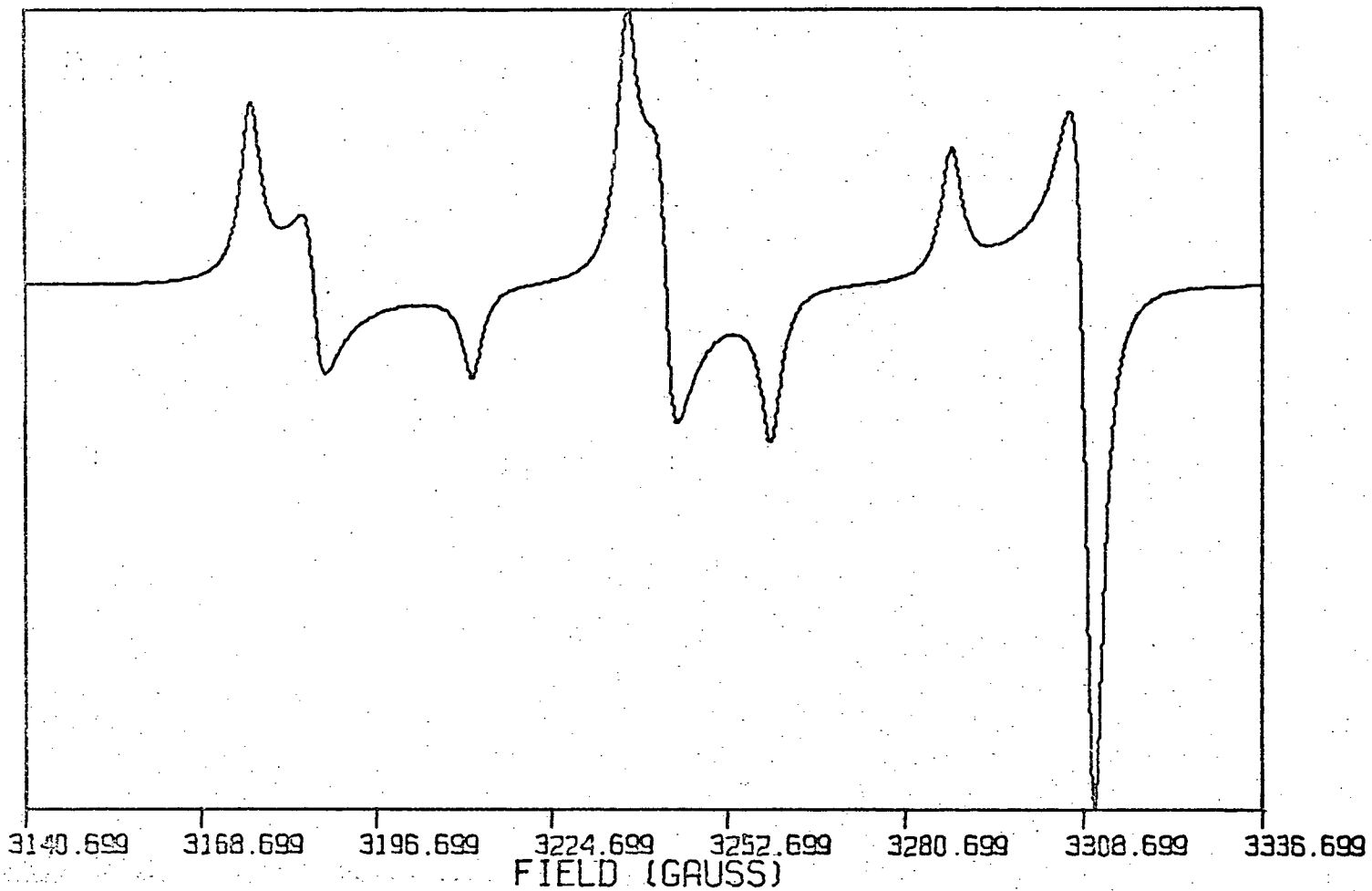


FIGURE 37. Computer simulated EPR spectrum of nitrogen dioxide adsorbed on Il-mordenite, recorded at 77° K.

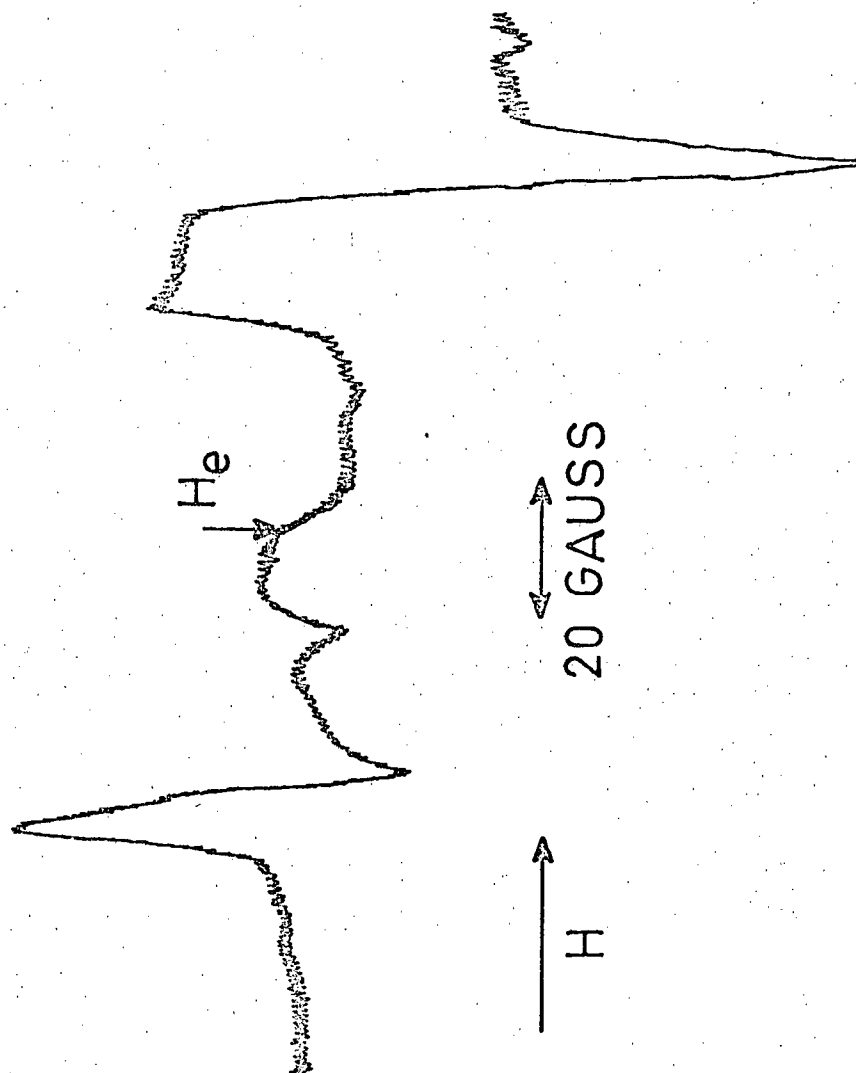


FIGURE 38. EPR spectrum of ^{15}N nitrogen dioxide adsorbed on H-mordenite, recorded at 77°K .

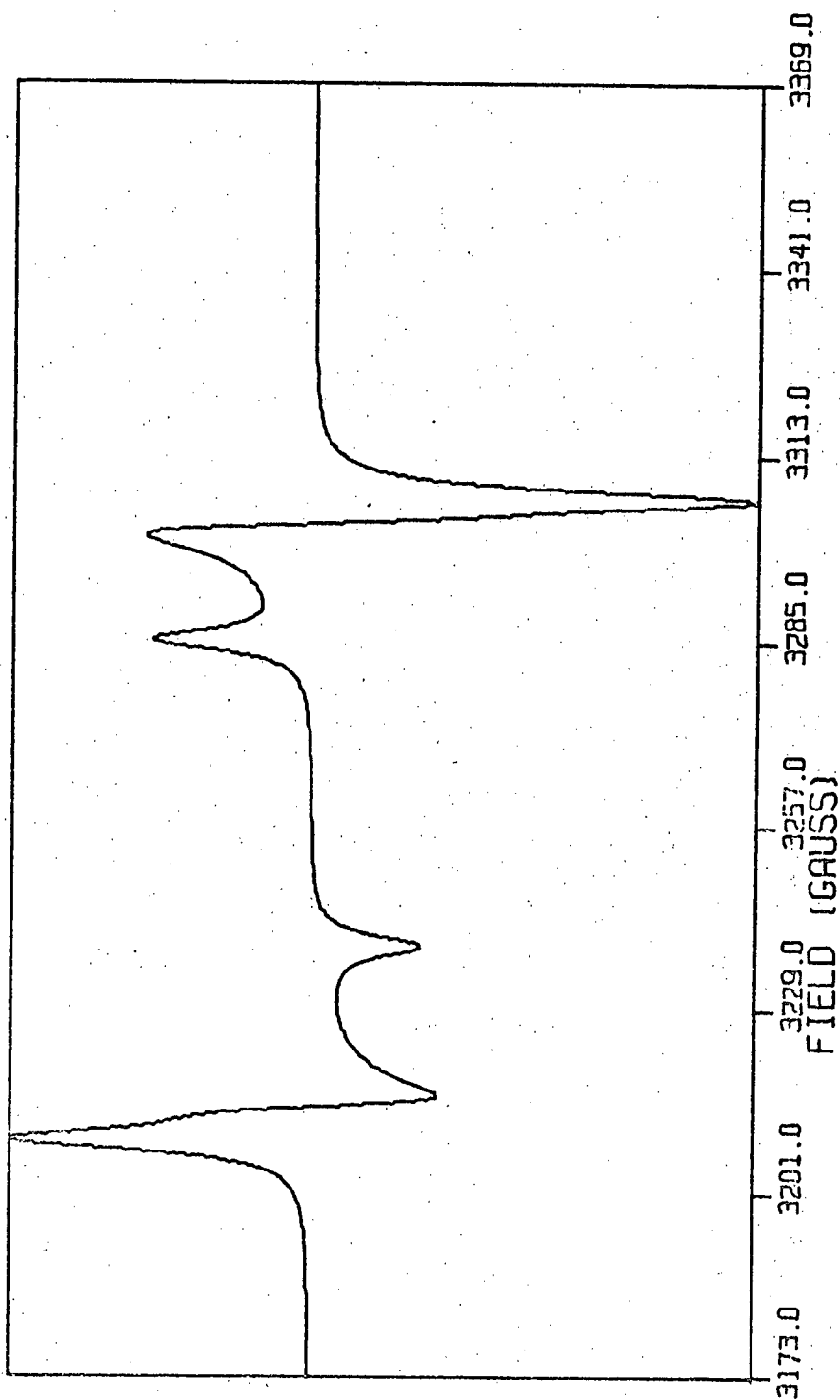
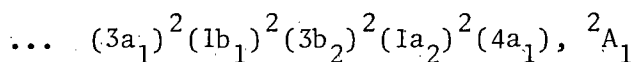
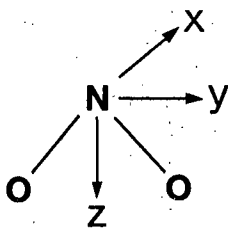


FIGURE 39. Computer simulated EPR spectrum of ^{15}N nitrogen dioxide adsorbed on H-mordenite, recorded at 77°K .

Walsh [139], the ground state has the configuration



The unpaired electron occupies an a_1 orbital, delocalized and constructed from both s and p orbitals on the central nitrogen atom. The hyperfine spectra should thus display a considerable isotropic splitting and the anisotropy should be such that its maximum value occurs when the C_2 axis of the molecule is aligned along the magnetic field. The assignment of the molecular axes is shown below



where the x-axis is perpendicular to the plane of the molecule.

The dominant g-shift, as with ClO₂, is expected to be along the y-axis although in this case it will be negative. These g-shifts are determined from the general formula given by equation (8-1). The g-value along the direction of the maximum value of the hyperfine tensor should be close to the free spin value or slightly greater. The shift along z, Δg_{zz} will also be small and positive.

Table 2 includes the results of NO_2 observed in various matrices and adsorbed on surfaces other than those studied here. The results of this work are also included. Comparison of the spectrum of adsorbed NO_2 with the well-established spectra in a variety of environments is the subject of the following discussion.

The dipole moment of NO_2 is considerably less than that of ClO_2 , being .29 D [157,158], and on this basis alone, one would expect somewhat weaker adsorption in comparable situations. The nitrogen nucleus has a nuclear spin $I = 1$ and so a quadrupole moment can also affect the absorption spectrum. The weaker adsorption forces are substantiated by the loss of spectrum on warming the sample to room temperature. This is in contrast to the results of Colburn et al [159] who observed the spectrum of rapidly tumbling NO_2 molecules at room temperature in 13X zeolites. The pressures of NO_2 in equilibrium with the zeolites were, however, several orders of magnitude larger than those in the present experiments. The pressures needed to observe the NO_2 spectra were however, much higher than those needed for ClO_2 indicating a much reduced adsorption attraction.

The expected orientation of NO_2 on adsorption differs from that of ClO_2 since the dipole moment is aligned in the opposite direction. One would expect, then, that the nitrogen nucleus will be closest to the adsorption sites. Rotation about the molecular z-axis would seem more probable, then, in this case than with ClO_2 .

The results observed from the adsorption on silica gel are quite similar to those reported for the adsorption of NO_2 on MgO [156]. The isotropic hyperfine splitting of 56.3 gauss is in good agreement with, and varies little from, that observed on other surfaces. In fact, the isotropic portion of the hyperfine tensor changes little between the surfaces studied and NO_2 molecules trapped in other media. The fields inherent in these different environments vary from very weak in the inert gas matrices to very strong in the synthetic zeolites. This implies that the s-character of the molecular orbital of the nitrogen is not appreciably affected by the surroundings of the molecule. Small changes, however, are observed for the anisotropic components, but are smaller than the linewidth used for the simulations. The assignment of g values agrees with that expected for this molecule: g_{xx} is greater than the free spin value g_e ; g_{yy} is less than g_e ; and g_{zz} very nearly equals g_e . This is in accordance with the work on the isoelectronic molecule CO_2^- [160].

The observed spectrum of NO_2 adsorbed on the zeolite 13X is not as striking as that for ClO_2 for several reasons. Direct evidence for two distinct adsorption sites is not immediately obvious. The lineshape is somewhat different from that observed on the other surfaces and the spectrum is best simulated using a Lorentzian rather than a Gaussian lineshape function. The g values are similar to those observed on other surfaces and the deviations in the anisotropic components of the hyperfine tensor are

less than the linewidth. The only noticeable effect of adsorption is the different lineshape. The strong electric fields in the cavities of the zeolite do not have the pronounced effects observed in the case of ClO_2 . This is surprising in that the approach of the nitrogen nucleus is much closer to the origin of the fields than was the chlorine nucleus, due of course to the proposed mode of adsorption.

NO_2 adsorbed on H-mordenite yielded a spectrum which enabled a more precise assignment of parameters. The hyperfine components are clearly seen and the g tensor readily measured. The assignment is very close to that of Schaafsma et al [153], of the components of both the g and hyperfine tensors. The adsorption sites in H-mordenite are thought to be in the side pockets lining the main cylindrical tubes of the structure (see Figure 11). Each pocket has space sufficient for only one molecule reducing broadening due to recombination of the radical to form N_2O_4 and also dipolar broadening caused by other NO_2 molecules.

In the experiments of Schaafsma et al, solid N_2O_4 was chosen as the host matrix due to its inertness towards NO_2 and the absence of any internal electric fields, being a molecular rather than an ionic matrix. Distortion of the NO_2 due to spatial effects should also be minimized since the structure of the guest and host molecules are the same. In light of the similarity of the parameters obtained from the spectrum of NO_2 adsorbed on H-mordenite to those in solid N_2O_4 , it appears adsorption, in this case,

has little or no effect on the NO_2 . It is likely, then, that the 'trapping pockets' of H-mordenite serve only as isolation cages for the NO_2 molecules and have little effect on its electronic structure. This is in accord with the parameters observed for ClO_2 adsorbed on this same zeolite, the effect being the smallest for all the zeolites studied.

CHAPTER TEN

NITRIC OXIDE, NO

Nitric oxide is another stable paramagnetic molecule which normally exists in the gas phase. Beringer and Castle [161] have analyzed in detail the spectrum of NO in the gas phase, where complexities due to orbital, spin and rotational interactions are present. Early attempts to detect NO trapped in rare gas matrices were unsuccessful [162]. That it does not give rise to a detectable spectrum in these matrices is not surprising as the interaction with the environment is probably not sufficient to quench the orbital motion of the paramagnetic electron sufficiently. This shall be discussed below.

The NO molecule in its ground state is not paramagnetic. NO is a $^2\pi$ molecule. The ground state of the molecule ($^2\pi_{1/2}$) is nonmagnetic since spin and orbital angular moments are antiparallel, and the orbital magnetism just cancels the spin magnetism.

The paramagnetic character of NO results from the $^2\pi_{3/2}$ state, a consequence of the spin and orbital momenta being aligned. The $^2\pi_{3/2}$ state is separated by 121 cm^{-1} from the ground state. Both states are appreciably populated except at temperatures below about 50°K .

Sorption and magnetic susceptibility studies on nitric oxide-silica gel systems [163, 164] have indicated a partial quenching of the orbital angular momentum. It thus appears that certain environments may quench the orbital angular momentum and enable the EPR spectra to be recorded. Recently, Lunsford [165-167], Gardner and Weinberger [168], and Hoffman and Nelson [169] have reported spectra of NO in a $^2\pi$ state adsorbed on MgO, ZnO and various zeolites, in which the orbital momentum seems substantially quenched by the surface fields of the adsorbents. These surface fields were studied as well as the effect of the adsorption on the NO.

The results to be presented here are in accord with those previously reported, although in the present work a reaction of the NO with certain surfaces was observed in addition. Preparation of the samples is the same as for the adsorption of NO_2 .

10.1 Silica Gel.

Attempts were made to observe the spectrum of NO adsorbed on silica gel at 77°K but were unsuccessful. Although Solbakk  n et al [163, 164] reported that the first molecules

adsorbed at this temperature were in the excited state $^2\pi_{3/2}$ and continued up to nearly monolayer coverage, no spectrum was observed.

10.2 13X Synthetic Zeolite.

The spectrum observed for NO adsorbed on 13X synthetic zeolite at 77°K is shown in figure 40. No hyperfine structure was evident and the spectrum appears similar to that reported by Gardner et al [168]. The parameters were assigned by comparison to the simulated spectrum, figure 41, and are given in Table 3. Since any hyperfine structure is apparently less than the linewidth, the effects of this and any other broadening interactions were included in the linewidth and the spectrum was simulated using an axially symmetric g tensor.

10.3 H-Mordenite.

The spectrum observed at 77°K for NO adsorbed on synthetic H-mordenite is also similar to that reported by Gardner et al [168] and to that of Lunsford [165] reported on MgO. Some structure is evident and as an aid to analysis, the spectrum of ^{15}NO was also recorded. Figures 42 and 43 show the spectra for ^{14}NO and ^{15}NO respectively. Simulation was attempted in a similar manner to that of the 13X sample using an axially symmetric g tensor, but now including hyperfine splittings. The results are shown in Table 3. It is obvious from the resulting spectra, shown in figures 44 and 45 respectively for ^{14}NO and ^{15}NO , that the situation

TABLE 3

Reference	g values			(gauss) Hyperfine components			Medium
	g_{xx}	g_{yy}	g_{zz}	T_{xx}	T_{yy}	T_{zz}	
	g_{\perp}		g_{\parallel}				
165	1.996	1.996	1.89	33		< 10	^{14}NO adsorbed on MgO @ 77°K
169	1.994	1.994	1.873	28			^{14}NO adsorbed on 4A @ 77°K
166	1.997	1.997	1.91	31			^{14}NO adsorbed on ZnS @ 77°K
168	1.970	1.970	1.786				^{14}NO adsorbed on 13X @ 77°K
168	1.967	1.967	1.773				^{14}NO adsorbed on H-mordenite @ 77°K
168	1.990	1.990	1.859				^{14}NO adsorbed on 5A @ 77°K
	±0.001	±0.001	±0.01	±1	Line width used for simulations (gauss)		
this work	1.967	1.967	1.78		90.0		^{14}NO adsorbed on 13X @ 77°K
this work	1.994	1.994	1.87	23	35.0		^{14}NO adsorbed on H-mordenite @ 77°K
this work	1.994	1.994	1.87	38	35.0		^{15}NO adsorbed on H-mordenite @ 77°K

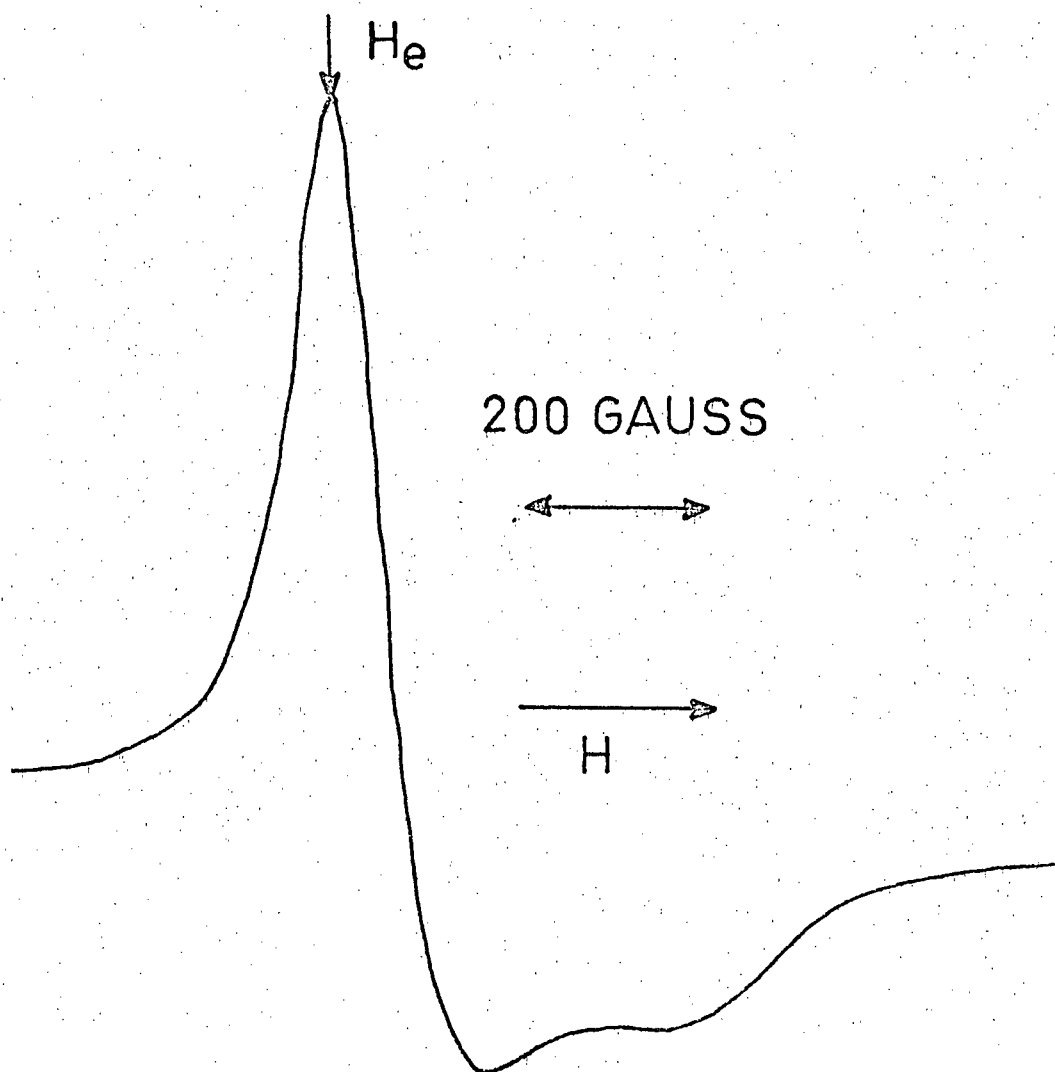


FIGURE 40. EPR spectrum of nitric oxide adsorbed on 13X synthetic zeolite, recorded at 77°K .

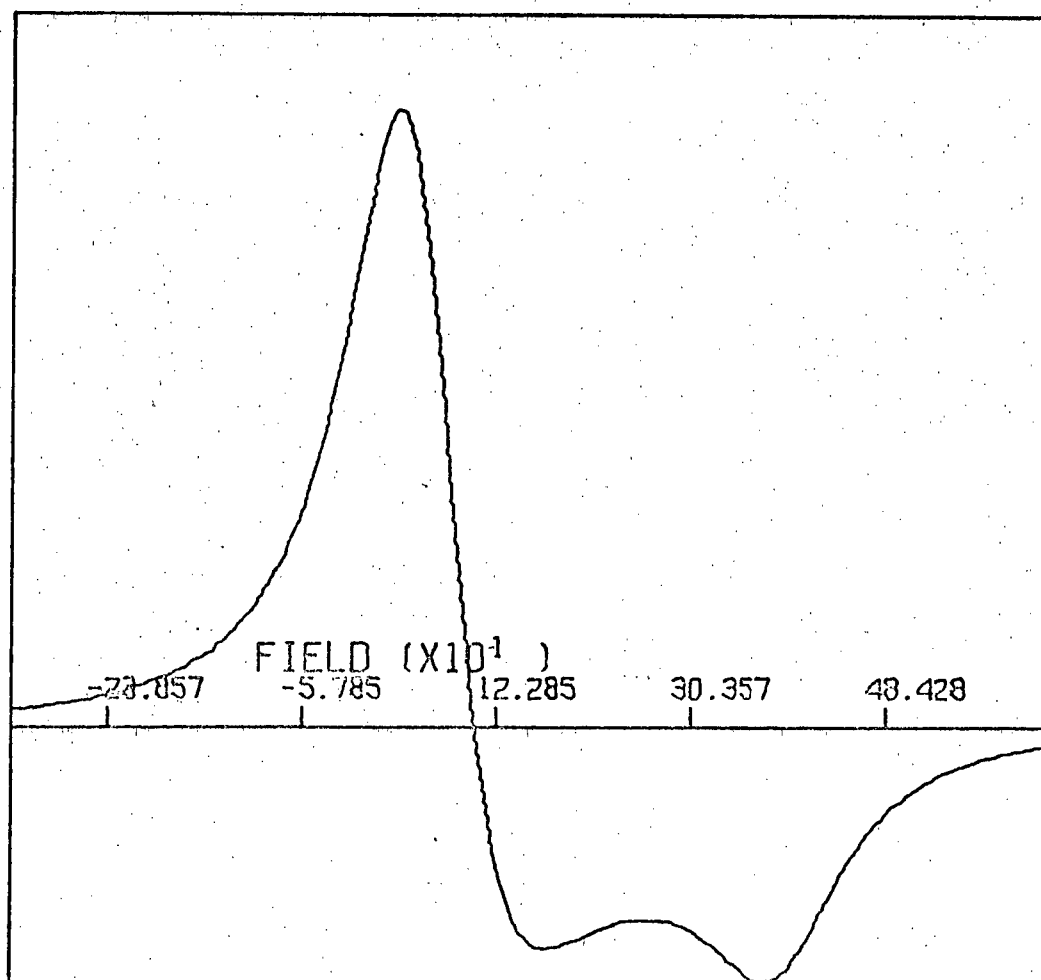


FIGURE 41. Computer simulated EPR spectrum of nitric oxide adsorbed on 13X synthetic zeolite, recorded at 77° K.

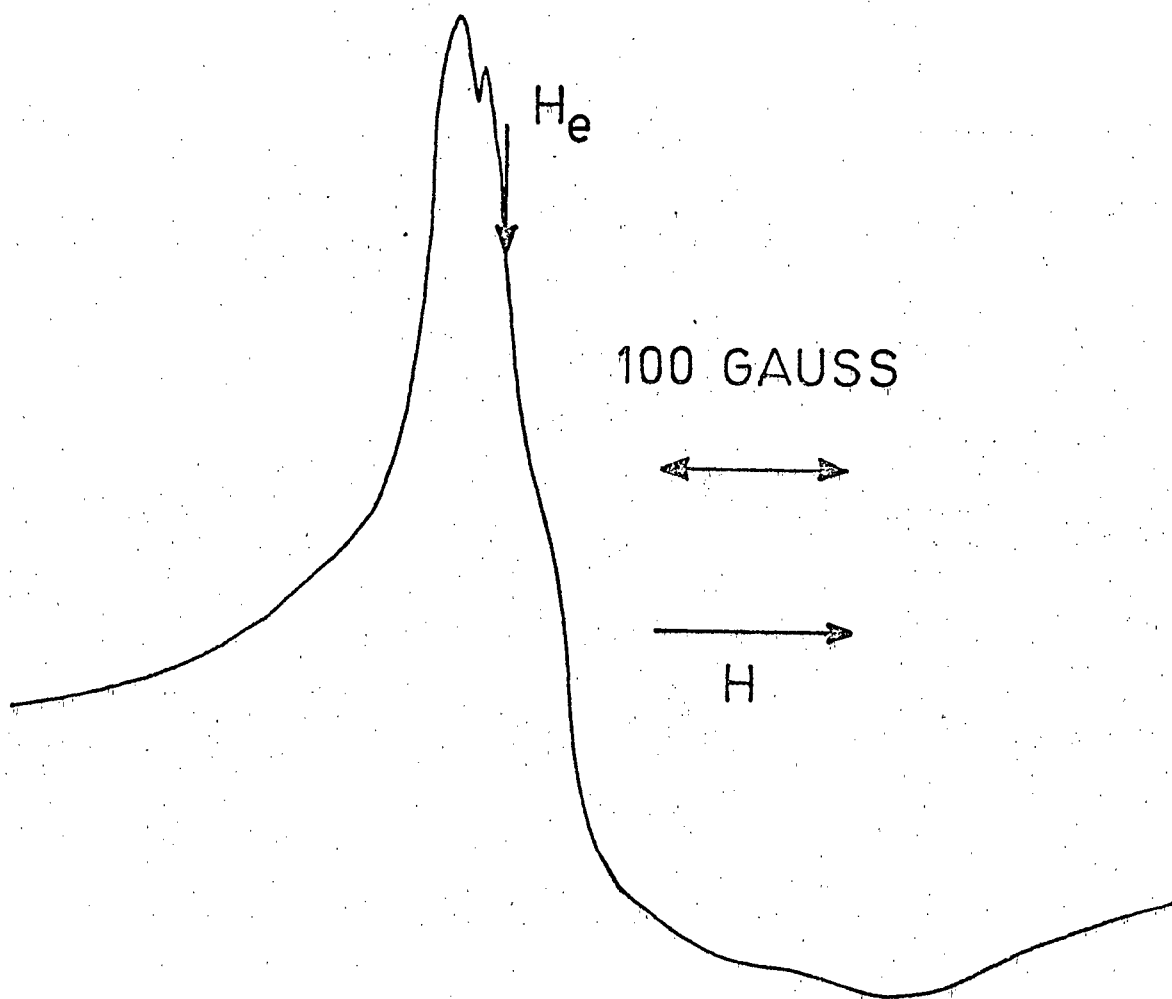


FIGURE 42. EPR spectrum of ^{14}N nitric oxide adsorbed on H-mordenite, recorded at 77°K .

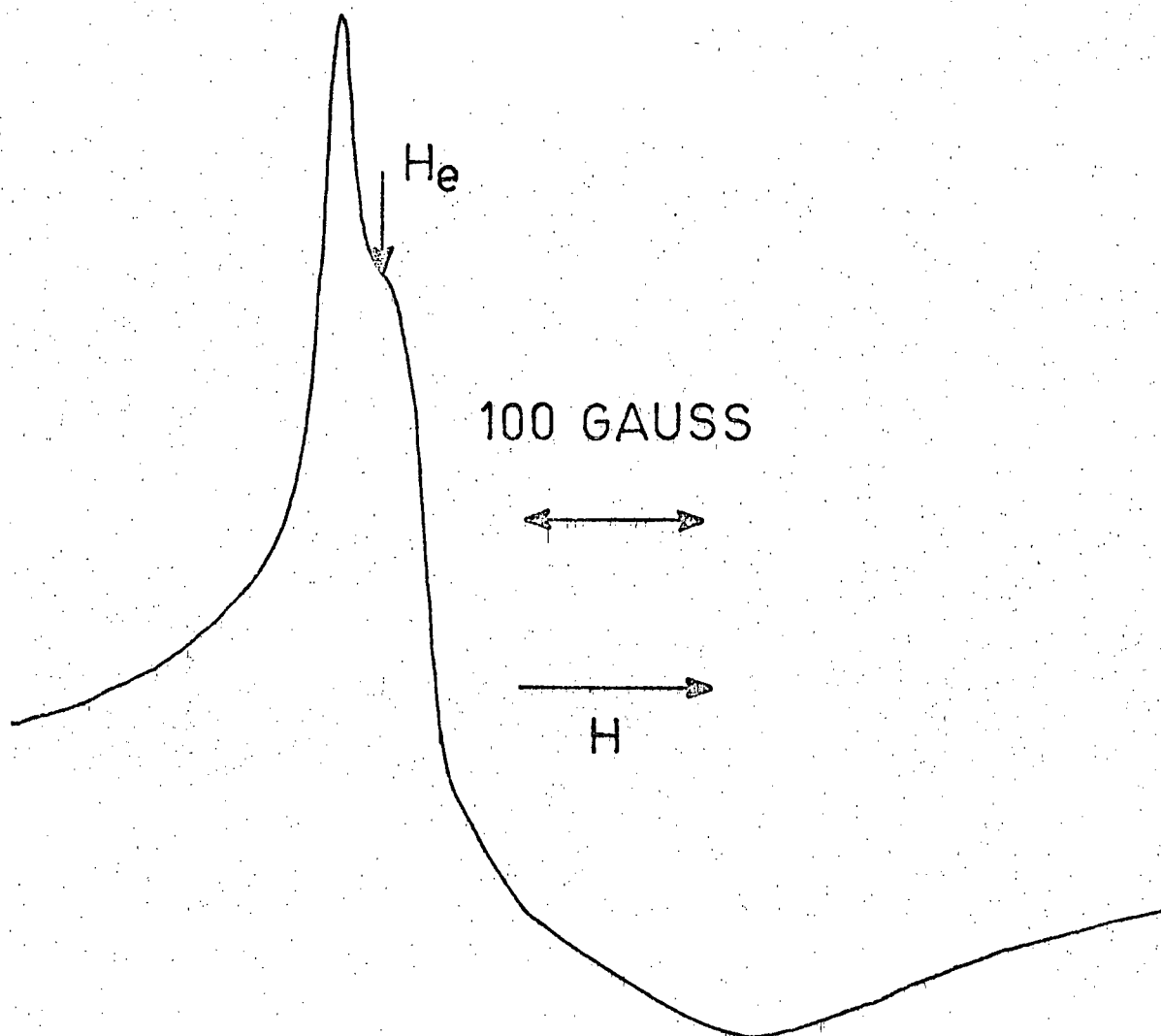


FIGURE 43. EPR spectrum of ^{15}N nitric oxide adsorbed on H-mordenite, recorded at 77°K .

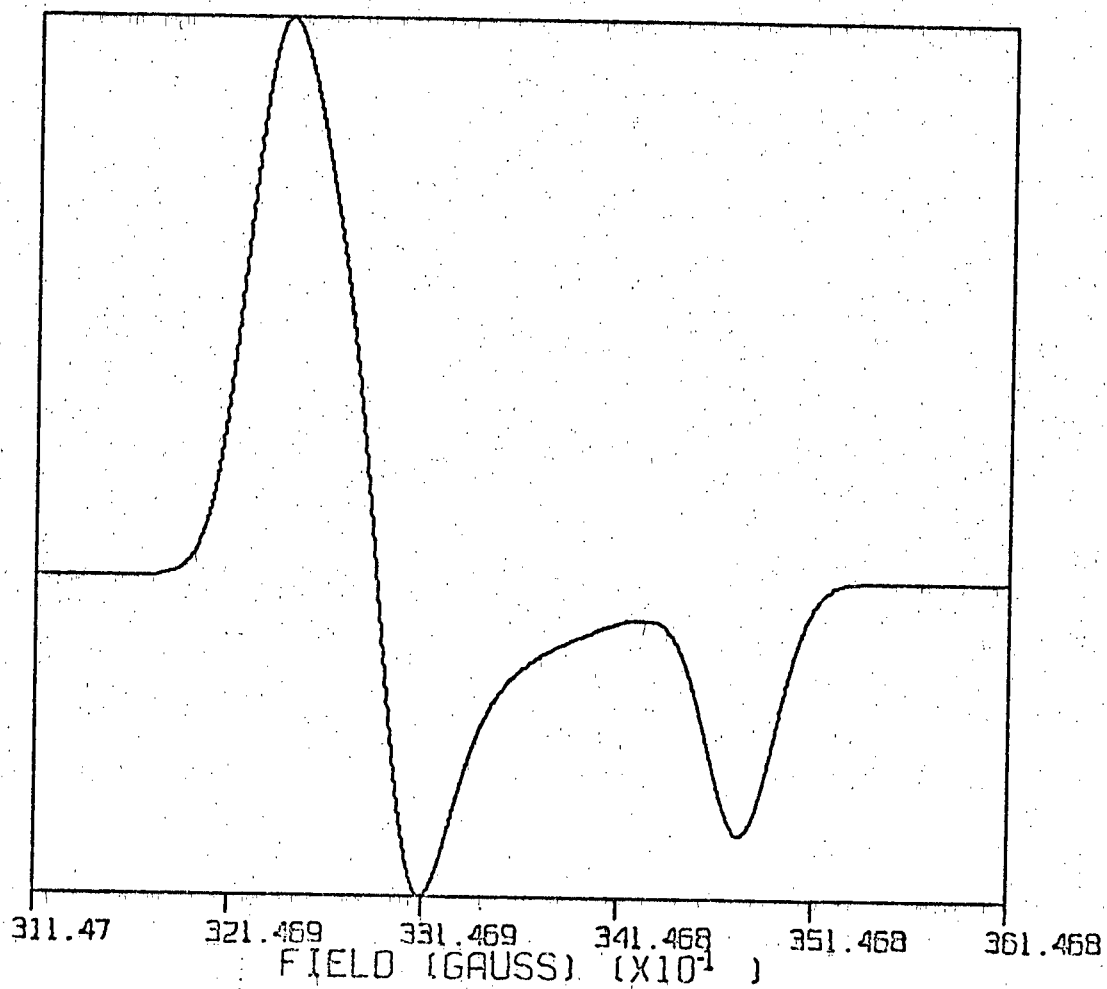


FIGURE 44. Computer simulated EPR spectrum of ¹⁴N nitric oxide adsorbed on H-mordenite, recorded at 77° K.

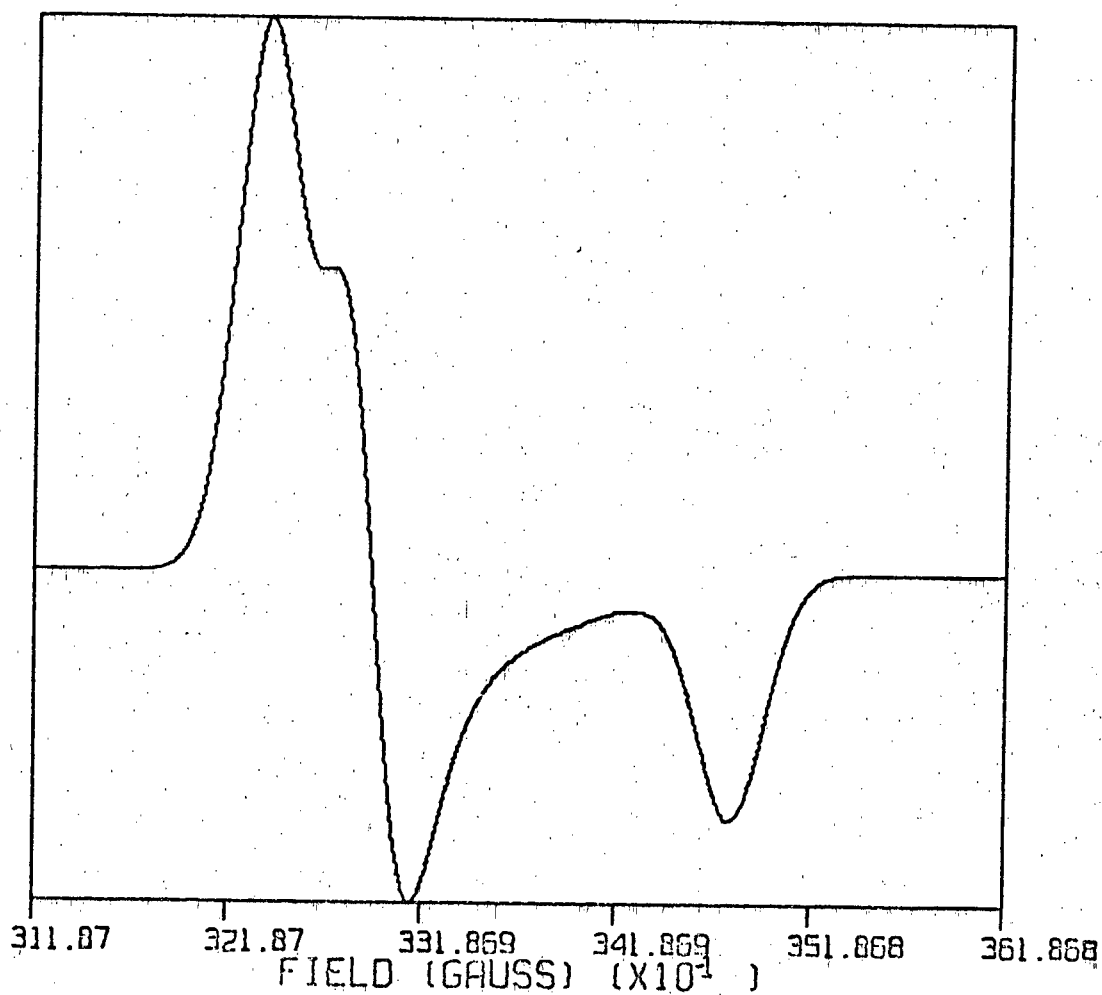


FIGURE 45. Computer simulated EPR spectrum of ¹⁵N nitric oxide adsorbed on H-mordenite, recorded at 77° K.

is more complex than this. Both samples were evacuated to remove as much adsorbed species as possible with the resulting spectrum shown in figure 46. The spectrum then observed at 77°K was identical in both cases and showed considerable structure.

10.4 Discussion.

Interaction of the surface fields with AB type π -radicals quenches the orbital momentum of these radicals. An unsymmetrical environment lifts the degeneracy of the $2p\pi^*$ orbitals (π_x and π_y orbitals, defining the N-O bond as the z-axis). For the NO molecule, the unpaired electron will be in the $2p\pi_x^*$ level in the absence of any spin-orbit interaction.

Explicit formulae for the g tensor of an electron in a $^2\pi$ state were given by Kanzig et al [170]: Δ is the crystal field splitting; λ the spin-orbit coupling constant; E, the effective energy difference between the $^2\pi$ levels and the $^2\Sigma$ levels; and k, the effective g factor for the orbital contribution (k=1 for the free molecule). The equations are given by

$$g_{zz} = g_e - 2k \left(\frac{\lambda^2}{\lambda^2 + \Delta^2} \right)^{1/2} \quad (10-1)$$

$$g_{yy} = g_e \left(\frac{\Delta^2}{\lambda^2 + \Delta^2} \right)^{1/2} - \frac{\lambda}{E} \left[1 + \left(\frac{\lambda^2}{\lambda^2 + \Delta^2} \right)^{1/2} + \left(\frac{\Delta^2}{\lambda^2 + \Delta^2} \right)^{1/2} \right] \quad (10-2)$$

$$g_{xx} = g_e \left(\frac{\Delta^2}{\lambda^2 + \Delta^2} \right)^{1/2} + \frac{\lambda}{E} \left[1 + \left(\frac{\lambda^2}{\lambda^2 + \Delta^2} \right)^{1/2} - \left(\frac{\Delta^2}{\lambda^2 + \Delta^2} \right)^{1/2} \right] \quad (10-3)$$

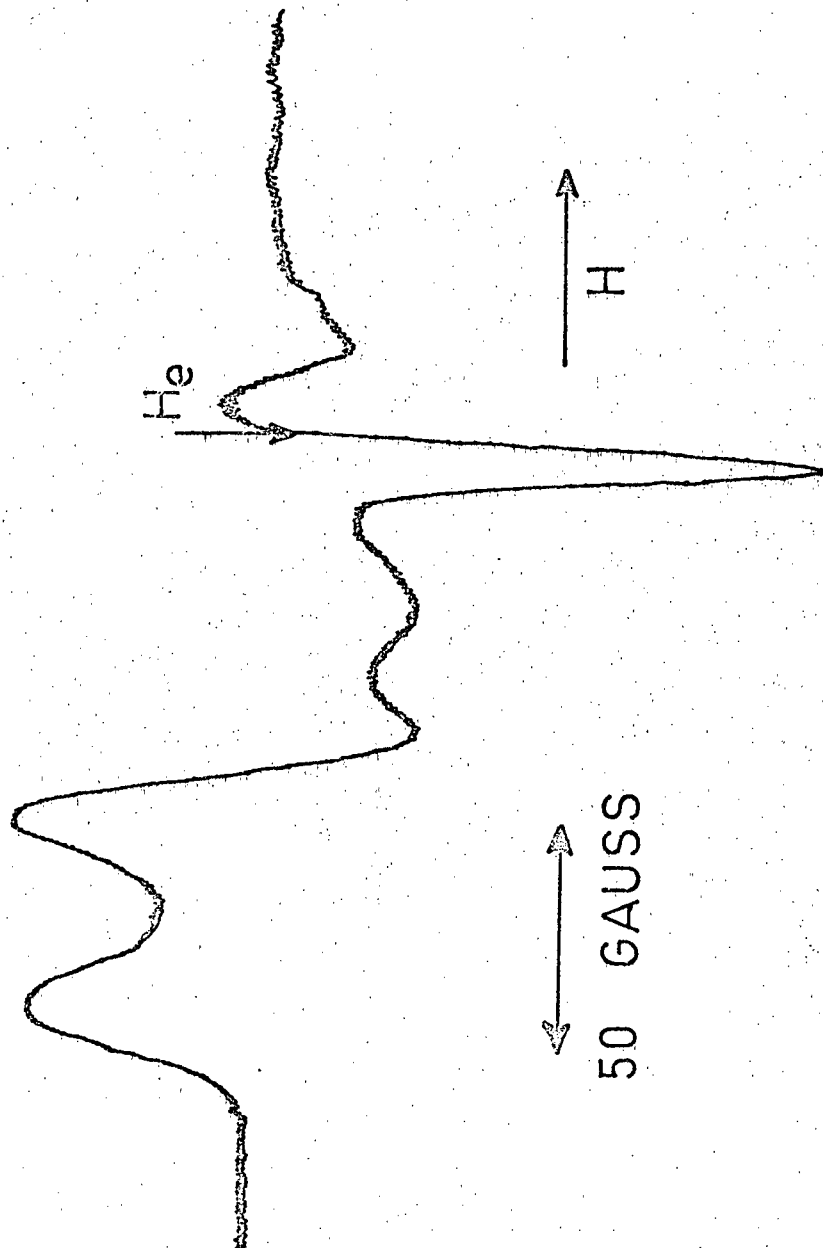


FIGURE 46. EPR spectrum observed after adsorption of nitric oxide on H-mordenite, followed by evacuation, recorded at 77° K.

The apparent axial symmetry of the observed spectra (due mainly to the linewidth) indicates λ/E must be small. The calculations of Gardner et al on the 13X and H-mordenite [168] will not be repeated here since the same adsorbents were used.

The species formed on adsorption of NO on H-mordenite and subsequent pumping of the sample is indeed curious. It is reasonable that the NO is easily removed by pumping since its dipole moment is much less than that of NO₂. A value of 0.158 D was reported by Stogryn [171]. The species is obviously not due to a nitrogen containing molecule since no change in structure was observed on adsorption of ¹⁴NO and ¹⁵NO, the nuclear spin of ¹⁵N being $I=\frac{1}{2}$ in contrast to $I=1$ for ¹⁴N. Numerous attempts at analysis using computer simulated spectra were made with no success. The presence of more than one species is possible but no evidence for this was given by tests of increasing the microwave power level.

The reaction of NO with the surface of H-mordenite has produced a species strongly attached to the surface. Failure to remove the species by pumping is evidence of this. It is likely the NO has reacted with some part of the surface to form a species which, if not chemisorbed, is very strongly attached. Terenin and co-workers [172], when studying the adsorption of NO on various zeolites using infrared spectroscopy, found that NO was adsorbed as N₂O, the oxygen freed by the reaction probably being adsorbed. Their assignment was shown to be correct by adsorbing N₂O directly. The formation of N₂O would account for identical spectra being observed for ¹⁵NO and ¹⁴NO since N₂O is not paramagnetic. The reaction of the oxygen

atom with the H-mordenite would then be responsible for the observed spectrum.

CHAPTER ELEVEN

DIFLUORAMINO RADICAL, NF_2

The NF_2 radical exists in equilibrium with its dimer tetrafluorohydrazine, N_2F_4 , at normal temperatures. The dissociation of N_2F_4 into NF_2 radicals has been studied previously (for example [173, 174]), and it has been shown that the difluoramino radical is quite stable and is capable of existing indefinitely in the free state. At room temperature and atmospheric pressure, the radical is present to the extent of only 0.05 per cent. The radical concentration reaches 90 per cent only at 573°K and one atmosphere, at 423°K and 1 mm, or at 298°K and 10^{-10} atmospheres.

The EPR spectrum observed in the gas phase consisted of a single broad line showing no hyperfine structure due to either the nitrogen or the fluorines [173]. Isotropic spectra showing

resolved hyperfine structure have been observed for NF_2 dissolved in perfluorodimethylhexane [175] and in liquid N_2F_4 [174]. Adrian et al [176] studied the NF_2 radical in an argon matrix, but were unable to offer any firm identification of the anisotropic components. Farmer et al [177] reported results for NF_2 in both argon and krypton matrices at 4.2°K . Unfortunately, neither of these studies yielded the anisotropic hyperfine parameters. More recently, Kasai and Whipple [178] studied the radical in a neon matrix at 4°K and were able to assign the observed principal tensor components to the molecular axes. A recent paper by McDowell et al [179] reported a detailed study of how an inert gas matrix and appropriate physical conditions together may influence the nature and extent of the orientation of a paramagnetic species, using NF_2 as an example. The work accomplished a complete analysis of the spectra and also a temperature study.

Results of the adsorption of the NF_2 radical on H-mordenite are reported here.

11.1 H-Mordenite.

The spectrum observed for N_2F_4 adsorbed on H-mordenite at 77°K is shown in figure 47. Several experiments were attempted with varying concentrations but this was the only reproducible spectrum observed. The observed splittings are not similar to those previously observed for the NF_2 radical in other media. H-mordenite was used as the adsorbent for these experiments since it has

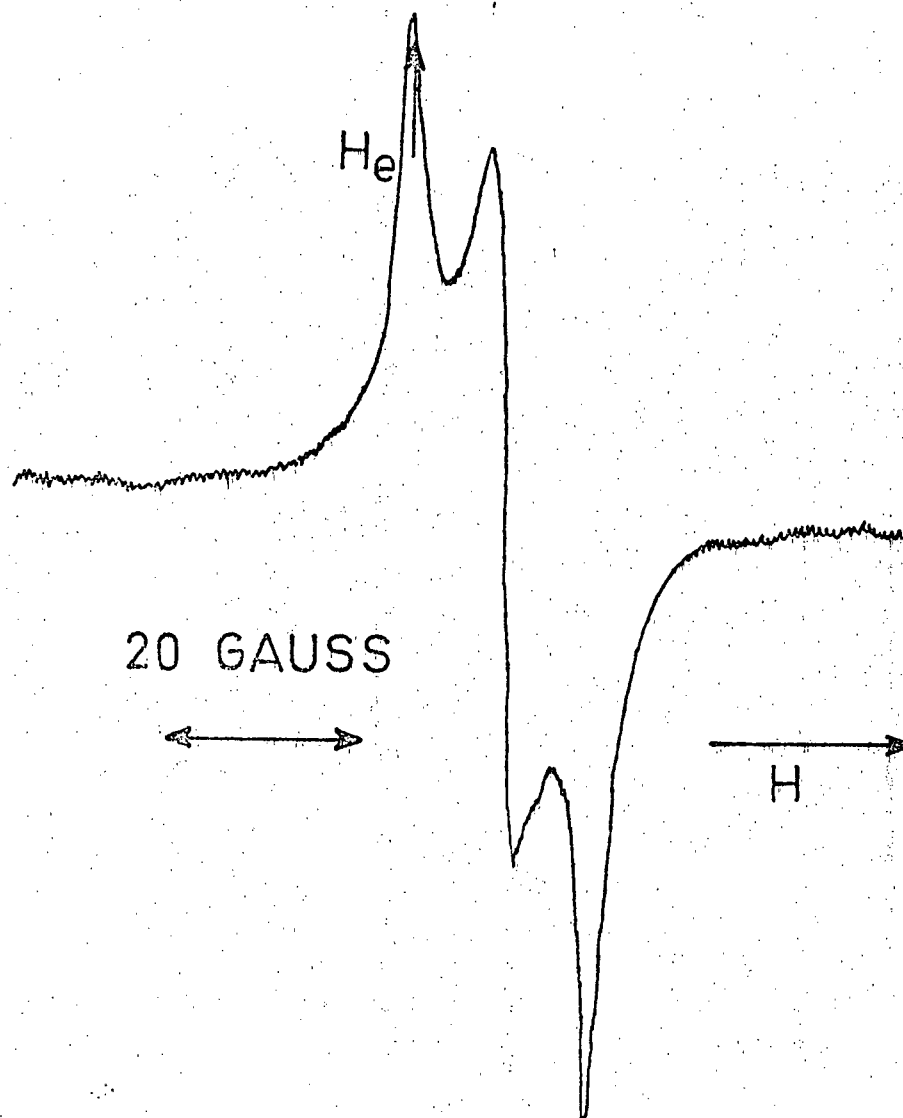


FIGURE 47. EPR spectrum observed after adsorption of N_2F_4 on H-mordenite, recorded at 77° K.

produced consistent results with the other radicals. Computer simulations of the observed spectrum are shown in figure 48. The parameters are given in Table 4.

11.2 Discussion.

The NF_2 radical is valence isoelectronic with ClO_2 , having the unpaired electron in a b_1 antibonding π orbital. The ground electronic state of the molecule is 2B_1 . The expected EPR spectrum of the radical should show hyperfine splitting due to both the fluorines and the nitrogen. The lack of hyperfine structure could be attributed to rapid recombination of the radicals, in fact, rapid recombination could even obliterate the entire spectrum. The spectrum observed in 5A molecular sieve by Colburn et al [180] did indeed show well resolved hyperfine structure with measured ^{14}N and ^{19}F couplings of 16 and 56 gauss respectively. The reported g value was 2.009. It was assumed the N_2F_4 was screened out of the zeolite eliminating much line broadening and the spectrum was due to freely rotating NF_2 radicals.

The spectrum observed in this study has been attributed to a species having an anisotropic g tensor with no observable hyperfine structure. Table 4 gives the assigned values. Figure 48a is an attempt to simulate the spectrum as due to an isotropic g value with observed splittings due to a nitrogen nucleus. A good fit could not be obtained with regard to either intensities or line positions. As was the case with NO adsorbed on H-mordenite, the NF_2 or N_2F_4 has probably reacted with the surface to form a

TABLE 4

Reference	g-values (± 0.0005)				Isotropic Hyperfine component (gauss)
this work figure 48b	g_{xx}	g_{yy}	g_{zz}	g avg	A_o
	2.0151	2.0084	2.0025		
this work figure 48a				2.0100	7.8

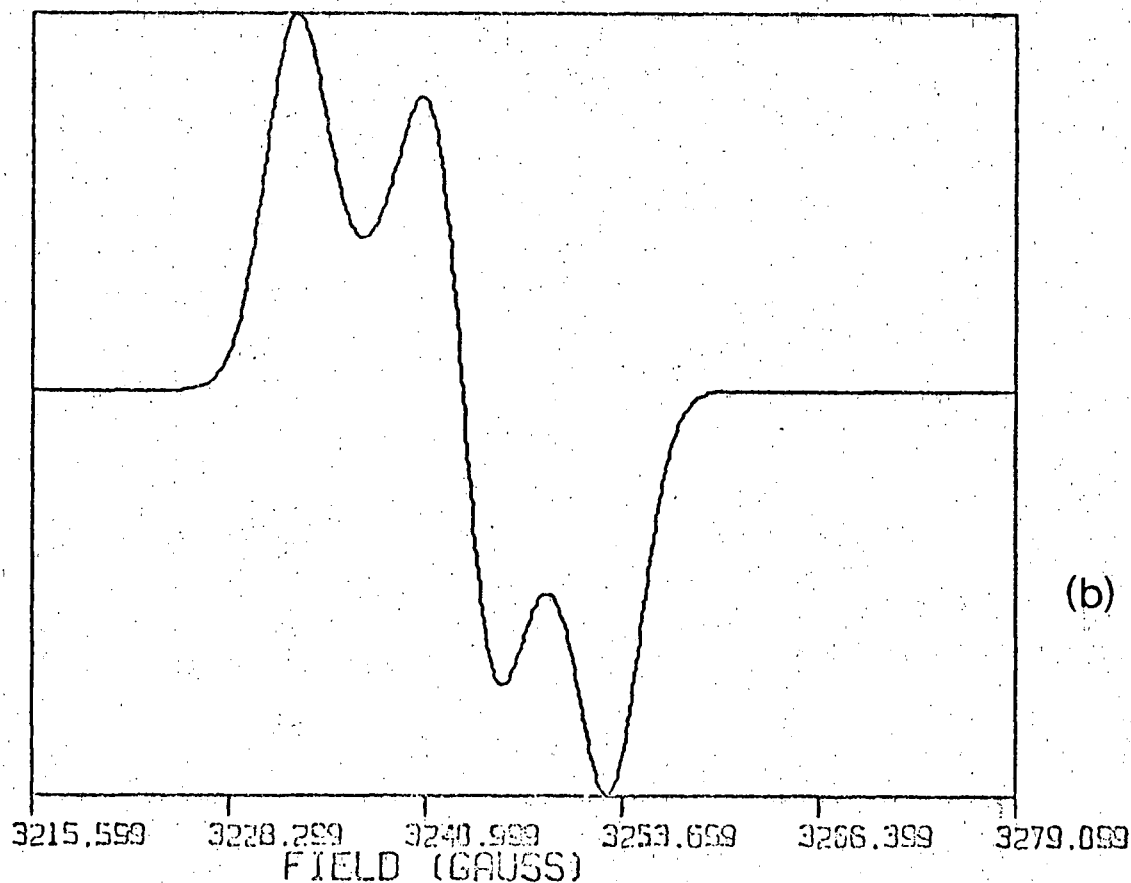
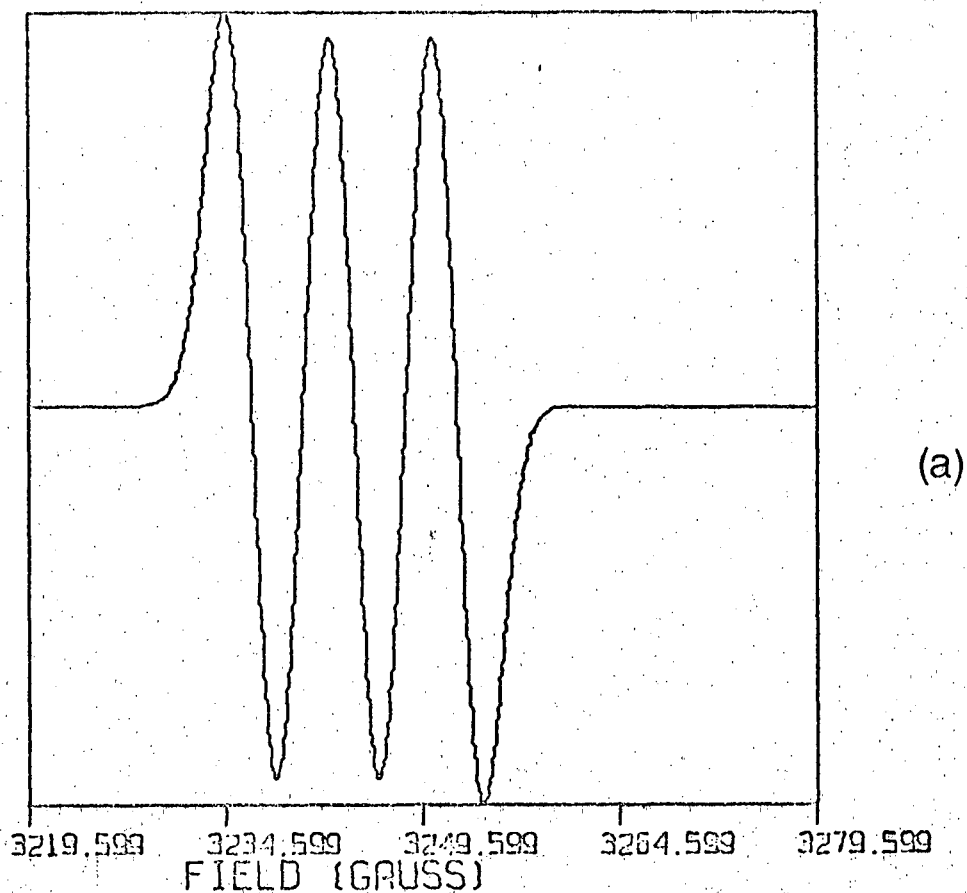


FIGURE 48. Computer simulated EPR spectra of species formed on adsorption of N_2F_4 on H-mordenite, recorded at 77° K

a) isotropic g and hyperfine tensor

b) anisotropic a tensor, no hyperfine

non-paramagnetic species and a paramagnetic species having no observable hyperfine structure.

CHAPTER TWELVE

SUMMARY

This chapter is intended as a summary of the work completed in this thesis with a view to possible further applications of studies in this area. Greater amounts of information are steadily becoming available on the topology of the various surfaces studied, the area where lack of knowledge has been the most outstanding. More detailed conclusions could then be reached concerning the interactions at these gas-solid interfaces.

The main species which has been studied here, chlorine dioxide, has shown widely different interactions with the various adsorbents used. The H-mordenite samples yielded EPR spectra having measured parameters the least changed from those obtained in media other than adsorbents. This indicates the ClO_2 molecules

are physically trapped in the interior of this zeolite, having little interaction with the internal electrostatic fields. The interaction with silica gel is somewhat similar, although the amorphous structure of this adsorbent makes it difficult to quantitatively place the ClO_2 molecules in any particular area of its internal surface. 13X, on the other hand, has an ordered structure which enables one, from data obtained from the experiments, to visualize the actual adsorption sites involved. These have been discussed in Chapter Eight. The results for the other zeolites may similarly be analyzed with regard to adsorption sites and interactions with the internal surface fields.

A publication concerning a study of ClO_2 adsorbed on synthetic zeolites [181] has recently appeared in the literature. The spectra obtained on the zeolites 13X and 10X were not analyzed in terms of actual adsorption sites, probably due to the fact that successful computer simulation of the spectra could not be obtained. The two distinguishable sites observed in the present study were not noticed. The linewidths for the spectra reported in their publication would have obliterated these features.

This same paper by Pietrzak and Wood also contained a study of NO_2 adsorbed on these same zeolites. The paper contained comparable spectra to these obtained in this study for the 13X synthetic zeolite. Results obtained here for NO_2 were not

significantly different from those of NO_2 studied in other media. In fact, the spectra observed on the synthetic zeolite H-mordenite is in excellent agreement to that for NO_2 in an N_2O_4 matrix, both media studied at 77°K . The proposed adsorption sites for the NO_2 molecules in this zeolite are the small pockets lining the main passage-ways. In the case of ClO_2 , the observed spectra correlated well with the structures of the 13X zeolites, whereas for NO_2 this was not so. Specific adsorption sites may only be assigned to the zeolite, H-mordenite. This is attributed to the fact that ClO_2 has a larger dipole moment than NO_2 which enables it to interact more strongly with specific cation sites in 13X. In H-mordenite, these sites are not as well-defined, and coupled with the small dipole moment of the NO_2 , the observed spectra suggest the molecules to be confined in these side pockets.

The spectra observed for nitric oxide adsorbed on various zeolites show yet another possible effect of adsorption. While the spectra which are first apparent on adsorption are similar to those observed by others on a variety of surfaces, pumping of the sample to decrease the concentration of the NO on the surface yields a new spectrum. This is assigned to a species formed by a reaction of the NO molecules with the surface. This new species has been shown not to contain nitrogen. This is confirmed by the fact that identical EPR spectra are observed for both ^{15}NO and ^{14}NO . The observance of chemical reactions on surfaces either through the formation of a new species or a

change in the spectra for the original species is then another area with wide possibilities.

The use then, of the EPR technique, in the study of the gas-solid interface can generally be categorized in three areas:

Information about the nature of the surfaces is possible in many cases and the opportunity for study here is limited only to the number of surfaces which yield EPR signals.

The addition of gaseous molecules to these surfaces widens the scope considerably. In these cases, as was found for ClO_2 , this technique may provide an "inert matrix" which perhaps enables the species in question to be studied with greater facility than other EPR techniques, or may even provide a means of study where others have not as yet been found. Included in this area also are the possibilities of reaction of the gaseous molecules with the surfaces to yield new species; either a new adsorbed species, or even spectra now due to the surface, whereas before the adsorption, none was evident. The latter was the case with nitric oxide. The opportunities are extremely large in this particular area.

The last general area where the use of EPR has found value in these studies is in the area of the dynamical behaviour of the adsorbed molecules. The motion of the adsorbed molecules, either hindered or free may be studied at a variety of temperatures by this technique. The publication of Pietrzak and Wood [181] mentioned earlier was such a study, although it was not completely

successful in the case of ClO_2 .

The opportunities for future work in this area, complemented by other spectroscopic techniques, look promising. The EPR technique has certainly not been explored to its fullest in any of the three areas mentioned. Since knowledge of the surfaces is vital to an understanding of the results, the more accurate the information available in this area, the better the conclusions. To this end, perhaps a combination of XRD and EPR techniques would prove very valuable. Modifications to the surfaces could then be studied in regard to their effect on the observed spectra. A single species could then be studied in greater detail by varying the surface conditions systematically. In any case, the future leaves much to be discovered in this area.

REFERENCES

1. R.P. Eischens and W.A. Pliskin, *Advances in Catalysis* X (W.G. Frankenberg, V.I. Komarevsky, E.K. Rideal, eds.), Academic Press, N.Y., 1958, p. 1.
2. V. Crawford, *Quart. Rev.*, 14, 378 (1960).
3. A.V. Kiselev and V.I. Lygin, *Russ. Chem. Rev.*, 31, 175 (1962).
4. M.R. Basila, *Applied Spectroscopy Reviews*, 1, 289 (1968).
5. M.L. Hair, *I R Spectroscopy in Surface Chemistry*, M. Dekker, N.Y., 1967.
6. L.H. Little, *The I R Spectra of Adsorbed Molecules*, Butterworth, London, 1966.
7. M.J.D. Low, *The Solid-Gas Interface*, (E.A. Flood, ed.), Vol. 2, p. 947, M. Dekker, N.Y., 1967.
8. N. Fuschillo and J.G. Aston, *J. Chem. Phys.*, 24, 1277 (1956).
9. A.A. Galkin and I.V. Matyash, *Ukr. Fiz. Zh.*, 7, 54 (1962).
10. H. Winkler, *Z. Naturforsch.*, 16A, 780 (1961).
11. H.A. Resing, J.K. Thompson, and J.J. Krebs, *J. Phys. Chem.*, 68, 7 (1964).
12. D. Graham and W.D. Phillips, *Surface Activity*, Vol. 2, (J.A. Schulman, ed.), Butterworth, London, 1957, p. 22.
13. Y. Ayant, P. Ducros, X. Pare and M. Soutif, *Compte Rend.*, 252, 550 (1960).
14. J. Fraissard, I. Solomon, R. Caillat, J. Elston, and B. Imelik, *J. Chem. Phys.*, 60, 676 (1963).
15. V.I. Kvlividze, N.M. Ievskaya, T.S. Egarova, V.F. Kiselev, and I.D. Sokolov, *Kinetika i Kataliz*, 3, 91 (1962).
16. R. Livingston, A. Zeldes, and E.A. Taylor, *Discuss. Faraday Soc.*, 19, 166 (1955).
17. J. Turkevitch and Y. Fujita, *Science*, 152, 1619 (1966).
18. C.B. Colburn, R. Ettinger, and F.A. Johnson, *Inorg. Chem.*, 3, 455 (1964).

19. H. Kayser, Wied. Ann. 14, 451 (1881).
20. M.M. Dubinin, Quart. Rev. Chem. Soc., 9, 101, (1959), and Chem. Rev., 60, 235 (1960).
21. S. Brunauer, L.S. Deming, W.S. Deming, and E. Teller, J. Am. Chem. Soc., 62, 1723 (1940).
22. I. Langmuir, J. Am. Chem. Soc., 38, 2267 (1916),
J. Am. Chem. Soc., 40, 1361 (1918),
Phys. Rev. 6, 79 (1915),
and J. Am. Chem. Soc. 54, 2798 (1932).
23. S. Brunauer, P.H. Emmett, and E. Teller, J. Amer. Chem. Soc., 60, 309 (1938).
24. B.P. Bering, M.M. Dubinin, V.V. Serpinsky, J. Colloid Sci., 21, 378 (1966).
25. M.M. Dubinin and E.D. Zaverina, Zh. Fiz. Kin., 21, 1351 (1947) and 23, 1129 (1949).
26. F. London, Z. Physik., 63, 245 (1930), and
Z. Physik. Chem., 11, 222 (1930).
27. J.E. Lennard-Jones, Proc. Roy. Soc. Lond., A, 106, 463 (1924).
28. R.M. Barrer, J. Colloid Sci., 21, 415 (1966).
29. J.H. de Boer, Advances in Catalysis, 8, 33, Academic Press Inc., N.Y., (1956).
30. L.E. Drain and J.A. Morrison, Trans. Faraday Soc., 49, 654 (1953).
31. J.W. McBain, The Sorption of Gases and Vapors by Solids, George Rutledge and Sons, Ltd., London, 1932.
32. R.M. Barrer, Proc. Roy. Soc., London, A167, 393 (1938).
33. R.M. Barrer, J. Chem. Soc., 2158 (1948).
34. R.M. Barrer, Disc. Faraday Soc., 40, 206 (1944).
35. R.M. Barrer and D.A. Ibbitson, Trans. Faraday Soc., 40, 195 (1944).
36. D.W. Breck, W.G. Eversole, and R.M. Milton, J. Am. Chem. Soc., 78, 2338 (1956).
37. R.M. Milton, U.S. Patent 2,882,243 and 2,882,214, April 14, 1959.

38. W. Loewenstein, Amer. Miner., 39, 92 (1954).
39. J. Selbin and R.B. Mason, J. Inorg. Nucl. Chem., 20, 222, 1961.
40. R.M. Barrer et al., J. Chem. Soc., 195 (1959).
41. R.M. Barrer, Endeavour, 23, 122 (1964).
42. R.M. Barrer and L.V.C. Rees, Trans. Faraday Soc., 50, 852 (1954).
43. R.M. Barrer and J.W. Baynham, J. Chem. Soc., 2892 (1956).
44. R.M. Barrer and D.L. Peterson, Phys. Chem., 68, 3427 (1964).
45. W. Nowacki and G. Bergerhoff, paper 3.13, 4th International Congress of Crystallography, Montreal, Canada, July 1957.
46. L. Broussard and D.P. Shoemaker, J. Am. Chem. Soc., 82, 1041 (1960).
47. R.M. Barrer, F.W. Bultitude, and J.W. Sutherland, Trans. Faraday Soc., 53, 1111 (1957).
48. P.E. Pickert, J.A. Rabo, E. Dempsey, and V. Schomaker, Proc. 3rd Intern. Congr. Catalysis, Amsterdam, 1964, Vol. 1, p. 714, Wiley, N.Y., 1965.
49. J.A. Rabo, C.L. Angell, P.H. Kasai and V. Schomaker, Disc. Faraday Soc., 41, 328 (1966).
50. T.B. Reed and D.W. Breck, J. Am. Chem. Soc., 78, 5972 (1956).
51. R.M. Barrer and I.S. Kerr, Trans. Faraday Soc., 55, 1915 (1959).
52. R.M. Barrer and W.M. Meier, Trans. Faraday Soc., 54, 1074 (1958).
53. W.M. Meier, Z. Krist., 115, 439 (1961).
54. R.M. Barrer and D.L. Peterson, Proc. Roy. Soc. Lond., A280, 466 (1964).
55. A.M. Portis, Phys. Rev., 91, 1071 (1953).
56. L. Petrakis, J. Chem. Educ., 44, 432 (1967).
57. C.P. Poole, Jr., ESR - A Comprehensive Treatise on Experimental Techniques, Interscience Publishers, N.Y., 1967.
58. P.B. Ayscough, ESR in Chemistry, Methuen and Co. Ltd., London, 1967.
59. G.E. Pake, Paramagnetic Resonance, W.A. Benjamin, Inc., N.Y., 1962.

60. H.M. Assenheim, Introduction to ESR, Hilger and Watts Ltd., London, 1966.
61. A. Carrington and A.D. McLachlan, Introduction to Magnetic Resonance, Harper and Row, N.Y. 1967.
62. A. Abragam and M.H.L. Pryce, Proc. Roy. Soc. Lond., A205, 135 (1951).
63. B. Bleaney and K.W.H. Stevens, Rep. Prog. Phys., 16, 108 (1955).
64. K.D. Bowers and J. Owens, Rep. Prog. Phys., 18, 304 (1955).
65. A. Carrington and H.C. Longuet-Higgins, Quart. Rev., 14, 427 (1960).
66. R.H. Sands, Phys. Rev., 99, 1222 (1955),
67. N. Bloembergen and T.J. Rowland, Acta. Met. 1, 731 (1953) and Phys. Rev., 97, 1679 (1955),
68. R.P. Kohin and C.P. Poole, Jr., Bull. Am. Phys. Soc. II, 3, 8 (1960).
69. F.K. Kneubühl, J. Chem. Phys., 33, 1074 (1960) and Helv. Phys. Acta, 35, 259 (1962).
70. D.J.E. Ingram and J.E. Bennett, Phil. Mag., 45, 545 (1954).
71. J.G. Castle, Phys. Rev., 95, 846 (1954).
72. J. Uebersfeld and E. Erb, Compt. Rend., 243, 363 (1956).
73. C. Jackson, H. Harker, and W.F.K. Wynne-Jones, Nature, 182, 1154 (1958).
74. H. Harker, C. Jackson, and W.F.K. Wynne-Jones, Proc. Roy. Soc. Lond., A 262, 328 (1961).
75. R.A. Weeks and C.M. Nelson, J. Am. Ceram. Soc., 43, 399 (1960).
76. S. Lee and P.J. Bray, J. Chem. Phys., 39, 2862 (1963).
77. Y. Nakai, Bulletin Chem. Soc. Japan, 37, 1089 (1964).
78. G.M. Muha, J. Phys. Chem., 70, 1390 (1966).
79. R.J. Faber and M.T. Rogers, J. Am. Chem. Soc., 81, 1849 (1959).
80. N.N. Buknov, V.V. Voevodskii, L.S. Polyak, and Yu.D. Tsvetkov, Optika i Spect., 6, 565 (1959).

81. V.B. Kazanski, G.B. Pariiskii, and V.V. Voevodskii, *Kinetika i Kataliz*, 1, 539 (1960).
82. V.B. Kazanskii, G.B. Pariiskii, and A.I. Burshtein, *Optika i Spect.*, 13, 45 (1962).
83. J.B. Peri and A.L. Hensley, Jr., *J. Phys. Chem.*, 72, 2926 (1968).
84. V.B. Kazanskii and G.B. Pariiskii, *Kinetika i Kataliz*, 2, 507 (1961).
85. G.B. Pariiskii, G.M. Zhidomirov, and V.B. Kazanskii, *Zhurnal Strukturnoi Khimii*, 4, 364 (1962).
86. V.B. Kazanskii, G.B. Pariiskii, I.V. Aleksandrov, and G.M. Zhidomirov, *Fizika Tverdogo Tela*, 5, 649 (1963).
87. A.P. Bobrovskii and V.E. Kholmogorov, *Teoreticheskaya i Eksperimental'naya Khimiya*, 3, 112 (1967).
88. C.L. Gardner and E.J. Casey, *Can. J. Chem.*, 46, 207 (1967).
89. T. Tanei, *Bulletin Chem. Soc. Japan*, 41, 833 (1967).
90. M. Miura, A. Hasegawa, and Y. Yamada, *Bulletin Chem. Soc. Japan*, 41, 1320 (1968).
91. O. Edlund, P.O. Kinell, A. Lund, and A. Shimizu, *J. Chem. Phys.*, 46, 3678 (1967) and *J. Phys. Chem.*, 73, 4175 (1969).
92. J.J. Rooney and R.C. Pink, *Trans. Faraday Soc.*, 58, 1632 (1962).
93. G.M. Muha, *J. Phys. Chem.*, 71, 633 (1967).
94. J. Turkeyitch and Y. Fujita, *Science*, 152, 1619 (1966).
95. M. Fujimoto, H.D. Gesser, B. Garbutt, and A. Cohen, *Science*, 154, 381 (1966).
96. M. Fujimoto, H.D. Gesser, B. Garbutt, and M. Shimizu, *Science*, 156, 1105 (1967).
97. M. Shimizu, H.D. Gesser, and M. Fujimoto, *Can. J. Chem.*, 47, 1375 (1969).
98. N. Shimamoto, Y. Fujita, and T. Kwan, *Bulletin Chem. Soc. Japan*, 43, 580 (1970).
99. Y.I. Petcherskaya, V.B. Kazanskii, and V.V. Voevodskii, *Actes du Deuxième Congrès International de Catalyse, 1960, Paris*, p. 2121.

100. V.V. Voevodskii, Proc. 3rd International Congress of Catalysis, 1964, Amsterdam, p. 88.
101. V.B. Kasenskii and G.B. Pariiskii, Proc. 3rd International Congress of Catalysis, p. 367, 1964.
102. D.N. Stamires and J. Turkevitch, J. Am. Chem. Soc., 86, 757 (1963).
103. D.N. Stamires and J. Turkevitch, J. Am. Chem. Soc., 86, 749 (1963).
104. M.N. Zhavoronkov, E.N. Topchieva, and V.B. Golubev, Doklady Akademii Nauk SSSR, 180, 898 (1968).
105. G.A. Helcké and R. Fantechi, Mol. Phys., 17, 65 (1969).
106. K.M. Wang and J.H. Lunsford, J. Phys. Chem., 74, 1512 (1970).
107. P.H. Kasai, J. Chem. Phys., 43, 3322 (1965).
108. G.A. Noble, R.A. Serway, A. O'Donnell, and E.S. Freeman, J. Phys. Chem., 71, 4326 (1967).
109. D.E. Wood and T.M. Pietrzak, J. Chem. Phys., 46, 2973 (1967).
110. R.L. Mays, P.E. Pickert, A.P. Bolton, and M.A. Lanewala, The Oil and Gas Journal, May 1965, p. 91.
111. J. King, Jr., and S.W. Benson, J. Chem. Phys., 44, 1007 (1966).
112. S.W. Benson and J. King, Jr., Science, 150, 1710 (1965).
113. J.A. Rabo, P.E. Pickert, D.N. Stamires, and J.E. Boyle, Actes du Deuxième Congrès International de Catalyse, 1960, Paris, p. 2055.
114. P.E. Pickert, J.A. Rabo, E. Dempsey, and V. Schomaker, Proc. 3rd International Congress of Catalysis, 1964, Amsterdam, p. 714.
115. J.A. Rabo, C.L. Angell, P.H. Kasai, and V. Schomaker, Disc. Faraday Soc., 41, 328 (1966).
116. G.J. Hoijtink, Recueil des Travaux Chimiques des Pays-bas, 76, 869 (1957).
117. G.J. Hoijtink, The Mechanism of Heterogeneous Catalysis, (J.H. de Boer, ed.), Elsevier, 1959, p. 90.
118. R.M. Barrer and R.M. Gibbons, Trans. Faraday Soc., 59, 2569 (1963).

119. R.M. Barrer and R.M. Gibbons, *Trans. Faraday Soc.*, 61, 948 (1965).
120. L.V. Cribkova, I.A. Sarakhov, N.A. Tverdokhlebov, and Z.A. Ryabikova, *International Chemical Engineering*, 9, 503 (1969).
121. H.S. Sherry, *Ion Exchange*, (J.A. Marinsky, ed.), Vol. 2, Chapter 3, p. 89.
122. G. Brauer, ed., *Handbook of Preparative Inorganic Chemistry*, Vol. 1, Academic Press, N.Y., 1963, p. 301.
123. J.D. Swalen and H.M. Gladney, *IBM Journal of Research and Development*, 8, 515 (1964).
124. H.M. Gladney and J.D. Swalen, *EPR (Revised - General EPR Spectral Program Exchange*, Indiana University, 1964.
125. R. Lefebvre and J. Maruani, *J. Chem. Phys.*, 42, 1480 (1965).
126. R. Lefebvre and J. Maruani, *J. Chem. Phys.*, 42, 1496 (1965).
127. J.A.R. Coope, *J. Chem. Phys.*, 44, 4431 (1966).
128. K. Itoh, *Chem. Phys. Letters*, 1, 235 (1967).
129. C.R. Byfleet, D.P. Chong, J.A. Hebden, and C.A. McDowell, *J. Mag. Resonance*, 2, 69 (1970).
130. R.E.D. McClung, *Canadian Journal of Physics*, 46, 2271 (1968).
131. L.D. Landau and E.M. Lifshitz, *Quantum Mechanics*, Addison-Wesley, Reading, Mass., 1958.
132. B. Bleaney, *Phil. Mag.*, 42, 441 (1951).
133. J.E. Bennett and D.J.E. Ingram, *Phil. Mag.*, 1, 109 (1956).
134. N. Vanderkooi, Jr. and T.R. Poole, *Inorganic Chemistry*, 5, 1351 (1966).
135. P.W. Atkins, J.A. Brivati, N. Keen, M.C.R. Symons, and P.A. Trevalion, *J. Chem. Soc.*, 4785 (1962).
136. J.R. Byberg, S.J.K. Jensen, and L.T. Muus, *J. Chem. Phys.*, 46, 131 (1967).

137. R.S. Eachus, P.R. Edwards, S. Subramanian, and M.C.R. Symons, J. Chem. Soc., A, 1704 (1968).
138. R.S. Mulliken, Revs. Modern Phys., 14, 204 (1942).
139. A.D. Walsh, J. Chem. Soc., 2260 (1953).
140. R.F. Curl, J.L. Kinsey, J.G. Baker, D.H. Baird, G.R. Bird, R.F. Heidelberg, T.M. Sudgen, D.R. Jenkins, and C.N. Kenney, Phys. Rev., 121, 1119 (1961).
141. R.F. Curl, R.F. Heidelberg, and J.L. Kinsey, Phys. Rev., 125, 1993 (1962).
142. J.K. Ward, Phys. Rev., 96, 845 (1954).
143. W.M. Tolles, J.L. Kinsey, R.F. Curl, and R.F. Heidelberg, J. Chem. Phys., 37, 927 (1962).
144. A.D. Buckingham, Quart. Rev., Chem. Soc. Lond., 14, 183 (1959).
145. C.J.F. Böttcher, Recueil des Travaux Chimiques des Pays-Bas, 64, 360 (1945).
146. E. Dempsey, Molecular Sieves, Society of Chemical Industry Special Publication, 1968, p. 293.
147. P.P. Ewald, Ann. Physik, 64, 254 (1921).
148. P.W. Atkins, M.C.R. Symons, and H.W. Wardale, J. Chem. Soc., 5215 (1964).
149. J.G. Castle and R. Beringer, Phys. Rev., 80, 114 (1950).
150. D.W. James and R.C. Marshall, J. Phys. Chem., 72, 2963 (1968).
151. C.K. Jen, S.W. Foner, E.L. Cochran, and N.A. Bowers, Phys. Rev., 112, 1169 (1958).
152. B.H.J. Bielski and R.B. Timmons, J. Phys. Chem., 68, 347 (1964).
153. T.J. Schaafsma, G.A. van der Velde, and J. Kommandeur, Molecular Phys., 14, 501 (1968).
154. R.D. Iyengar and V.V. Subba Rao, J. Am. Chem. Soc., 90, 3267 (1968).
155. R.D. Iyengar, V.V. Subba Rao, and A.C. Zettlemoyer, Surface Science, 13, 251 (1969).

156. J.H. Lunsford, J. Colloid and Interface Science, 26, 355 (1968).
157. R.W. Schulz, Z. Physik, 109, 517 (1938).
158. C.T. Zahn, Phys. Rev., 34, 461 (1933).
159. C.B. Colburn, R. Ettinger, and F.A. Johnson, Inorganic Chemistry, 2, 1305 (1963).
160. D.W. Overall and D.H. Whiffen, Mol. Phys., 4, 135 (1961).
161. R. Beringer and J.G. Castle, Phys. Rev., 78, 581 (1950).
162. C.K. Jen, S.W. Foner, E.L. Cochran, and V.A. Bowers, Phys. Rev., 112, 1169 (1958).
163. A. Solbakkën and L.H. Reyerson, J. Phys. Chem., 63, 1622 (1959).
164. A. Solbakkën, Acta Chem. Scand., 21, 1123 (1967).
165. J.H. Lunsford, J. Chem. Phys., 46, 4347 (1967).
166. J.H. Lunsford, J. Phys. Chem., 72, 2141 (1968).
167. J.H. Lunsford, J. Phys. Chem., 72, 4163 (1968).
168. C.L. Gardner and M.A. Weinberger, Can. J. Chem., 48, 1317 (1970).
169. B.M. Hoffman and N.J. Nelson, J. Chem. Phys., 50, 2598 (1969).
170. W. Kanzig and M.H. Cohen, Phys. Rev. Letters, 3, 509 (1959).
171. D.E. Stogryn and A.P. Stogryn, Mol. Phys., 11, 371 (1966).
172. A.V. Alekseev, V.N. Filimonov, and A.N. Terenin, Dvkl. Akad. Nauk SSSR, 150, 584 (1963).
173. L.H. Piette, F.A. Johnson, K.A. Booman, and C.B. Colburn, J. Chem. Phys., 35, 1481 (1961).
174. H.E. Doorenbos and B.R. Loy, J. Chem. Phys., 39, 2393 (1963).
175. R. Ettinger and C.B. Colburn, Inorg. Chem., 2, 1311 (1963).
176. F.J. Adrian, E.L. Cochran, and V.A. Bowers, Advan. Chem., 32, 50 (1962).
177. J.B. Farmer, M.C.L. Gerry and C.A. McDowell, Mol. Phys., 8, 253 (1964).

178. P.H. Kasai and E.B. Whipple, Mol. Phys., 9, 497 (1965).
179. C.A. McDowell, H. Nakajima, and P. Raghunathan, Can. J. Chem., 48, 805 (1970).
180. C.B. Colburn, R. Ettinger, and F.A. Johnson, Inorg. Chem., 3, 455 (1964).
181. T.M. Pietrzak and D.E. Wood, J. Chem. Phys., 53, 2454 (1970).
182. P.W. Atkins and M.C.R. Symons, The Structure of Inorganic Radicals, Elsevier Publishing Co., London, 1967, p. 242.

APPENDIX

```

IMPLICIT REAL*8(A-H,O-Z)
DIMENSION H(91,91),TP(91,91),G(91,91),G2(91,91),A(91,91),
1AA2(91,91),AALPH2(91,91),C1(91,91),C2(91,91),C4(91,91),C5(91,91),
2C6(91,91),PHI(91),SP(91),CP(91),ST(91),CT(91),SP2(91),CP2(91),
3ST2(91),CT2(91),CSP2(91),GALPH2(91),PHID(91),TITLE(20)

```

C

```

READ(5,883)TITLE
READ(5,894) NTIMES,NTHETA,NPHI
KOUNT=0

```

4

```

READ(5,890) GX,GY,GZ,FREQ,SPIN
READ(5,891)AX,AY,AZ
WRITE(6,883)TITLE
WRITE(6,899)FREQ
WRITE(6,880)GX,GY,GZ
WRITE(6,898)AX,AY,AZ
WRITE(6,897)SPIN,NTHETA,NPHI

```

883

```

FORMAT(20A4)

```

890

```

FORMAT(5F10.5)

```

891

```

FORMAT(3F10.3)

```

894

```

FORMAT(3I3)

```

899

```

FORMAT(1X,'THE FREQUENCY IS',F10.5,' MHZ.')
```

880

```

FORMAT(1X,'GX= ',F10.5,' GY= ',F10.5,' GZ= ',F10.5)

```

898

```

FORMAT(1X,'AX= ',F10.3,' AY= ',F10.3,' AZ= ',F10.3,' IN GAUSS'

```

897

```

FORMAT(1X,'SPIN= ',F10.1,' NTHETA= ',I3,' NPHI= ',I3)

```

```

START=SCLOCK(0.0)

```

```

FREQ=FREQ*1.00+06

```

```

AX=AX*GX*1.39962640+06

```

```

AY=AY*GY*1.39962640+06

```

```

AZ=AZ*GZ*1.39962640+06

```

```

GX2=GX*GX

```

```

GY2=GY*GY

```

```

GZ2=GZ*GZ

```

```

AX2=AX*AX

```

```

AY2=AY*AY

```

```

AZ2=AZ*AZ

```

```

AXY2=AX2*AY2

```

```

GAX2=GX2*AX2

```

```

GAY2=GY2*AY2

```

```

GAZ2=GZ2*AZ2

```

C

```

BO=0.927320-20

```

```

HH=6.625170-27

```

```

RAD=1.74532925199430-02

```

C

```

DPHI=NPHI

```

```

IF(NPHI.GT.1)DPHI=90.00/FLOAT(NPHI-1)

```

C

```

A1=(AX2*AX2-2.00*AX2*AY2+AY2*AY2)*GX2*GY2

```

```

A2=A1*GAZ2

```

```

A5=HH/BO

```

```

A3=A5*A5

```

```

A4=SPIN*(SPIN+1.00)

```

```

11  A6=A5*FREQ
    SMI=SPIN
    B1=SMI*SMI
    B2=A3*B1/2.000
    B3=A3*(A4-B1)/4.000
    B4=A5*SMI
C   IF(SMI.LT.SPIN)GO TO 56

    PHI(1)=0.000
    PHID(1)=PHI(1)
    AAP=DPHI*RA0
    DIV=1.0/FLOAT(NTHETA-1)
    CT(1)=1.00
    CT2(1)=1.00
    ST(1)=0.00
    ST2(1)=0.00
    DO 17 I=2,NTHETA
    CT(I)=CT(I-1)-DIV
    CT2(I)=CT(I)*CT(I)
    ST(I)=DSQRT(1.00-CT2(I))
    ST2(I)=ST(I)*ST(I)
17  C
    IF(NPHI.LE.1)GO TO 60
    DO 98 I=2,NPHI
    PHI(I)=PHI(I-1)+AAP
    PHID(I)=PHID(I-1)+DPHI
98  60
    DO 89 NP=1,NPHI
    SP(NP)=DSIN(PHI(NP))
    CP(NP)=DCOS(PHI(NP))
    SP2(NP)=SP(NP)*SP(NP)
    CP2(NP)=CP(NP)*CP(NP)
    CSP2(NP)=CP2(NP)*SP2(NP)
    GALPH2(NP)=GX2*CP2(NP)+GY2*SP2(NP)
89  CONTINUE
    DO 48 NP=1,NPHI
    DO 43 NT=1,NTHETA
    G(NT,NP)=DSQRT(GALPH2(NP)*ST2(NT)+GZ2*CT2(NT))
    G2(NT,NP)=G(NT,NP)*G(NT,NP)
    AALPH2(NT,NP)=(GX2*CP2(NP)+GY2*SP2(NP))/G2(NT,NP)
    A(NT,NP)=DSQRT(G2(NT,NP)*AALPH2(NT,NP)*ST2(NT)+GAZ2*CT2(NT))/G(NT,
1NP)
    AA2(NT,NP)=A(NT,NP)*A(NT,NP)
    C1(NT,NP)=G2(NT,NP)*AALPH2(NT,NP)
    C2(NT,NP)=GALPH2(NP)*AA2(NT,NP)
    C4(NT,NP)=G2(NT,NP)*G2(NT,NP)*C2(NT,NP)
    C5(NT,NP)=C4(NT,NP)*AALPH2(NT,NP)
    C6(NT,NP)=G2(NT,NP)*C4(NT,NP)
    IP(NT,NP)=GZ2*GALPH2(NP)/G2(NT,NP)
48  C
56  DO 58 NP=1,NPHI
    DO 58 NT=1,NTHETA
1122 B9=(B4*A(NT,NP)-A6)/G(NT,NP)
    B82=B6*B9
    CC=B2*((GZ2*(C1(NT,NP)-GALPH2(NP)*AZ2)**2*ST2(NT)*CT2(NT))/C6(NT,
1P)+(A1*ST2(NT)*CSP2(NP))/C4(NT,NP)+(B3/G2(NT,NP))*((C1(NT,NP)*AZ2
2)/C2(NT,NP)+(GALPH2(NP)*AXY2)/C1(NT,NP)+(A2*CT2(NT)*CSP2(NP))/C5(
3T,NP))
    X=B82-CC*4.00

```

```

C      H(NT,NP)=(-BB+DSQRT(X))/2.D0
C
58     CONTINUE
C
      IF(SMI.LT.SPIN.OR.KOUNT.GT.0)GO TO 1111
      WRITE(1,603)(CT(I),I=1,NTHETA)
      WRITE(1,600)(PHID(I),I=1,NPHI)
1111   WRITE(6,1000)
      WRITE(6,1002)PHID(1)
      DO 70 NP=1,NPHI
      IF(NP.GT.1)WRITE(6,1003)PHID(NP)
      DO 80 NT=1,NTHETA,4
      K=NT+1
      L=NT+2
      M=NT+3
      WRITE(6,1001)H(NT,NP),TP(NT,NP),H(K,NP),TP(K,NP),H(L,NP),TP(L,NP)
      1H(M,NP),TP(M,NP)
80     CONTINUE
70     CONTINUE
1000   FORMAT(1H1,3(/),3X,4('FIELD(GAUSS)',3X,'INTENSITY',2X)/)
1001   FORMAT(5X,4(F3.2,5X,F3.5,5X))
1002   FORMAT('PHI=',F5.1,' DEGREES')
1003   FORMAT(3(/),'PHI=',F5.1/)
      DO 30 I=1,NPHI
30     WRITE(1,601)(H(J,I),J=1,NTHETA)
      DO 31 I=1,NPHI
31     WRITE(1,602)(TP(J,I),J=1,NTHETA)
600    FORMAT(13F6.2)
601    FORMAT(10F6.2)
602    FORMAT(10F3.5)
603    FORMAT(15F6.4)
C
      SMI=SMI-1.D0
      IF(SMI.LT.-SPIN)GO TO 5
      GO TO 11
5      TIME=SCLOCK(START)
      WRITE(6,850)TIME
      NTIMES=NTIMES-1
      KOUNT=KOUNT+1
      IF(NTIMES.GT.0) GO TO 4
850    FORMAT(1H0,'TIME REQUIRED',F3.3,' SECONDS'/)
      STOP
      END

```